



Tomas Kamencek, BSc BSc

Thermal transport and vibrational properties in metal-organic frameworks from first principle calculations

MASTER'S THESIS

to achieve the university degree of

Diplom-Ingenieur

Master's degree programme: Technical Physics

submitted to

Graz University of Technology

Supervisor

Ao.Univ.-Prof. Dipl.-Ing. Dr.techn. Egbert Zojer

Co-Supervisor

Dr. Natalia Bedoya-Martínez

Institute of Solid State Physics

Graz, July 2018

AFFIDAVIT

I declare that I have authored this thesis independently, that I have not used other than the declared sources/resources, and that I have explicitly indicated all material which has been quoted either literally or by content from the sources used. The text document uploaded to TUGRAZonline is identical to the present master's thesis.

Date

Signature

Contents

1. Introduction	1
2. Metal-organic frameworks	5
3. Theory and computational methods	8
3.1. Derivation of the thermal conductivity tensor	8
3.2. Phonon calculations	12
3.2.1. Finite differences approach	14
3.2.2. Perturbative approach	15
3.3. Phonon lifetimes	15
3.3.1. Used model for phonon lifetimes	18
3.4. Computational methods	20
3.4.1. Density functional theory	20
3.4.2. Calculation of Raman spectra within DFT	21
3.4.3. Density functional tight binding	23
4. Computational details	27
4.1. VASP	28
4.2. DFTB+	30
4.3. Lattice parameter relaxations	31
4.4. Phonon calculations	32
4.5. Phonon lifetimes	34
5. Results and discussion	37
5.1. Raman spectra	38
5.2. Comparison of the phonons obtained with DFTB+ and VASP	47
5.3. Thermal conductivity	50
5.3.1. Brillouin zone sampling	51
5.3.2. Influence of the organic linkers	53
5.3.3. Influence of the metallic nodes	70
5.4. Concluding remarks	87
6. Summary	90
A. Appendices	105
A.1. Heat capacity for a system of harmonic oscillators	105
A.2. DFTB3	106
A.3. First Brillouin zone and high symmetry point of a fcc Bravais lattice	109
A.4. Linear linkers: IRMOF-130, IRMOF-131, and IRMOF-132	110

1. Introduction

Life and the universe itself are full of non-equilibrium processes. Wherever there is a transfer of energy between systems, the thermodynamically equilibrated states are disturbed. These perturbations might be of electromagnetic, chemical or thermal origin, for example. In physics, people began to describe these rather complex non-equilibrium problems with relatively simple laws and equations early. Relations like Ohm's law, the Seebeck effect, Fick's law, the Hall effect, Fourier's law and many others were based on empirical findings and initially lacked fundamental physical proofs. Due to the nature of these typically linear descriptions of difficult problems, there are certain limitations for all these laws. For electrical conductivity, for instance, Ohm's law is only valid for electric fields below a certain threshold. However, those simple descriptions of non-equilibrium problems are still forming the essential backbone of (classical) physics.

The non-equilibrium process that this thesis deals with is the exposure of the system to small¹ temperature gradients on a crystalline system. The phenomenological proportionality constant that relates the temperature gradient to the heat flux density is the thermal conductivity. In practice, this quantity is one of the most important properties of a solid because it determines, how fast heat is transferred through the system from the hot to the cold side. For most classes of materials the mechanisms of heat transport can be attributed to two basic energy carriers: electrons and phonons. Although there might be contributions from other interactions in the solid - quantised as quasiparticles like magnons, plasmons etc. - these two usually dominate the thermal conductivity.

There are numerous examples in nature and technology, where thermal transport properties are one of the main concerns. Consider a piece of electrically conducting material, for example. If an electrical current flows through the solid, heat will be generated (by means of Joule heating and additionally recombination heating in the case of semiconductors). This heat has to be dissipated at least with the same speed as new energy density is generated in order to prevent thermal runaway. In semiconductor physics a situation like this can be modelled in order to predict the thermodynamically stable situation if the temperature dependence of the charge carrier mobility as well as the thermal conductivity of the solid are known. However, this requires the determination of these quantities in a microscopic or even a quantum-mechanical picture. Subsequently, macroscopic simulations can be carried out with the parameters obtained. Modelling of materials properties is, therefore, the first step in multiscale simulations predicting the behaviour of real applications.

A further example, where the thermal transport properties are a main concern, are thermoelectric effects. Especially in systems like metals, where the electronic contributions overweigh the phononic ones, the movement of the electrons also results in an electric current density. This effect is known as thermoelectricity. Therefore, one can generate electric currents or voltages (depending on the boundary conditions) by applying a temperature gradient to solids with distinct thermoelectric properties.

Although there are many models of the thermal conductivity for certain inorganic sys-

¹So small that the resulting heat flux density can be described with Fourier's law (cf. eq. (3.8))

1. Introduction

tems available, e.g. for metals and semiconductors, the situation is much more complicated for organic or hybrid systems. For that reason, thermal transport is only poorly understood in these classes of materials, in spite of its importance already illustrated. With the increasing demand of organic LEDs (OLEDs), for example, it is important to understand and to be able to predict thermal transport in such materials too. However, in molecular crystals one has to deal with large, complex systems and additional interactions like dispersion forces that can be neglected for metals. Moreover, due to the rather bound electrons of organic crystals compared to metals, the phononic contributions for the thermal conductivity are very likely to dominate. For that reason, in the following the focus will be on the thermal transport properties arising from lattice vibrations. Let us consider a very simplistic model system, based on which some general tendencies can be illustrated. The periodic system consists of a one-dimensional chain of two atoms in the primitive unit cell connected with linear springs. Obviously the two atoms differ in their masses, otherwise the cell size could be reduced. By solving Newton's equation with a plane-wave ansatz one obtains the phonon band structure for this system. This can be seen in figure 1.1. For certain phase shifts between the movements of atoms in neighbouring unit cells - described with the reciprocal wavelength q - the eigenfrequencies ω can be calculated. If one replaces now the heavier one of the two atoms with another atom with even larger and larger mass, the band structure changes as it is seen in figure 1.1.

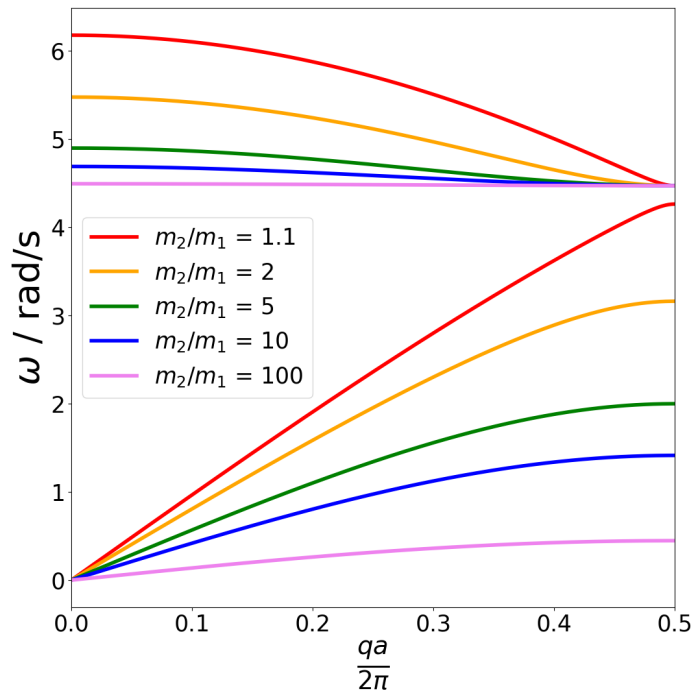


Fig. 1.1: Phonon band structure of a linear one-dimensional chain of two atoms with different masses m_1 and m_2 in a primitive unit cell of length a . The optical and acoustic bands are plotted for different mass ratios m_2/m_1 . $\omega \dots$ phonon frequency, $q \dots$ phonon wave vector.

As the ratio of the masses increases, some noticeable features can be observed. The bands tend to become flatter and to be restricted to lower frequencies. The real space analogue to flat bands is a localisation of modes at certain atoms. Localised vibrations are, of course, inhibitors of thermal transport, since phonon modes cannot efficiently transfer heat from one atom to its neighbour in this way. Although in most inorganic crystals there are not very large mass differences present, this is exactly the case for metal-organic hybrid structures like metal-organic frameworks (MOFs). Due to the large amount of atoms in their unit cells, MOFs have many optical phonons, with some of them possibly reaching lower frequencies, which are typically found to be more important for the thermal conductivity than higher frequency phonons. Therefore, MOFs have the potential to show interesting thermal transport properties.

MOFs are materials which have recently gained a lot of scientific interest as can be seen in figure 1.2. In that plot the number of publications on *Web of Science* having "MOF" or "metal-organic framework" as their topic is displayed from 1994 to July 2018. Note that the last bar is smaller because it accounts only for the first half of the year 2018.

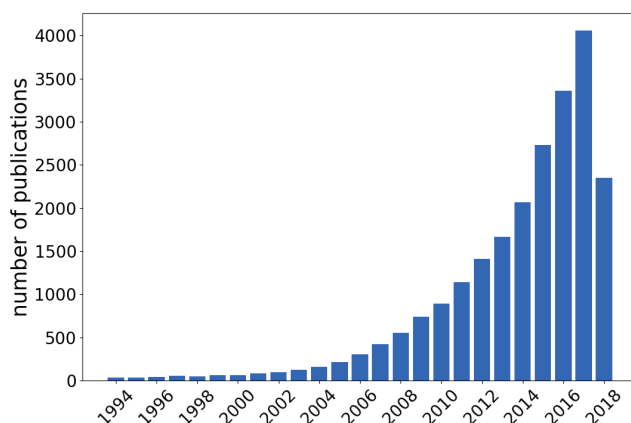


Fig. 1.2: Number of publications listed by Web of Science that have "MOF" or "metal-organic framework" as their topic. Evaluated at 2 July 2018, 7 pm.

The general structure of MOFs contains two main constituents: metallic clusters (nodes) connected with organic molecules (linkers). Depending on the length of the linkers, the structures are relatively open and usually show cavities or channels, with both resulting in a large amount of internal surface area. For this reason, the main applications of MOFs are uses, where one exploits this large surface areas like catalysis and gas storage. In all those applications temperature gradients are generated. This raises the question, whether their thermal transport properties are suitable to dissipate the heat fast enough for preventing the material from destruction. If MOFs are to be used efficiently in future applications, the knowledge of their thermal transport behaviour is absolutely essential, but hardly investigated yet. This can be seen as the motivation for this thesis. However, as there are numerous possibilities to vary the constituents in order to derive structure-to-property relationships, a systematic approach and accurate

1. Introduction

computational simulation methods have to be chosen. As a consequence, first-principle calculations are employed within a quasi-harmonic lattice dynamics approach to study the influences the different constituents of a MOF have on the vibrational properties and the thermal conductivity.

Therefore, in section 2 some important applications and structural considerations of MOFs are summarised in order to better understand these materials. Once this is accomplished, the next step is to briefly condense the theoretical approaches, approximations and methodologies that one can use in order to obtain the desired materials properties. This is the topic of section 3. Here, one has to consider the necessary calculations to compute the thermal conductivity. The quantities of interest can be divided into harmonic and anharmonic ingredients as will be shown. The following part mainly deals with some computational details. In section 4, the used programmes as well as the most important input parameters are introduced and discussed in order to allow to reproduce the obtained results. These are presented and discussed in section 5, before the most important findings are condensed in the summary in section 6.

2. Metal-organic frameworks

transition dependent on the ambient temperature and pressure [1]. The phase shown in figure 2.2(a) is the high temperature phase (ht) that is observed experimentally. By varying the environmental conditions one can, therefore, influence the structure of certain systems. Considerations of that kind complicate the usage of MOFs since phase transitions might limit the operating range in real applications.

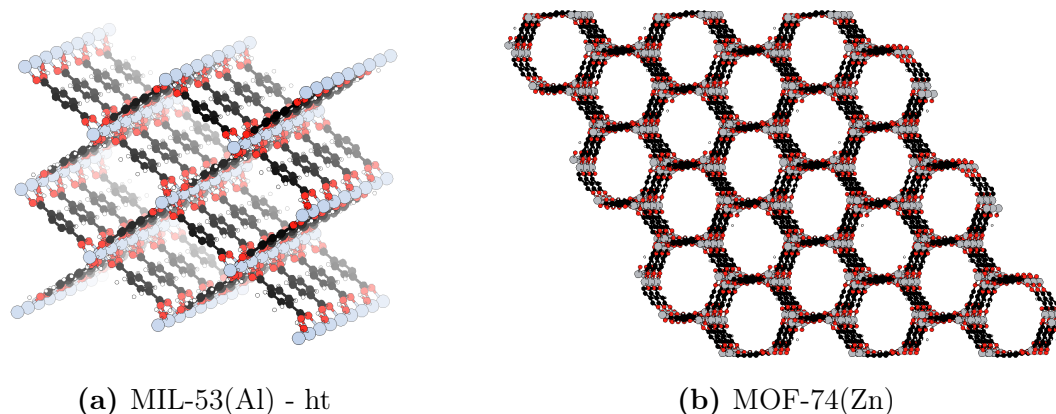


Fig. 2.2: Some exemplaric MOF structures forming channels through the crystal.

Most applications of MOFs exploit the enormous internal surface areas of MOFs. One of the first typical application people have been using MOFs for is gas absorption [2, 3, 4]. Especially for systems that have three-dimensionally confined cavities in their structure one can entrap gases inside the porous frameworks. This has been excessively studied in particular for carbon dioxide [3], hydrogen [5], water [6] and methane [7]. Furthermore, MOFs were used as adsorption coolers [8, 9, 10] or in adsorption vacuum pumps instead of the much heavier zeolithes, or as components of thermal batteries [11] storing heat by means of adsorption. If the organic linkers are functionalised with certain chemical groups, they also can be used for catalysis [12] where certain molecules preferentially react with each other at the extended surfaces inside a MOF. If one allows reactions to change the linker, for example, by substitution of functional groups, or if one modifies the oxidation numbers of the metals in the nodes, this very likely results in a change in physical properties (colour, electrical resistivity, crystal structure etc.). If these variations of properties can be measured, sensing is another typical application a MOF is suitable for [13].

However, in all the aforementioned potential applications, non-equilibrium processes involving temperature gradients happen. This could either be the case when chemical reactions are of exothermal or endothermal nature, if MOFs are used for cooling or heating purposes, and basically for every type of process where molecules are adsorbed on the internal surfaces of the framework. In spite of its importance for all the typical applications of MOFs, the thermal transport properties have been hardly investigated yet, leaving academic and commercial users in the dark about what influences temperature gradients will have on the system. Will the generated heat be dissipated fast enough? Will the material suffer from thermal degradation? Will thermoelectricity be observed?

Can the input of thermal energy reach the central part of the MOF crystal in finite time? These and similar questions arise in connection with non-equilibrium situations during applications and can only be answered if one has a fundamental understanding of the main influences governing thermal conductivity in MOFs. Once it is figured out, how the different constituents of the crystals influence the thermal conductivity, one can, as a next step, use this knowledge and choose linkers or nodes in a way that desired thermal transport properties can be observed. By replacing constituents of the crystals only in one direction, one can also obtain anisotropy in thermal conductivity so that preferred pathways for thermal transfer can be realised, while other directions are blocked, in order to save adjacent sensitive components, for example. A very useful aspect of MOFs is their quasi-infinite number of possible linker molecules from organic chemistry to choose from combined with more or less bulky nodes. Future steps would be to study the influence of different adsorbates or species caught in the cavities on the thermal conductivity. The more open and porous MOFs become, the more likely they are to form interpenetrated structures what will reduce the cavity sizes, but definitely increases thermal transport due to the much denser structures. One of the most difficult considerations will be the description of thermal transport across boundaries of different MOFs or different grains of an imperfect solid. This requires the correct understanding of the single-crystalline systems before. Without doubt, MOFs are a very interesting class of materials having high potential for industrial applications as well as fundamental research. The investigation of thermal transport properties is right in the beginning and will take ages until it will have been described in a proper, quantitative manner. However, until a general understanding of the thermal transport behaviour in MOFs is obtained, many studies will have to be conducted. One has to start with simpler systems and systematically vary small parts of the geometry, unless one wants to get lost in the huge variety of different constituents. In order to take the first step in the attempt to deduce structure-to-property relationships for MOFs, the following approach was chosen: to analyse the effects of different components on the thermal conductivity it is useful to start by first looking at the lattice vibrations and the respective phonon band structures, since these quantities are supposed to be the ones determining the thermal transport properties. The bigger challenge, however, is to anharmonic effects take into account. Starting from the relatively well-known MOF-5 (cf. fig. 2.1(a)) the two main parts of a MOF - the linkers and the nodes - are systematically varied to study the changes of vibrational properties and thermal transport. The thermal conductivity is studied for the simpler case of IRMOFs, which have the convenient attribute that they have only one kind of linker in all three directions arranged in a cubic crystal system. The linkers are substituted by different aromatic or alkyne molecules to understand their influence. Also the impact of the metals in the nodes is investigated by considering three different species (Zn, Mg, Ca), with the principal node geometry being fixed. In order to understand, which physical ingredients are worthwhile looking at, and which quantities are needed to calculate the thermal conductivity, the theoretical background has to be dealt with. Therefore, the relevant equations as well as their derivations are introduced in the next section.

3. Theory and computational methods

In this section the expression for the thermal conductivity tensor within the lattice dynamics approach will be derived. Based on that equation, each contribution will then be dealt with in more detail. When it has become clear what needs to be calculated, some methods will be discussed, which can be used to obtain these quantities in practice using well-established procedures.

3.1. Derivation of the thermal conductivity tensor

The derivation of the thermal conductivity tensor will be done in detail to be able to understand all the approximations and assumptions that are made. This is essential for understanding the limitations and deficiencies of the used approach. The derivation up to equation (3.3) is adopted from Ibach and Lüth [14, p. 245ff], whereas the problem-specific expressions were individually derived and compared to the final equations from literature (e.g. [15, 16]).

In order to describe (quantum-mechanical) systems it is often useful to introduce a distribution function $f(\mathbf{r}, \mathbf{k}, t)$ that describes the probability to find the system at a given time t at a specific point² in phase space - i.e. a multidimensional space represented by the momenta $\hbar\mathbf{k}$ and positions \mathbf{r} of all particles involved. Liouville's equation follows as a direct consequence of continuity considerations.

$$\frac{df}{dt} = \frac{\partial f}{\partial t} + \nabla_{\mathbf{k}} f \cdot \frac{\partial \mathbf{k}}{\partial t} + \nabla_{\mathbf{r}} f \cdot \frac{\partial \mathbf{r}}{\partial t} = 0 \quad (3.1)$$

The first partial derivative in equation (3.1) accounts for explicit temporal changes in the distribution function, whereas the second accounts for external forces³ and the last one for spatial changes. Throughout this derivation, we will neglect external forces - i.e. the second term - completely. If we rearrange equation (3.1) and interpret the time derivative of the position \mathbf{r} as the group velocities, we end up with the Boltzmann transport equation (BTE) in the special case of no external forces.

$$\frac{\partial f}{\partial t} = -\nabla_{\mathbf{r}} f \cdot \mathbf{v}_{\mathbf{g}} + \left. \frac{\partial f}{\partial t} \right|_{coll} \quad (3.2)$$

The so-called collision term - i.e. the last term on the right side of the BTE - accounts for temporal changes in the distribution function due to collisions with other particles in the system and is usually the biggest challenge when it comes to solving the equation. One convenient way to (seemingly) circumvent the insufficient knowledge about the collision term is to make use of the relaxation time approximation (RTA) employing the following ansatz for the collision term:

²To be exact $f(\mathbf{r}, \mathbf{k}, t)$ is the probability to find the system at time t in the phase space volume $[\mathbf{r}, \mathbf{r} + d\mathbf{r}]$, $[\mathbf{k}, \mathbf{k} + d\mathbf{k}]$.

³The time derivative of the momentum corresponds to external forces.

3.1. Derivation of the thermal conductivity tensor

$$\left. \frac{\partial f}{\partial t} \right|_{coll} = \frac{f_0 - f}{\tau} \quad (3.3)$$

This approximation implies that the system returns to approximately 63 % of its equilibrium distribution f_0 after one relaxation time τ has passed in absence of any external forces and spatial variations in the distribution. In order to analyse the BTE (eq. 3.2) further one has to think about possible contributions to the spatial gradient of f . The distribution function f is usually only indirectly dependent on the spatial coordinates via quantities like the chemical potential μ or the temperature T . For phonons, where the particle number is a non-conserved quantity, the chemical potential must vanish. So does its derivative. In cases, where thermal transport is important, a temperature gradient will however be present. This consideration and the RTA (eq. (3.3)) lead to the following equation in the stationary case.

$$f = f_0 - \tau \nabla T \cdot \mathbf{v}_g \frac{\partial f}{\partial T} \approx f_0 - \tau \nabla T \cdot \mathbf{v}_g \frac{\partial f_0}{\partial T} \quad (3.4)$$

The last approximate equality in equation (3.4) differs from the exact solution by the fact that not the temperature derivative of the actual distribution function, but that of the equilibrium one is considered. Therefore, one assumes that there is not a big change regarding the temperature dependence between f and f_0 . For phonons, the Bose-Einstein distribution is chosen as the equilibrium distribution function.

$$f_0 = f_{BE} = \frac{1}{\exp\{\beta \hbar \omega_n(\mathbf{q})\} - 1} \quad (3.5)$$

In this equation, β is the inverse temperature $\frac{1}{k_B T}$ scaled with the Boltzmann constant k_B , and $\omega_n(\mathbf{q})$ is the phonon frequency of band n at the wave vector \mathbf{q} . The distribution function according to equation (3.4) can be used to calculate a number of flux densities (energy, heat, particles). The way, in which f is used, depends on the properties one wants to study. If the distribution function according to equation (3.4) is inserted in the general expression for the i^{th} component of the heat flux density (cf. eq. (3.6)) $j_{Q,i}$ for phonons, one obtains the result according to equation (3.7). Note that the shorthand notation $\partial_i := \frac{\partial}{\partial x_i}$ is used in the following equations.

$$j_{Q,i} = \frac{1}{8\pi^3} \sum_n \int d^3q v_{g,i}(\mathbf{q}) \hbar \omega_n(\mathbf{q}) f \quad (3.6)$$

$$j_{Q,i} = \frac{1}{8\pi^3} \sum_n \int d^3q \tau_n(\mathbf{q}) k_B \frac{(\beta \hbar \omega_n(\mathbf{q}))^2 \exp\{\beta \hbar \omega_n(\mathbf{q})\}}{[\exp\{\beta \hbar \omega_n(\mathbf{q})\} - 1]^2} v_{g,n,i}(\mathbf{q}) v_{g,n,j}(\mathbf{q}) \partial_j T \quad (3.7)$$

It shall be emphasised that the term f_0 in the expression of the distribution function f vanishes during the integration. If the heat flux density of equation (3.7) is compared to Fourier's law (cf. eq. (3.8)) the thermal conductivity can be identified as the tensor quantity shown in equation (3.9).

3. Theory and computational methods

$$j_{Q,i} = \kappa_{ij} \partial_j T \quad (3.8)$$

In the linear tensorial expression of equation (3.8) the thermal conductivity tensor κ_{ij} is introduced as the proportionality constant between the heat flux density in direction i and a temperature gradient in direction j .

$$\kappa_{ij} = \frac{1}{8\pi^3} \sum_n \int d^3q \tau_n(\mathbf{q}) k_B \frac{(\beta \hbar \omega_n(\mathbf{q}))^2 \exp\{\beta \hbar \omega_n(\mathbf{q})\}}{[\exp\{\beta \hbar \omega_n(\mathbf{q})\} - 1]^2} v_{g,n,i}(\mathbf{q}) v_{g,n,j}(\mathbf{q}) \quad (3.9)$$

Still the sum over the indices n sums over contribution of all the $3N$ phonon bands where N is the number of atoms in the primitive unit cell. The integral accounts for all contributions at wave vectors \mathbf{q} inside the first Brillouin zone. From statistical physics one can derive an expression for the specific heat capacity of a system of independent harmonic oscillators according to the following equation. The derivation can be found in the appendix A.1.

$$c_V(T) = \frac{1}{8\pi^3} \sum_n \int d^3q k_B \frac{(\beta \hbar \omega_n(\mathbf{q}))^2 \exp\{\beta \hbar \omega_n(\mathbf{q})\}}{[\exp\{\beta \hbar \omega_n(\mathbf{q})\} - 1]^2} = \frac{1}{8\pi^3} \sum_n \int d^3q C(\omega_n(\mathbf{q})) \quad (3.10)$$

The integrand of the equation above is exactly the central part of the integrand in equation (3.9). For that reason, the expression for the thermal conductivity tensor can often be found in the following form:

$$\kappa_{ij} = \frac{1}{8\pi^3} \sum_n \int d^3q \tau_n(\mathbf{q}) C(\omega_n(\mathbf{q})) v_{g,n,i}(\mathbf{q}) v_{g,n,j}(\mathbf{q}) \quad (3.11)$$

It has to be emphasised that $C(\omega_n(\mathbf{q}))$ is not the heat capacity of a material that can, e.g., be determined from experiments. $C(\omega_n(\mathbf{q}))$ is only the contribution of one single phonon mode, which one would have to integrate over all frequencies in order to obtain the phononic contribution to the material's specific heat capacity labelled as $c_V(T)$. Actually it is only a shorthand notation, which contains the temperature derivative of the Bose-Einstein distribution function and, therefore, accounts for occupation of phonon modes participating in thermal transport. The heat capacity function can be seen in figure 3.1. In figure 3.1(a) also the Bose-Einstein distribution (cf. eq. (3.5)) is plotted, showing that the heat capacity function is much broader.

By using equation (3.9) or (3.11), one can immediately calculate the (phononic) thermal conductivity by only knowing the phonon density of states (phDOS) respectively the band structure and the relaxation times. The phonon bands then allow the computation of the "heat capacities" and the group velocities which are defined as the derivatives of the bands with respect to the wave vector.

3.1. Derivation of the thermal conductivity tensor

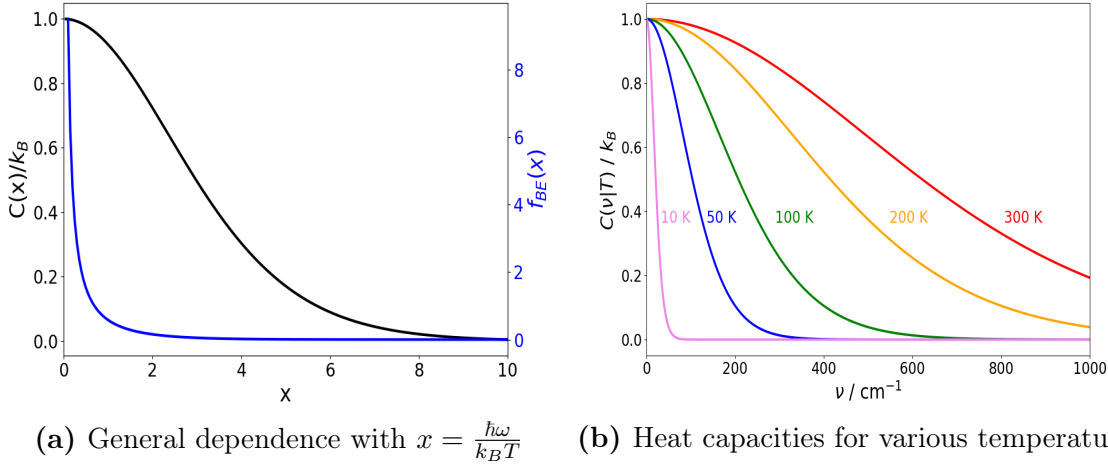


Fig. 3.1: Heat capacities according to eq. (3.10) for (a) the general univariate function compared to the Bose-Einstein distribution f_{BE} and (b) for different temperatures T as parameter over a frequency range ν . Mind that the curves for different temperatures correspond to a rescaling of the abscissa in (a).

The i^{th} component of the group velocity $v_{g,n,i}$ is defined as the derivative of the frequency of band n with respect to the i^{th} component of the wave vector q_i according to equation (3.12).

$$v_{g,n,i}(\mathbf{q}) = \frac{\partial \omega_n(\mathbf{q})}{\partial q_i} \quad (3.12)$$

The methods of how these quantities are obtained in practice will be the topic of the next subsections. There, we first focus on all the harmonic ingredients - i.e. the phonon band structure from which the group velocities and the heat capacities can be calculated (cf. sec. 3.2). In the next step, methods that are used to obtain the phonon lifetimes from the anharmonicities will be discussed (cf. sec. 3.3).

In principle, one can find a very similar expression for the electronic contribution to heat transport. The only differences are that one uses the Fermi-Dirac distribution as the equilibrium distribution function f_0 and that the chemical potential μ is not zero.

$$f_0 = f_{FD} = \frac{1}{\exp\{\beta(E_n(\mathbf{k}) - \mu)\} + 1} \quad (3.13)$$

In this equation $E_n(\mathbf{k})$ is the energy of the n^{th} band at the (electronic) wave vector \mathbf{k} . With non-vanishing chemical potential and a spin multiplicity of 2 the heat flux density changes slightly.

$$j_{Q,i} = \frac{1}{4\hbar\pi^3} \sum_n \int d^3q (E_n(\mathbf{k}) - \mu) \frac{\partial E_n(\mathbf{k})}{\partial k_i} f \quad (3.14)$$

For the distribution function f equation (3.4) can be applied again, if the chemical potential of the electronic system does not change as a function of the location. A

3. Theory and computational methods

comparison with Fourier's law (cf. eq. (3.8)) yields the electronic contribution to the thermal conductivity κ_{ij}^{elec} .

$$\kappa_{ij}^{elec} = \frac{1}{4\pi^3\hbar^2} \sum_n \int d^3k \tau_n^{elec}(\mathbf{k}) k_B \frac{(\beta(E_n(\mathbf{k}) - \mu))^2 \exp\{\beta(E_n(\mathbf{k}) - \mu)\}}{[\exp\{\beta(E_n(\mathbf{k}) - \mu)\} + 1]^2} \frac{\partial E_n(\mathbf{k})}{\partial k_i} \frac{\partial E_n(\mathbf{k})}{\partial k_j} \quad (3.15)$$

The ingredients to compute the electronic contributions are similar to those for phonons: the band structure respectively the DOS, and the electronic relaxation times. Even the chemical potential can be calculated from the DOS. However, the mobility of the charge carriers in organic crystals is dramatically reduced compared to metals and the bands are nearly fully occupied. Furthermore, the derivatives of the band energies with respect to the wave vector are typically very small for organic crystals. Therefore, this contribution will be neglected compared to the phononic part of equation (3.9).

3.2. Phonon calculations

As can be seen in the equation for the thermal conductivity (eq. (3.9)) for most of the integrand only the phonon frequencies - i.e. the band structure resp. the density of states - are needed. In order to obtain those, one has to solve Newton's equation of motion for all the atoms in the crystal. The derivation of the phonon frequencies is adapted from [17, p. 176f]. The interaction between the respective atoms is usually considered as being a linear function of the displacement from the equilibrium position. This is equal to the picture of the atoms being pairwise interconnected by stronger or weaker linear springs. The strength of these springs is determined by the energy landscape as a function of the atomic coordinates. This already implies that the resulting phonon normal modes are only valid within the harmonic approximation. This means that in this step one assumes the potential energy surface (PES) to have constant second derivatives⁴, or in other words, that the PES can be represented by a high-dimensional parabola. This assumption is only true, of course, if one does not move too far away from the minimum of the PES. Directly at the minimum, the PES (labelled with E) can be Taylor expanded with respect to the displacement $u_i^a(A)$ of each atom a in unit cell A in direction i . In this equation the indices i and j run over the cartesian directions x, y, z , and a and b over the atoms in the unit cells A and B .

$$E(\mathbf{r} + \mathbf{u}) = E(\mathbf{r}) + \frac{1}{2} \sum_{a,b} \sum_{i,j} \sum_{A,B} \frac{\partial^2 E}{\partial u_i^a(A) \partial u_j^b(B)} \Bigg|_{\mathbf{r}} u_i^a(A) u_j^b(B) + \dots \quad (3.16)$$

The first derivatives vanish at the minimum of the PES. The second derivatives are often referred to as either the force constant matrix or the Hessian matrix. In the harmonic approximation, where the usual concept of phonons is applicable, one truncates the expansion of equation (3.16) after the second order terms and uses the force constants

⁴The potential of a linear spring with a fixed spring constant C is a quadratic function of the displacement.

to describe the interactions between the atoms when solving the equations of motions. When it comes to that step, one however has to make sure that also possible interactions to adjacent unit cells are taken care of. Therefore, in general one has to define the force constants as quantities also dependent on the unit cell index (described with capital letters).

$$C_{ij}^{ab}(A, B) = \frac{\partial^2 E}{\partial u_i^a(A) \partial u_j^b(B)} = -\frac{\partial F_j^b(B)}{\partial u_i^a(A)} \quad (3.17)$$

That means that if one atom a in unit cell A is displaced in i direction, another atom b in unit cell B will *feel* a force that is linearly dependent on the force constant $C_{ij}^{ab}(A, B)$. The last equality in equation (3.17) uses the fact that one of the derivatives can be interpreted as the force on that respective atom. This equation is an important relation that can be exploited to obtain the force constants numerically, as will be discussed later.

When solving Newton's equations of motion for all the atoms in the unit cell, one can make use of the periodicity of the system and employ Bloch's theorem. Therefore, one can make the ansatz that a displacements $u_i^a(A)$ of atom a in unit cell A in i direction can be described by a plane wave:

$$u_i^a(A) = \frac{1}{\sqrt{m_a}} \xi_i^a \cdot \exp \{i(\mathbf{q} \cdot \mathbf{R}_A - \omega t)\} \quad (3.18)$$

In equation (3.18) m_a is the mass of atom a , ξ_i^a is the amplitude of the plane wave and \mathbf{R}_A is the lattice vector that defines the location of the unit cell A . After inserting the ansatz (eq. (3.18)) in the equations of motion, one ends up with a single matrix to diagonalise. This matrix $D_{ij}^{ab}(\mathbf{q})$ is called the dynamical matrix and is shown in equation (3.19).

$$D_{ij}^{ab}(\mathbf{q}) = \frac{1}{\sqrt{m_a m_b}} \sum_{\text{cells}:A,B} C_{ij}^{ab}(A, B) \exp \{i\mathbf{q} \cdot (\mathbf{R}_A - \mathbf{R}_B)\} \quad (3.19)$$

In essence, every element of this matrix is the Fourier transform of all the force constants between two atoms scaled with a factor containing their masses. Since both unit cell indices A and B run over all possible unit cells in the whole crystal, equation (3.19) can be written equally as:

$$D_{ij}^{ab}(\mathbf{q}) = \frac{1}{\sqrt{m_a m_b}} \sum_{\text{cells}:B} C_{ij}^{ab}(0, B) \exp \{-i\mathbf{q} \cdot \mathbf{R}_B\} \quad (3.20)$$

The difference of that equation is that the sum only accounts for all force constants between one atom a that is located in the *central* unit cell labelled as 0 and another atom b that is located in all the periodic images of the unit cell labelled with the index B . The advantage of using the form of equation (3.20) for the calculation of the dynamical matrix is a huge reduction of computational effort. In order to determine the force constants $C_{ij}^{ab}(0, B)$ one only has to displace the atoms in the *central* unit cell (0) and calculate the forces on the atoms in all the other unit cells (B) of the crystal.

3. Theory and computational methods

Once the dynamical matrix for a system is known, one can diagonalise it and directly obtain the (squared) phonon frequencies $\omega_n(\mathbf{q})$ and the eigenvectors $\mathbf{e}_n(\mathbf{q})$ for every desired wave vector \mathbf{q} (cf. eq. (3.21)).

$$\omega_n^2(\mathbf{q}) = \langle \mathbf{e}_n(\mathbf{q}) | D(\mathbf{q}) | \mathbf{e}_n(\mathbf{q}) \rangle \quad (3.21)$$

The eigenvectors contain all the amplitudes of the plane wave ansatz (cf. eq. (3.18)) that can be converted to real space displacements by a rescaling with the square roots of the respective masses.

This is one of the biggest differences to electronic band structure calculations. In that case one usually has to re-calculate the energies for every (electronic) wave vector \mathbf{k} . In the case of phonons, one only has to make sure that the series in equation (3.20) converges by taking enough force constants into consideration. In order to achieve this, one must usually increase the system size to large supercells to obtain a sufficient amount of terms in the series so that the force constants are small enough for the series to be converged.

3.2.1. Finite differences approach

The finite differences approach makes use of equation (3.17) to calculate the harmonic force constants of the system. Instead of really calculating the derivative, it is approximated with a central difference quotient. That means, that one has to displace every atom in the unit cell in each direction twice ($+i$ and $-i$ direction with $i = x, y, z$). In this way, one has to carry out $6N$ single point calculations where N is the number of atoms in the unit cell in order to obtain all the force constants. Luckily, one can reduce the number of necessary displacements by using the symmetries of the system. In the case of MOF-5 this reduces the effort from 636 displacements to only 19 due to the high (cubic) symmetry.

However, the approximation of a derivative by a difference quotient always imposes an error on the calculation. By choosing the central difference quotient one can at least decrease the error from $\mathcal{O}((\Delta r)^2)$ to $\mathcal{O}((\Delta r)^3)$. Another reason to keep the displacement very small besides numerical accuracy is that one should guarantee that the displacement is small enough to stay within the harmonic approximation of the PES. However, one must not choose the displacement too small because otherwise the effect will be suppressed by inevitable numerical noise. An example of how the harmonic approximation of an anharmonic potential could look like is displayed in figure 3.2 in section 3.3. Typical values that are used for such atomic displacements are approximately 0.01 Å. Comparing this with a typical bond distance being in the range of 1 Å this is indeed rather small and will in most cases fulfil both requirements: acceptable numerical accuracy and the validity of the harmonic approximation. From the atomic displacements, the change of the forces is determined and regarded as an approximation for the desired derivatives. From that, the dynamical matrix is constructed via a Fourier transform from which phonon frequencies can be calculated for any desired wave vector \mathbf{q} .

3.2.2. Perturbative approach

A somewhat different approach is density functional perturbation theory (DFPT). Like in ordinary perturbation theory, with DFPT one solves the quantum-mechanical problem of a system that is slightly perturbed from a reference state that is already solved. This perturbation can, for instance, be a superimposed electric field, an additional potential term etc. In the case of phonon calculations, the perturbation corresponds to an elastic term that originates from the displacement of one atom. Within the framework of DFPT there are analytical expressions to obtain the correction (usually up to second order) to the energy, the charge density, and the KS wave functions.

The way in which DFPT is used to calculate the phonons, however, changes between the available simulation packages. For example, the Vienna Ab-Initio Simulation Package (VASP) [18, 19, 20] performs DFPT calculations only at the Brillouin zone centre Γ . That infers that in order to obtain the complete phonon band structure, one has to increase the system to larger supercells and unfold the results afterwards. So in this approach, there is essentially no difference in the phonon calculation, only in the way how the interatomic force constants are calculated. There is even a drawback of this approach: with the finite differences method one can in principle run all the rather cheap single point calculations at once, whereas within DFPT one usually is forced to calculate the perturbative corrections of all the displacements sequentially. Furthermore, single point calculations are much cheaper with respect to computational time than a full DFPT calculation, where both types of calculations have to be carried out for the same super cell to obtain the same amount of information.

In contrast, there is an alternative way of making use of DFPT. The Quantum Espresso package [21, 22] considers a perturbation in reciprocal space: instead of an atomic displacement as perturbation, there a change of the PES due to a plane wave with wave vector \mathbf{q} is used. In that way, one can directly calculate the phononic vibrations for a specific \mathbf{q} point in the first Brillouin zone. In order to obtain the complete phonon band structure, one has to repeat the quite expensive DFPT calculation for a mesh of wave vectors. But still, one cannot calculate the phonons for any desired \mathbf{q} point from that. The approach to solve this problem is the following. The reciprocal force constants have to be calculated for a \mathbf{q} mesh that is fine enough to allow an accurate inverse Fourier transformation from those reciprocal to the real space force constants. The latter are the quantities that are calculated directly in the finite differences approach. Once you know the real space force constants, the dynamical matrix is constructible and from that quantity the phonons for any desired \mathbf{q} can be computed.

3.3. Phonon lifetimes

So far all considerations were focused on how one can obtain the phonon band structure, the knowledge of which is essential for calculating the heat capacities and group velocities for the thermal conductivity (cf. eq. 3.9). Still the problem remains, how one can obtain expressions for the phonon lifetime $\tau_n(\mathbf{q})$. First of all, it has to be stressed that in the usual concept of phonons, which are essentially obtained by solving the classical

3. Theory and computational methods

equations of motion within the harmonic approximation, every phonon "lives" forever - i.e. there is no finite relaxation time. This quantity only comes into play if one considers the anharmonic contribution of the PES. The Lennard-Jones potential being a typical anharmonic potential as well as its harmonic approximation can be seen in figure 3.2.

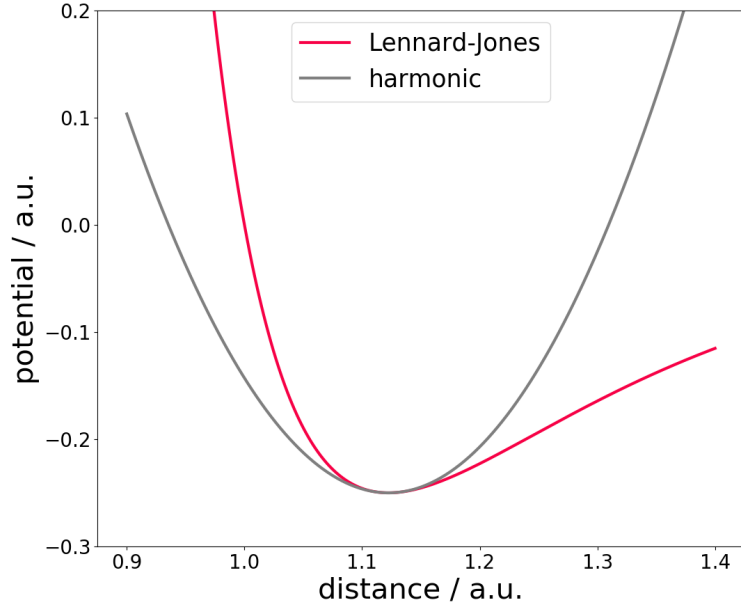


Fig. 3.2: Lennard-Jones potential plotted as a function of the distance in comparison with its harmonic approximation around the minimum.

One way to calculate the phonon lifetimes is Molecular Dynamics (MD). With this approach one can simulate large supercells and calculate the time dependent normal mode-coordinates (cf. eq. (3.35)) [23]. From this information one can then calculate how the harmonic energy (determined by the normal-coordinates) evolves in time. If finally the autocorrelation function of this energy is calculated, one can find the lifetime of that mode as a measure for how fast the autocorrelation decays.

The approach within lattice dynamics is rather different. Since the harmonic approximation corresponds to a truncation of the Taylor expansion of the PES after the second order term, the logical conclusion is to consider also higher order terms that then contain the anharmonicities of the system. With Fermi's golden rule one can derive an expression for the phonon lifetimes considering the third derivatives of the PES. The following considerations are based on [23, 24, 25]. The third derivative of the PES with respect to three displacements of atoms a, b, c being in the unit cells labelled with A, B, C in i, j, k direction is given by equation (3.22).

$$\Phi_{i,j,k}^{a,b,c}(A, B, C) = \frac{\partial^3 E}{\partial u_i^a(A) \partial u_j^b(B) \partial u_k^c(C)} = -\frac{\partial^2 F_k^c(C)}{\partial u_i^a(A) \partial u_j^b(B)} \quad (3.22)$$

The analytical expression considers both the conservation of energy (with the delta distributions in equation (3.23)) and the conservation of momentum (with the Kronecker delta in eq. (3.24)) of the interactions between three phonons with wave vector \mathbf{q} , \mathbf{q}' and \mathbf{q}'' . Furthermore, the occupation factors f (Bose-Einstein distribution) of all the phonons participating in possible scatter events are taken into account.

$$\begin{aligned} \tau_n^{-1}(\mathbf{q}) = & \frac{\hbar\pi}{8Z} \sum_{\mathbf{q}',n'}^{Z,3N} \sum_{\mathbf{q}'',n''}^{Z,3N} \left| \widetilde{\Phi}_{n,n',n''}(\mathbf{q}, \mathbf{q}', \mathbf{q}'') \right|^2 \cdot \{ [f(\omega_{n'}(\mathbf{q}')) + f(\omega_{n''}(\mathbf{q}'')) + 1] \cdot \\ & \cdot \delta(\omega_n(\mathbf{q}) - \omega_{n'}(\mathbf{q}') - \omega_{n''}(\mathbf{q}'')) + [f(\omega_{n'}(\mathbf{q}')) - f(\omega_{n''}(\mathbf{q}''))] \cdot \\ & [\delta(\omega_n(\mathbf{q}) + \omega_{n'}(\mathbf{q}') - \omega_{n''}(\mathbf{q}'')) - \delta(\omega_n(\mathbf{q}) - \omega_{n'}(\mathbf{q}') + \omega_{n''}(\mathbf{q}''))] \} \end{aligned} \quad (3.23)$$

The *interaction strength* $\widetilde{\Phi}_{n,n',n''}(\mathbf{q}, \mathbf{q}', \mathbf{q}'')$ of the three-phonon-process is essentially given by a multi-dimensional Fourier transform of the third-order force constants $\Phi_{i,j,k}^{a,b,c}$ scaled with the respective atomic masses m_a and the eigenvector overlap between the parts of the phononic eigenvectors $\mathbf{e}_{n,i}^a(\mathbf{q})$ that belong to a certain atom a and a wave vector \mathbf{q} . The position vectors in the exponent of the Fourier transform of equation (3.24) are labelled as \mathbf{r}_b for the coordinates of atom b in the "central" unit cell (0), whereas \mathbf{R}_B stands for the lattice vector of cell B relative to cell 0.

$$\begin{aligned} \widetilde{\Phi}_{n,n',n''}(\mathbf{q}, \mathbf{q}', \mathbf{q}'') = & \sum_{i,a}^{3,N} \sum_{j,b,B}^{3,N,Z} \sum_{k,c,C}^{3,N,Z} \frac{\delta_{\mathbf{q}+\mathbf{q}'+\mathbf{q}'',\mathbf{G}} \Phi_{i,j,k}^{a,b,c}(0, B, C)}{\sqrt{m_a \omega_n(\mathbf{q}) m_b \omega_{n'}(\mathbf{q}') m_c \omega_{n''}(\mathbf{q}'')}} \cdot \\ & \cdot \mathbf{e}_{n,i}^a(\mathbf{q}) \mathbf{e}_{n',j}^b(\mathbf{q}') \mathbf{e}_{n'',k}^c(\mathbf{q}'') \cdot \exp \{ i [(\mathbf{q} \cdot \mathbf{r}_a + \mathbf{q}' \cdot (\mathbf{r}_b + \mathbf{R}_B) + \mathbf{q}'' \cdot (\mathbf{r}_c + \mathbf{R}_C))] \} \end{aligned} \quad (3.24)$$

The Kronecker delta in eq. (3.24) also accounts for Umklapp scattering if the sum of all wave vector equals an arbitrary lattice vector \mathbf{G} . The variable Z appearing in both expression is the number of unit cells the sum is running over (with $Z \rightarrow \infty$ in the end). Obviously one can calculate the phonon lifetimes from the equations above more or less straightforwardly. In reality, however, a significant complication arises. How do we compute the third-order force constants? If we used a finite differences scheme as for the harmonic force constants, this would mean that we could make use of the last equality in equation (3.22), where one of the derivatives was interpreted as the force on that atom. Still it would be necessary to calculate the changes of that force if two atoms are simultaneously displaced from their equilibrium position. As the systems grow, there are more and more combinatorial choices to pick two atoms and two directions to displace them. In fact, for a system of N atoms in the unit cell there are $\binom{6N}{2}$ combinations. However, this is only the number of combinations for one unit cell. In order to guarantee that the Fourier series in equation (3.24) converges, one has to consider supercells again. If only a $2 \times 2 \times 2$ supercell was found to be sufficient for convergence, this would mean that there are $\binom{48N}{2}$ combinations.

For example, let us consider the relatively small system MOF-508 with 54 atoms in the primitive unit cell. In this unit cell there would be 52 326 combinations that would

take about 46 years in computational time if the single point calculations were carried out with VASP (cf. fig. 3.3 in sec. 3.4.3). For a $2 \times 2 \times 2$ supercell there are already more than $3.4 \cdot 10^6$ combinations which would need $2 \cdot 10^5$ years of computational time considering that calculations with supercells are slower than with primitive cells.

Despite the combinatorial explosion, there is an approach to handle this calculation. If one sets a certain cutoff for the distances up to which atoms are considered to have an influence on the third-order force constants, the number of necessary displacements can be decreased significantly. Also symmetry consideration can spare one some displacement combinations. But still, this approach is tremendously expensive. For that reason, a model to compute the phonon lifetimes from quantities that are related to the third derivatives was employed. This model will be the topic of the following subsection.

3.3.1. Used model for phonon lifetimes

The chosen procedure employs the model of Bjerg et al.[16]. This model uses a number of empirical relations to obtain an approximative expression for the mode dependent phonon lifetime. The first ingredient of the model is an empiric relation for the phonon lifetimes that was found by Slack et al. [26] for the case that the dominating phonon-phonon interaction is Umklapp scattering. In this publication they used equation (3.25) with $\alpha = 2$, $\beta = 3$, but stressed that other values could be better approximations for other systems and temperatures.

$$\tau_n^{-1}(\mathbf{q}) = p(\langle \gamma^2 \rangle) \omega_n^\alpha(\mathbf{q}) \frac{T}{\Theta} \exp \left\{ \frac{-\Theta}{\beta T} \right\} \quad (3.25)$$

In the above equation T is the temperature, Θ a temperature scaling factor that corresponds to the Debye temperature for inorganic systems, $\omega_n(\mathbf{q})$ is the phonon frequency with band index n and wave vector \mathbf{q} . Finally, $p(\langle \gamma^2 \rangle)$ is an empirically determined fitting function that is dependent on the mean squared Grüneisen parameter $\langle \gamma^2 \rangle$. Let us first see, what the mode dependent Grüneisen parameter is, before we consider the mean squared one. In essence, the mode dependent Grüneisen parameter $\gamma_n(\mathbf{q})$ describes how much the phonon frequency $\omega_n(\mathbf{q})$ changes if the system volume V is altered relative to its equilibrium value V_0 . This is stated in equation (3.26), where the last equality follows from the spectral theorem since the squared phonon frequencies are the eigenvalues of the dynamical matrix D . Furthermore, this equality is exactly the way, the mode dependent Grüneisen parameters are calculated in practice. Rather than directly computing the changes of the frequencies, a new matrix M (cf. eq. (3.27)) is constructed by the dynamical matrices of slightly larger and smaller volumes, which is diagonalised. The result is then proportional to the mode dependent Grüneisen parameter.

$$\gamma_n(\mathbf{q}) = -\frac{V_0}{\omega_n(\mathbf{q})} \left. \frac{\partial \omega_n(\mathbf{q})}{\partial V} \right|_{V_0} = -\frac{V_0}{2 \omega_n(\mathbf{q})} \left\langle \mathbf{e}_n(\mathbf{q}) \left| \left. \frac{\partial D(\mathbf{q})}{\partial V} \right|_{V_0} \right| \mathbf{e}_n(\mathbf{q}) \right\rangle \quad (3.26)$$

$$M(\mathbf{q}) = \left. \frac{\partial D(\mathbf{q})}{\partial V} \right|_{V_0} \approx \left. \frac{\Delta D(\mathbf{q})}{\Delta V} \right|_{V_0} \quad (3.27)$$

The Grüneisen parameter is a measure of the anharmonicities in the system. If a crystal would have a totally harmonic PES, then all the Grüneisen parameters would vanish. One can also understand that the Grüneisen parameters are (roughly) related to the third derivatives of the PES because the frequency is proportional to the energy and $\partial V \approx \partial x \partial y \partial z$. So the usage of this quantity is very reasonable to account for anharmonicities.

The mean Grüneisen parameter of order m is defined as the average weighted with the mode heat capacities (cf. eq. (3.10)). In the model of Bjerg et al. $m = 2$ is used to prevent the cancellation of positive and negative Grüneisen parameters what would distort the overall image of the present anharmonicities.

$$\langle \gamma^m \rangle = \frac{\sum_n \int d^3q C_n(\mathbf{q}) (\gamma_n(\mathbf{q}))^m}{\sum_n \int d^3q C_i(\mathbf{q})} \quad (3.28)$$

In the considered model another empirical finding by Slack et al. [15] for the thermal conductivity in noble gas crystals is then used along with the thermal conductivity according to equation (3.9) within the Debye model to find an expression for the fitting function p .

$$p = \frac{1 - 0.514(\langle \gamma^2 \rangle)^{-1} + 0.228(\langle \gamma^2 \rangle)^{-1} \frac{\hbar^2 \langle \gamma^2 \rangle}{k_B \Theta M V^{1/3} c_s}}{0.0948} \quad (3.29)$$

The variables appearing in this equation are the average atomic mass in the unit cell, M , the unit cell volume, V and the speed of sound, c_s , as well as the temperature scaling factor Θ which is the Debye temperature for several reported inorganic systems [16, 27]. The Debye temperature can be calculated rather easily from an arbitrary moment of the phonon frequencies defined with the phonon density of states D according to equation (3.30).

$$\Theta = \frac{\hbar}{k_B} \sqrt[m-n]{\frac{m+3}{n+3} \frac{\langle \omega^m \rangle}{\langle \omega^n \rangle}} \quad \text{with } \langle \omega^j \rangle = \int d\omega D(\omega) \omega^j \quad (3.30)$$

This expression is usually evaluated for $m = 2$ and $n = 0$ - i.e. the second moment of the phonon frequencies divided by a scaling constant.

To sum up, the main ingredient are the mode dependent Grüneisen parameters that represent the anharmonicities of the system. By using the mean squared Grüneisen parameter in equation (3.29), one can calculate the fit function p , the knowledge of which finally allows the computation of the mode dependent phonon lifetimes according to equation (3.25).

It has to be stressed once more that this model was shown several times to be very well applicable to inorganic crystals [16, 27]. Together with the fact that this approach reduces the computational effort dramatically because the lifetimes are obtained from

3. Theory and computational methods

only three phonon band structure calculations at different volumes, this model is very interesting in terms of applications to other systems. Even if the model did not fit too well for a whole class of materials different to those the model was set up for, there would be still parameters to adjust as the variables α and β in equation (3.25), as it was suggested in the original publication [26].

3.4. Computational methods

In order to obtain all the aforementioned quantities, first principle calculations were employed. Nowadays the framework of density functional theory (DFT) is the standard way to perform quantum-mechanical calculations of materials. Since DFT has been intensively reviewed in the last decades, only a very brief summary will be given here that is sufficient to understand the much less well-known density functional tight binding (DFTB) approach of section 3.4.3. A more detailed description of the conceptual ideas and applications of DFT can be found e.g. in [28, 29].

3.4.1. Density functional theory

In DFT the central quantity is the electron density ρ . The total energy of the system was shown by Hohenberg and Kohn [30] to be expressible as a functional of the charge density, where the ground state of the system should result in a charge density which minimises this functional. However, the form of the functional is not known. The framework for solving quantum-mechanical problems with the DFT approach was introduced by Kohn and Sham [31]. They suggested the functional of equation (3.31), where the real problem is mapped onto an auxiliary system of non-interacting electrons. This expression yields the exact solution if the exchange-correlation functional was known. That is where approximation comes into play. The following considerations are based on [29].

$$E_{KS}[\rho] = T_0[\rho] + \int d^3r \rho(\mathbf{r}) \left(V_{ext}(\mathbf{r}) + \frac{1}{2}\Phi(\mathbf{r}) \right) + E_{xc}[\rho] \quad (3.31)$$

In this equation T_0 is a functional representing the kinetic energy of all electrons under the assumption that they do not interact with each other, V_{ext} is the external potential, $\Phi = \int d^3r' \rho(\mathbf{r}')/|\mathbf{r} - \mathbf{r}'|$ is the classical Coulomb potential of a charge distribution and all the unknown, complicated multi-body effects are put into the exchange-correlation energy E_{xc} . In principle, the lack of knowledge of the exact functional is thereby transferred to the lack of knowledge of the exchange-correlation energy functional. In order to use the method, there are numerous approximate functionals available which (empirically) try to describe the $E_{xc}[\rho]$ term in equation (3.31). The functional that is used in all reported DFT results in this thesis is the PBE functional of Perdew, Burke and Ernzerhof [32]. This functional is one of the so-called generalised gradient approximation (GGA) functionals - i.e. it is assumed that the exchange-correlation term is not only a function of the charge density, but also of the gradient of it.

The next step is the introduction of single-particle wave functions (KS orbitals) that yield

the desired density of the system (eq. (3.32)) and fulfill the single-particle Schrödinger equations of equation (3.33).

$$\rho(\mathbf{r}) = \sum_i |\langle \mathbf{r} | \Psi_i \rangle|^2 \quad (3.32)$$

$$\left[-\frac{1}{2} \nabla^2 + v_{KS}(\mathbf{r}) \right] \Psi_i = \varepsilon_i \Psi_i \quad \text{with} \quad v_{KS}(\mathbf{r}) = V_{ext}(\mathbf{r}) + \Phi(\mathbf{r}) + \frac{\delta E_{xc}[\rho(\mathbf{r})]}{\delta \rho(\mathbf{r})} \quad (3.33)$$

It is obvious from the interdependencies above that these equations can only be solved iteratively in order to find the charge density that minimises the Kohn-Sham energy functional E_{KS} . In this so-called self consistent field (SCF) approach, an initial charge density is guessed from the nuclei's position. From that, the KS-potential v_{KS} according to equation (3.33) can be calculated if a certain exchange-correlation energy functional is provided. After that, the single-particle Schrödinger equation can be solved for all KS-orbitals Ψ_i , which yield a new charge density. With the new density one can again compute the KS-potential and so on. The KS-energy is evaluated in every SCF step and the iterative procedure is finished when the energy converges within a certain accuracy. Nowadays, there are many codes available to allow quantum-mechanical calculations with DFT. They essentially differ in how they describe the KS-orbitals and which functionals one can use. One approach that accelerates the calculations, for instance, is the usage of pseudopotentials instead of solving the KS-equations for all the electrons in the system. One particularly efficient way is the projector augmented wave method (PAW) introduced by Blöchl [33], whose work is briefly summarised in the following. The problem is that if one wants to describe wave functions near the nucleus (core states), one usually has to use a large plane wave basis set to account for the strongly oscillating radial functions in the core region. In the PAW approach, linear operators \hat{T} are introduced to map the all-electron (AE) wave functions $|\Psi\rangle$ onto pseudo wave functions $|\tilde{\Psi}\rangle$ that are smoother around the nuclei and decrease the computational effort. These projection operators differ from the identity only in a certain volume around the nucleus (augmentation region Ω_R). That means that both wave functions are equal outside Ω_R . If both, the AE and the pseudo wave functions, are expressed as a linear combination of plane waves $|\phi_i\rangle$ and "pseudo plane waves" $|\tilde{\phi}_i\rangle$, a linear operator \hat{T} can be found:

$$\hat{T} = 1 + \sum_i \left(|\phi_i\rangle - |\tilde{\phi}_i\rangle \right) \langle \tilde{p}_i | \quad (3.34)$$

In the equation above $|\tilde{p}_i\rangle$ are the so-called localised projector functions, which are orthonormal to all pseudo partial waves and usually localised in the augmentation region. Knowing the transformation \hat{T} , it can be used to transform also operators so that expectation values and other observables can be calculated from the pseudo wavefunction and the transformed operators.

3.4.2. Calculation of Raman spectra within DFT

Porezag and Pederson introduced a straightforward way to use DFT to compute infrared intensities (IR) and Raman scattering intensities [34]. The following summary is based

3. Theory and computational methods

on their work. They report that this method is especially suited for GGA functionals, as the results are in much better agreement with experiments compared to LDA results. In Raman spectroscopy visible light is used. The photons of the incident radiation inelastically scatter at the crystal, creating or annihilating phonons, for example, so that the momentum as well as the energy of the photons is altered. Visible light is usually used because the changes of the frequencies (Raman shift) can easily be measured in that range. The absolute momentum change, however, is rather small. As a consequence, one can only image the phonon band structure at the Γ point of the first Brillouin zone. Obviously, it is enough for a DFT Raman spectra calculation to consider the phonon modes at Γ . The displacement \mathbf{u}_i corresponding to the movement of the i^{th} mode can be written as the product of the respective eigenvector \mathbf{e}_i and a dimensionless normal-mode coordinate Q_i . The normal-coordinates are of interest for the vibrational properties of a material.

$$\mathbf{u}_i = Q_i \mathbf{e}_i \quad (3.35)$$

Both, the IR and the Raman scattering intensities, depend on the derivative of an observable quantity with respect to the normal-mode coordinates. The derivatives of a quantity labelled as X with respect to the normal-mode coordinate can be easily expressed by using the derivatives with respect to the atoms' positions (r_μ) and the phonon eigenvectors.

$$\frac{\partial X}{\partial Q_i} = \sum_{\mu} \frac{\partial X}{\partial r_{\mu}} e_{i,\mu} \quad (3.36)$$

In the case of IR intensities X is the electric dipole moment p_k and in the case of Raman scattering the polarisability tensor α_{ij} . For the Raman scattering intensities one has to consider the differential Raman scattering cross section (cf. ref. [34]). From that expression one can find the Raman scattering intensities as a function of the derivatives of α_{mn} under the following experimental convention. The directions of the incident radiation, the polarisation of the light and the detection direction are all perpendicular to each other. The differential cross section was evaluated for this experimental arrangement, but could have been computed for any other as well.

With equation (3.36) one has to compute the derivative of the polarisability tensor with respect to cartesian atomic positions r_p in order to obtain the desired Raman activity respectively intensity. By making use of fundamental dependencies of the polarisability tensor α_{mn} , the electric field ε_m , the forces on atoms F_m , the electric dipole moment μ_m , and the energy E one can find the following relation:

$$\frac{\partial \alpha_{mn}}{\partial r_p} = \frac{\partial^2 \mu_m}{\partial \varepsilon_n \partial r_p} = - \frac{\partial^3 E}{\partial \varepsilon_m \partial \varepsilon_n \partial r_p} = \frac{\partial^2 F_p}{\partial \varepsilon_m \partial \varepsilon_n} \quad (3.37)$$

Especially the last equality in equation (3.37) can easily be exploited to compute the derivatives of the polarisability tensor via numerical methods. One usually calculates how the forces in the system change when electric fields are perturbatively introduced (density functional perturbation theory DFPT).

3.4.3. Density functional tight binding

As it was discussed in section 3.2 one has to make sure that the force constants decay fast enough so that the Fourier transform converges for a given super cell size. This implies that system sizes rather soon become very large and the computations become very often too computationally expensive. In figure 3.3 it can be seen how the computational time scales with the system size for VASP single point calculations. The simulated system was MOF-508 with different super cell sizes up to a $2 \times 2 \times 2$ super cell. Except for the Brillouin zone sampling, all the simulations parameters were kept the same for all system sizes. Even for a rather small super cell ($2 \times 2 \times 2$) the computational effort increases by nearly a factor of 500. Therefore, it is necessary to look for other computational methods, which still can reproduce the desired physical quantities within an acceptable accuracy, but decrease the computational effort significantly.

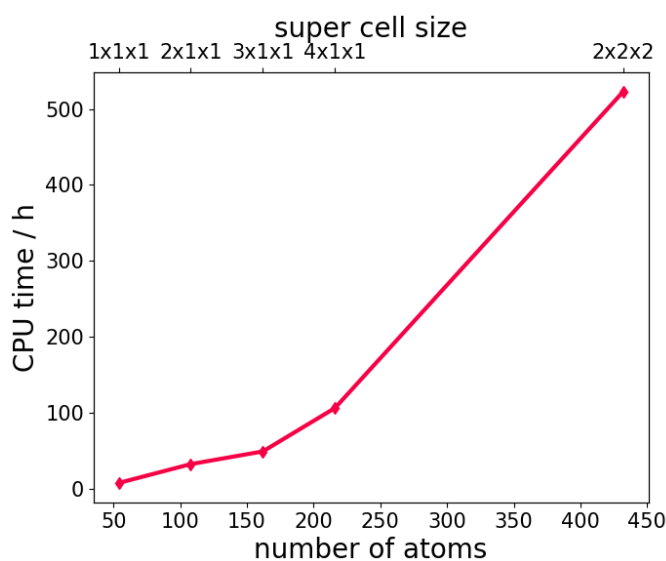


Fig. 3.3: Computational time scaling behaviour for single point calculations of different super cells of MOF-508 with VASP ($\text{EDIFF} = 1\text{E-}8$, $\text{ALGO} = \text{Fast}$, $\text{PREC} = \text{Accurate}$). The Brillouin zone sampling has been adapted to the supercell sizes.

One possible alternative is density functional tight binding (DFTB). Very instructive reviews of the methods can be found for instance in [35, 36]. Only the most fundamental steps will be discussed in this subsection in order to understand the biggest differences to DFT and the capabilities of DFTB. The following summary is inspired by the work of Oliveira et al. [35].

Oliveira et al. [35] derive the DFTB formalism from the Kohn-Sham equations, starting by expressing the electron density ρ as some reference density ρ_0 that is perturbed by a small charge density fluctuation $\delta\rho$.

$$\rho(\mathbf{r}) = \rho_0(\mathbf{r}) + \delta\rho(\mathbf{r}) \quad (3.38)$$

3. Theory and computational methods

Using this ansatz for the density in the KS-equations and Taylor expanding the exchange-correlation functional (cf. eq. (3.39)), one can rearrange the energy functional and ends up with three contributions as indicated in equation (3.40).

$$E_{xc}[\rho_0 + \delta\rho] = E_{xc}[\rho_0] + \left. \frac{\delta E_{xc}}{\delta\rho} \right|_{\rho_0} \delta\rho + \left. \frac{\delta^2 E_{xc}}{\delta\rho \delta\rho'} \right|_{\rho_0} \delta\rho \delta\rho' + \dots \quad (3.39)$$

$$E[\rho_0 + \delta\rho] = E_{band}[\rho_0] + E_{rep}[\rho_0] + E_{fluct}[\rho_0, \delta\rho] \quad (3.40)$$

The term E_{band} is essentially the sum of all the expectation values of all single-particle Hamiltonians \hat{h}_0 of equation (3.33) evaluated for single-particle wave functions Ψ_i (degeneracy n_i) that together give the reference density ρ_0 .

$$E_{band}[\rho_0] = \sum_i n_i \langle \Psi_i | \hat{h}_0[\rho_0] | \Psi_i \rangle \quad (3.41)$$

The second term is referred to as repulsion term E_{rep} . Here the contribution from the Coulomb repulsion of the nuclei will be omitted, which one would have to add to the repulsion term otherwise. The functional derivative of the exchange-correlation energy with respect to the density is written as the exchange-correlation potential $v_{xc}[\rho]$.

$$E_{rep}[\rho_0] = E_{xc}[\rho_0] - \frac{1}{2} \int \int d^3r d^3r' \frac{\rho_0(\mathbf{r})\rho_0(\mathbf{r}')}{\|\mathbf{r} - \mathbf{r}'\|} - \int d^3r v_{xc}[\rho_0(\mathbf{r})]\rho_0(\mathbf{r}) \quad (3.42)$$

In this expression the reference density is simply assumed to be a linear superposition of atomic charge densities around the nuclei α .

$$\rho_0(\mathbf{r}) = \sum_{\alpha} \rho_0^{\alpha}(\mathbf{r} - \mathbf{R}_{\alpha}) \quad (3.43)$$

If this ansatz is inserted in equation (3.42) numerous multi-centres integrals would appear. Usually only terms up to 2-centre contributions are considered.

Although these contributions could be calculated theoretically, the whole repulsion term E_{rep} is usually seen as a fitting quantity (as a function of atomic distances) which is used to bring the energy of DFT in agreement with the band energy from DFTB. The only term that includes the density fluctuation $\delta\rho$ is the fluctuation functional $E_{fluct}[\rho_0, \delta\rho]$.

$$E_{fluct}[\rho_0, \delta\rho] = \frac{1}{2} \int \int d^3r d^3r' \left(\frac{1}{\|\mathbf{r} - \mathbf{r}'\|} + \left. \frac{\delta^2 E_{xc}}{\delta\rho \delta\rho'} \right|_{\rho_0} \right) \delta\rho(\mathbf{r})\delta\rho(\mathbf{r}') \quad (3.44)$$

In the standard DFTB approach, this term is completely neglected. Consequently, there is no need for an iterative solution as the reference density is known (cf. eq. (3.43)). One then expresses the wave functions of equation (3.41) as a linear combinations of atomic orbitals (LCAO) ϕ_n .

$$\psi_{\mu}^{\alpha}(\mathbf{r}) = \sum_n C_{\mu n} \phi_n(\mathbf{r} - \mathbf{R}_{\alpha}) \quad (3.45)$$

Inserting this ansatz in the expression for the band energy, one has now to solve a generalised eigenvalue problem for the expansion coefficients $C_{\mu n}$ which is determined by the Hamiltonian matrix $H_{\mu\nu} = \langle \phi_\mu | \hat{h}_0 | \phi_\nu \rangle$ and the overlap matrix $S_{\mu\nu} = \langle \phi_\mu | \phi_\nu \rangle$. What makes DFTB so fast is the fact that those matrix elements are pre-calculated with DFT and provided in so-called Slater-Koster files. That means that a code solving a problem with the standard DFTB approach only has to read those files, set up the matrices and solve the general eigenvalue problem.

However, the results with standard DFTB are usually not in very good agreement with other first principle calculations. The accuracy is significantly increased, when one considers the fluctuation term and solves the equations self-consistently (self-consistent charge, SCC). In this approach, one approximates the charge fluctuation as superposition of contributions from every atom that are non-directional in space and decay fast with increasing distance from the nuclei. As analysed in [35] this corresponds to a consideration of charge transfer, but changes of the shape of the electronic density are neglected. The fluctuation energy term is approximated by the following equation making use of the additional charges Δq_μ and functions $\gamma_{\alpha\beta}$ that describe the Coulomb and exchange-correlation interaction between those charge fluctuations.

$$E_{fluct} \approx \frac{1}{2} \sum_{\alpha\beta} \Delta q_\alpha \Delta q_\beta \gamma_{\alpha\beta} \quad (3.46)$$

In SCC-DFTB the desired matrix elements are now also dependent on the additional charge Δq_α centred around a nucleus α . For that reason, one has to guess a starting charge fluctuation, read the tabulated matrix elements for standard DFTB and calculate the SCC-DFTB matrix elements with the charge fluctuations assumed. From that, one can solve the generalised eigenvalue problem, which yields the expansion coefficients and, therefore, the wave functions, respectively the charges. Those charge densities differ from the reference density by some fluctuations, which can then again be used to calculate new matrix elements and so on. The flow of actions can be seen schematically in figure 3.4.

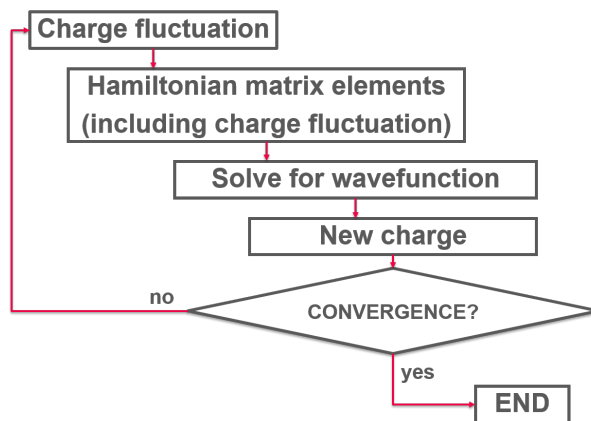


Fig. 3.4: Flow chart of the self-consistent charge approach in DFTB.

3. Theory and computational methods

The fast performance of DFTB compromises the numerous approximations that are made in this approach. DFTB cannot be used to solve every quantum-mechanical problem, but usually performs rather well regarding the calculation of forces and total energies. These are essentially the only quantities that are needed for phonon calculations.

4. Computational details

In the previous chapter the theoretical background for the calculation of vibrational properties and the thermal conductivity has been described. The practical procedure that has been followed is the topic of the current section with detailed reports of relevant input parameters. The general steps to compute the thermal conductivity are shown in the flow chart of figure 4.1. For the (quasi-)harmonic part of the calculation the Vienna Ab-Initio Simulation Package (VASP) and DFTB+ were used. It will become clear during the following discussion, which programme was used to obtain which results. Depending on the used package some parameters have to be converged as a first step of the computational procedure. For the processing of the data produced with the ab-initio codes and the evaluation of the interatomic force constants, the phonons, and the mode Grüneisen parameters the phonopy package was employed. Prior to the phonon calculation, the atomic positions and also the lattice geometry were optimised in order to make sure that the system is in a minimum of the PES such that the harmonic approximation can be applied. Otherwise, the calculation of vibrations yields unphysical results.

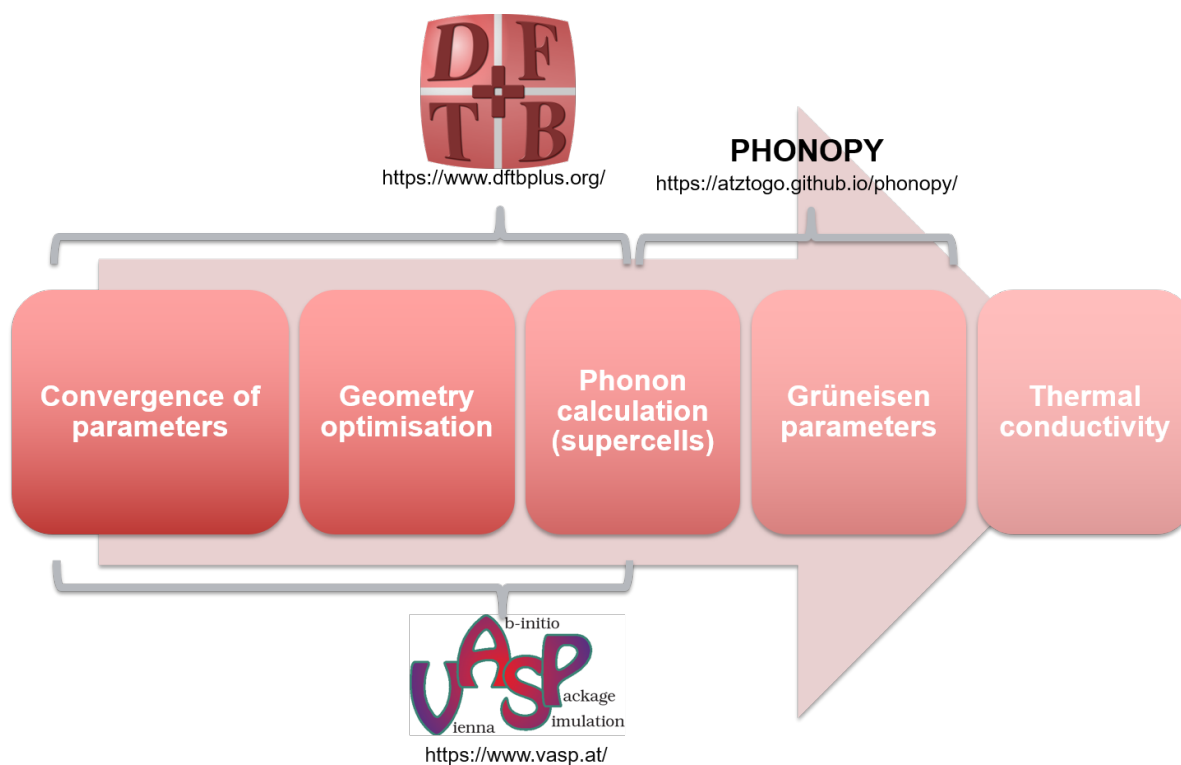


Fig. 4.1: Flow chart of the general steps in order to calculate the thermal conductivity tensor. The code packages used are assigned to certain steps.

The geometries for the various studied IRMOFs were obtained from [37]. The cif-files contain references to the work of Eddaoudi et al. [38]. It has to be mentioned that these geometry files contained the atomic position of the conventional cell with a simple cubic

4. Computational details

Bravais lattice, but more atoms in the system than necessary. All the systems of interest were reduced to primitive cells. For all IRMOFs this means a reduction of the numbers of atoms by a factor of four and the transition from a simple cubic to a face-centred cubic (fcc) Bravais lattice.

For the calculation of vibrational properties, one usually has to use rather tight numerical criteria for the geometry relaxations, for instance. These settings were tested and then consistently used throughout all steps of the computational procedure. The simulation parameters that were used are the topic of the following sections. It shall be emphasised that the results presented in section 5 were obtained with the settings discussed here unless explicitly stated otherwise.

4.1. VASP

VASP (version 5.4.1) [18, 19, 20] was used with PAW pseudopotentials [39] and the PBE functional [32]. A number of tests of different simulation variables were conducted for each system to end up with the same level of convergence in order to guarantee comparability amongst the systems, whereas some special tests were only carried out for the test system MOF-508. The (electronic) \mathbf{k} point convergence and the energy cutoff turned out to be the parameters that could vary between different MOFs, while all the remaining parameters were kept constant.

As a first step of every calculation, the convergence behaviour with respect to the sampling density of \mathbf{k} points in the first Brillouin zone was investigated. It turned out that it is a good practice to converge the total energy of the system to less than 1 meV per atom compared to the converged value with infinitely dense sampling. Except for MOF-5, for which a $2 \times 2 \times 2$ sampling was necessary, for all IRMOFs a $1 \times 1 \times 1$ \mathbf{k} mesh was sufficient to reach this condition, whereas for MOF-508 resp. PMOF-508 a $3 \times 3 \times 2$ resp. $2 \times 2 \times 3$ mesh had to be used. The \mathbf{k} points were generated using the Monkhorst-Pack scheme. The `ENCUT` tag, which controls the energy cutoff for plane waves, was set to 800 eV in all cases. So was the minimisation algorithm `ALGO = Fast` as this is said to perform well in both regimes, at the start and the end of the SCF cycles. In those two phases of the calculation the intermediate solution differs more or less from the converged result. There are algorithms that are more suitable for each of those regimes, with `Fast` being an appropriate compromise.

The following settings were only tested once for MOF-508 and then consistently used in accordance with the results from the tests. The convergence criterion for the self-consistent field (SCF) cycles was set to `EDIFF = 1E-8`. This criterion usually has to be tighter as for ordinary single-point calculations. To avoid aliasing errors, the `PREC` tag was set to `ACCURATE`. The presence of "wrap around" errors was tested by comparing the total energy per atom in the system of different supercells. If aliasing errors were present, these values should change considerably. However, with the settings mentioned up to this point differences of the total energy per atom were calculated differing only on the order of 10^{-5} eV between different supercell sizes, which can be attributed to numerical noise. A rather expensive choice that was absolutely necessary, though, was to evaluate the projection operators in reciprocal space via `LREAL = .FALSE.` because the

real space evaluation tends to yield negative (imaginary) frequencies more often. Moreover, Gaussian smearing (`ISMEAR = 0`) with a smearing parameter of `SIGMA = 0.05 eV` was used.

The impact of van der Waals (vdW) interactions was tested by calculating the phonon frequencies at the Γ point with the Tkatchenko-Scheffler method [40] (`IVDW = 2`) and without any correction. Since the maximum relative differences of the low-frequency modes were only in the order of 1 %, the influence of vdW interaction was, therefore, neglected for all calculations. Due to the fact that there are recent discussions about the quality and efficiency of different vdW corrections within DFT [41, 42, 43], this decision was made to eliminate the influence of this further parameter as the changes are expected to be very small. Besides, for larger systems than MOF-508 where the linkers are separated from each other by even longer distances, the influence is assumed to be even smaller.

Once it has been assured that the general simulation parameters were chosen in a reasonable way, the next step was to optimise the atomic position in order to move the system to a minimum of the PES, where the forces - i.e. the gradients of the PES - vanish. Since this criterion can never be fulfilled exactly with numeric methods, one has to set a maximum residual force that is allowed to remain without altering the reliability of the results. A rule of thumb is to relax the atoms to a maximum residual force of $1 \text{ meV}/\text{\AA}$. To estimate the influence of the quality of relaxation on the phonon frequencies, MOF-508 was once relaxed to a maximum remaining force of $1.54 \cdot 10^{-4} \text{ eV}/\text{\AA}$ and once even further to $2 \cdot 10^{-5} \text{ eV}/\text{\AA}$. It turned out that the biggest change in frequencies was in the range of 0.2 cm^{-1} (approx. 0.5 %). However, the relaxation takes considerably longer if the forces are reduced to such a small threshold. The dependence of the computational time on the maximum remaining force was seen to show exponential behaviour. In order to save resources, the price of a relatively small loss of accuracy was paid. The maximum force for the geometry relaxations was set to be $1 \text{ meV}/\text{\AA}$ for all reported results. For a similar reason, the VASP tag `ADDGRID` was not used, which introduces a finer mesh for the evaluation of quantities like the compensation (or augmentation) charges. Although if set to `.TRUE.`, the numeric noise on the forces is supposed to be reduced, no significant changes in the phonon frequencies were observed, while the computational times showed the tendency to increase slightly. The optimisation of the coordinates inside the unit cell was done with the `GADGET` code implemented by Bucko et al. [44], usually showing faster convergence to the PES minimum than the optimisation algorithms available within VASP (`IBRION`) by making use of internal coordinates instead of cartesian ones. `GADGET` performs the optimisation independently, while VASP only yields energies and forces as a result of single-point calculations. Moreover, it allows to consider constraints and system specific initialisation of the second derivatives of the PES (Hessian matrix). The relaxations with `GADGET` were performed with an iterative update of the Hessian matrix according to the Broyden-Fletcher-Goldfarb-Shanno (BFGS) method, keeping the lattice vectors constant. The optimisation of the unit cell was achieved in a different way described in section 4.3. For systems with large numbers of atoms in the unit cell, the efficiency of the relaxations using `GADGET` was observed

4. Computational details

to significantly drop due to the rather slow convergence of the SCF cycles starting from scratch. In order to resolve this unfavourable behaviour, the wave functions from a previous relaxation step were saved (`LWAVE = .TRUE.`) and read as an initial guess for the next one (`ISTART = 1, 2`). This accelerated the calculations by up to a factor of 10.

The calculation of the Raman intensities according to Porezag et al. [34] was carried out with an implementation written in Python for VASP by Fonari et al. [45]. The code makes use of DFPT calculations with VASP (`IBRION = 8`) in order to calculate the dielectric tensor (`LEPSILON = .TRUE.`) which is evaluated by the `raman_vasp` code to obtain the Raman scattering activities separately for every single phonon mode at Γ . Therefore, one needs to know the frequencies at the centre of the Brillouin zone already, before the Raman calculation can be started. Since the phonon calculations were conducted in an equivalent way for both, VASP and DFTB+, the procedure is described in section 4.4.

4.2. DFTB+

For most of the studied systems, the supercells necessary to make the force constants converge and yield physically reasonable phonon frequencies are too big to be calculated using VASP. Therefore, the DFTB code DFTB+ (version 18.1) [46] was used to describe such large systems. The most important influence factor for this package is the choice of the Slater-Koster files. Especially for the MOFs containing Zn, the parameters set "znorg-0-1" [47] could have been used, since these parameters have been tested in various studies. However, in order to guarantee comparability between the results with MOFs containing different metals, this parameter set could not be used, since it does not contain parameters for pair interactions involving Ca or Mg. Therefore, the "3ob-3-1" parameters were used [48, 49, 50]. Based on this Slater-Koster set, some parameter files were replaced by those of the "3ob:freq-1-2" set [51]. This set provides a modification of the ordinary 3ob set, which is supposed to improve vibrational properties involving carbon. All reported results have been calculated with this set of Slater-Koster files.

As a first step of the calculation of the thermal conductivity of every system the convergence of the total energy with respect to the Brillouin zone sampling density was tested. For all studied IRMOFs it was found to be sufficient to use the Γ point only for the electronic calculations.

Actually, the 3ob Slater-Koster files allow the application of the DFTB3 method (see appendix A.2). However, for all the studied IRMOFs there was hardly any difference observed in the phonon modes obtained with ordinary DFTB and DFTB3, except for a slight increase of computational time. For economic reasons, this additional correction was neglected for the presented results.

All calculations were conducted in the self-consistent charge (SCC) mode of DFTB+ with a required convergence of `ScdTolerance = 1E-10`. Maximum angular momenta considered for the elements were $l = 0$ (s) for hydrogen, $l = 1$ (p) for oxygen, nitrogen, carbon, calcium, and magnesium and $l = 2$ (d) for zinc.

To be consistent with VASP and to allow future comparisons, vdW corrections were also

neglected in the DFTB+ calculations.

Geometry optimisations were carried out using the conjugate gradient algorithm from scratch (`Driver = ConjugateGradient{}`) allowing all atoms to move (`MovedAtoms = 1:-1`) up to a maximal residual force (`MaxForceComponent`) of 10^{-8} eV/Å. Since the lattice relaxations in DFTB+ are somewhat inefficient, the optimisations have been conducted with fixed lattice vectors (`LatticeOpt = No`). The methodology to find the equilibrium volume for the systems is the topic of the next section.

4.3. Lattice parameter relaxations

This section deals with the way in which the cell geometries were optimised in both DFTB+ and VASP calculations. There are two main reasons why the optimisation of the lattice vectors was outsourced, so to say. Firstly, in VASP one has to increase the energy cutoff by at least a factor of 1.3 in order to account for the distortion of the cell and the change in the plane wave basis set that results from that. The increased cutoff slows down the calculations considerably. Secondly, it was found easier to impose certain constraints on the cell shapes. In principle, it is possible to force VASP to let the cell relax in a certain shape when the volume is optimised using the tag `ISIF = 3`, for instance. For this, however, the code has to be changed and recompiled, which was found to be too tedious for every different Bravais lattice. The location where such a change has to be performed is in the file `constr_cell_relax.f90`. Inside this subroutine the cell force `FCELL` is evaluated and returned for the next step of the optimisation algorithm. If one manually sets certain components of this 3×3 array to 0, the respective components of the lattice vectors will feel no force and will not change during the relaxation. In a similar way one could also impose certain relations between the lattice vectors etc.

It was found that the easiest and most efficient way to account for the conservation of symmetry of the cell during the relaxation was to separate the lattice parameter from the geometry optimisation. This was achieved by fitting the PES with respect to the lattice parameters of the respective cell. For an fcc Bravais lattice only one variable is necessary, for instance, or three for an orthorhombic system. Close to the minimum of the PES it can be fitted to a multidimensional parabola according to equation (4.1), where $x_{i/j}$ are the m variables of interest ($m = 1$ for fcc, $m = 3$ for orthorhombic etc.). The matrix A_{ij} with $m(m+1)/2$ independent components as it is symmetric, the vector b_i with m components and c are the fit parameters of the parabola. Note that the sum convention is used.

$$f(\mathbf{x}) = \frac{1}{2}A_{ij}x_ix_j - b_ix_i + c \quad \text{with } A_{ij} = A_{ji} \quad (4.1)$$

From this equation, the minimum can be found by solving for the roots of the gradient of f shown in equation (4.2). The largest m value conceivable is 9; so the solution vector of equation (4.2) can be easily found by inverting the matrix A_{ij} .

$$\nabla f(\mathbf{x}) \stackrel{!}{=} 0 \Rightarrow A_{ij}x_j = b_i \quad (4.2)$$

4. Computational details

Geometry relaxations were performed for a set of fixed cell parameters to sample the PES with respect to the relevant lattice parameters. The obtained data was fitted to a general parabola according to equation (4.1) within the framework of Bayesian probability theory in order to obtain (the probability density of) the lattice parameters at the minimum of the PES. This approach provides a convenient way of estimating the uncertainty of the found optimal lattice vectors, since the entire probability density functions are computed. If, for example, the variance of these probability densities turns out to be unacceptably large, the formalism is used to calculate the next set of lattice parameters, for which a "measurement" should be conducted in order to gain the largest amount of information and decrease the uncertainty (expected utility). With this new data point the fit is performed again and possibly the new variance is small enough to be accepted. If not, the procedure is repeated, and so on. The approach is based on [52, p. 491ff].

4.4. Phonon calculations

VASP respectively DFTB+ was used to compute the phonons via the finite differences approach introduced in section 3.2.1. Therefore, atoms have to be displaced one by one in each direction twice and the resulting forces are computed. The geometries containing the displacements were generated with the phonopy package (version 1.13.0) [53]. There is an interface in phonopy implemented for VASP that directly can create supercell geometries from the primitive unit cells. For DFTB+ phonon calculations, a slightly more complicated procedure was necessary due to the lack of a phonopy interface. The geometry files of DFTB+ were translated into VASP POSCAR files by a Python script. Phonopy was run on those artificial POSCARs and created the displacements, which were re-translated to the geometry format for DFTB+.

During the generation of the displacements with phonopy one can save a lot of computational resources by making use of the command option `--tolerance`. By doing so, one can influence the resulting number of displacements necessary to calculate because phonopy internally detects the symmetries of the systems and uses them to decrease the effort accordingly. If the tolerance is set to rather high values, more symmetries will be recognised and fewer calculations are needed. This can sometimes reduce the effort significantly depending on the intrinsic symmetries of the system. The general approach was to use a tolerance so that the experimental space group is reproduced. For example, the necessary number of displacements of MOF-5(Zn) relaxed with VASP would have been 636 (= number of atoms in the unit cell times six) if the default tolerance (10^{-5}) had been used. This is equal to saying that there are no symmetries in the crystal (space group P1). By increasing the tolerance to $5 \cdot 10^{-3}$, however, the experimental space group $F\bar{m}3m$ is found, resulting in only 19 displacements. Interestingly, the geometries relaxed with DFTB+ showed the experimental symmetries even for the default tolerance, making it unnecessary to increase it manually. Apparently, the conjugate gradient algorithm of DFTB+ yields geometries with the tendency to keep the initial symmetry, whereas GADGET distorts the systems more significantly. In future calculations it should be taken into consideration to perform an additional optimisation step after the relaxation

with GADGET. For such a step, a different optimisation method like VASPS’s conjugate gradient algorithm should be used, which could possibly result in a better preservation of the symmetries.

It was tested how the different symmetry tolerances of phonopy alter the Γ frequencies of the test system MOF-508. The biggest absolute change turned out to be less than 0.1 cm^{-1} , the biggest relative change about 0.4 %

After all the forces on the atoms in the system have been calculated, phonopy reads and collects them in the `FORCE_SETS` files. For DFTB+ calculations the output had to be translated manually to a format known to phonopy via one of its interfaces. It has to be stressed that all reported phonon band structures and phonon densities of states, which describe the whole first Brillouin zone, were obtained by DFTB+ calculations.

The supercell sizes necessary in order to converge the force constants so that no negative frequencies were obtained for band structures etc. can be found in table 4.1. The last column also shows the number of atoms in the respective supercells, rationalising why this type of calculations are very expensive using DFT programmes like VASP. The uncertainties of the found lattice constants with the approach described in section 4.3 are the square roots of the respective probability density functions. The definition of the lattice parameter a can be found in equation (5.4).

Tab. 4.1: Systems with converged force constants allowing to calculate phonons for generic \mathbf{q} points. The supercell size necessary for this, the number of atoms in the primitive (N) and supercells ($N_{\text{supercell}}$) as well as the lattice parameters according to eq. (5.4) are listed.

System	N	$a / \text{\AA}$	supercell size	$N_{\text{supercell}}$
MOF-5(Zn)	106	13.189 ± 0.001	$3 \times 3 \times 3$	2862
MOF-5(Ca)	106	13.798 ± 0.003	$3 \times 3 \times 3$	2862
MOF-5(Mg)	106	13.165 ± 0.001	$2 \times 2 \times 2$	848
IRMOF-14(Mg)	190	17.454 ± 0.002	$3 \times 3 \times 3$	5130
IRMOF-131(Mg)	58	11.452 ± 0.001	$5 \times 5 \times 5$	7250
IRMOF-132(Mg)	70	14.043 ± 0.001	$5 \times 5 \times 5$	8750

The general transformation from a primitive unit cell described by a matrix P , which contains the primitive lattice vectors as rows, to a supercell, described by a matrix S (again containing the supercell vectors as rows) is done by means of a transformation matrix M according to equation 4.3.

$$S = M^T P \quad (4.3)$$

For the supercells used in all systems the transformation was diagonal - i.e. $M_{ij} = n_s \delta_{ij}$. For cubic systems like the ones studied there is no reason to use non-diagonal transformation matrices. This could be different for MOFs with different symmetries.

Note that for all frequencies the acoustic sum rules are imposed by setting `FC_SYMMETRY`

4. Computational details

= `.TRUE.` in phonopy. For the systems shown in the table above, many phononic properties can then be calculated, once the force constants are made sure to be converged. Further quantities that are needed for the calculation of the thermal conductivity or the analysis are the group velocities (`GROUP_VELOCITY = .TRUE.`), the eigenvectors (`EIGENVECTORS = .TRUE.`), and the Debye frequency calculated by phonopy by a fitting procedure of the first quarter of the DOS to a quadratic function according to the Debye model (`DEBYE_MODEL = .TRUE.`). For the calculation of the group velocities, the symmetric mesh generation had to be switched off (`MESH_SYMMETRY = .FALSE.`), since vectorial properties are not necessarily the same for (irreducible) \mathbf{q} points in the first Brillouin zone, whereas scalar quantities are equal. In other words, for frequencies or mode Grüneisen parameters it is sufficient to consider only the irreducible part of the first Brillouin zone. Weights can be assigned to those quantities (in order to calculate expectation values, for instance) depending on how often they would occur in the whole first Brillouin zone. This is not true for vector quantities like the group velocities. There are two possibilities to obtain the right group velocities of the whole first Brillouin zone: use the results of the irreducible part and properly apply the respective symmetry operations, or consider the whole first Brillouin zone in the first place so that all weights are the same.

4.5. Phonon lifetimes

The calculation of the phonon lifetimes was carried out according to the earlier described model of Bjerg et al. (cf. sec. 3.3.1). The necessary ingredients can be seen in equation (3.25). The frequencies are already known, so the next thing is to calculate Θ . In the correct derivation from the Debye model, this variable is the Debye temperature, which can be calculated from (arbitrary) momenta of the phonon DOS according to equation (3.30). However, Bjerg et al. rescaled this temperature with $N^{-1/3}$ (N ... number of atoms in the unit cell) in order to obtain better results. Since this scaling factor was introduced with relatively little justification, another definition for Θ was used. Because of the fact that there are only acoustic bands in the Debye model, people attempt to define the analogue of the Debye temperature for real systems by considering only modes up to the flattening out of the acoustic bands [54]. A similar approach was tried for determining Θ by which the right orders of magnitudes (according to the work of Huang et al. [55, 56]) for the thermal conductivity could be reproduced. The procedure is to find out the highest frequency ν_{cut} from the band structure at which an acoustic band flattens out. Subsequently, the integrals in equation (3.30) are truncated at this limiting frequency. The resulting Θ is then referred to as a temperature scaling factor rather than as Debye temperature.

The next step is to determine $p(\langle\gamma^2\rangle)$ from equation (3.25). There the temperature scaling factor appears again. Further parameters are the average mass per atom in the unit cell M , the system volume V and the speed of sound c_s . While the first two quantities can be easily determined from the atomic masses respectively the lattice vectors, the speed of sound is calculated from the Debye frequency ω_D via the following equation, involving the number of atoms in the unit cell N .

$$c_s = \frac{\omega_D}{\sqrt[3]{6\pi^2 \frac{N}{V}}} \quad (4.4)$$

In principle, the Debye frequency and temperature describe the same physical concept, just with different units, so that the one quantity can be directly converted to the other (with \hbar/k_B). However, the results obtained with the lifetime model were better compared to the results reported in [55, 56] if for the Debye frequency ω_D the value calculated with phonopy was used. The way this is done is by fitting the first (lower-frequency) quarter of the DOS to the quadratic shape of the Debye model and extracting the maximum frequency using normalisation conditions. Since the quality of the fit depends on the number of \mathbf{q} points that are sampled in the first Brillouin zone, the convergence of the obtained Debye frequency had to be studied. Usually, the value does not change above $20 \times 20 \times 20$ meshes. The converged values for ω_D were then used for further calculations.

Tab. 4.2: Quantities necessary to calculate the phonon lifetimes for the studied systems.

All listed values were obtained from DFTB+ calculations.

$V \dots$ primitive unit cell volume $M \dots$ average atomic mass in the unit cell
 $\nu_{cut} \dots$ truncation frequency for Θ $\Theta \dots$ temperature scaling factor (eq. (3.30))
 $\nu_D \dots$ Debye wavenumber (phonopy)

System	$V / \text{\AA}^3$	M / u	$\nu_{cut} / \text{cm}^{-1}$	Θ / K	ν_D / cm^{-1}
MOF-5(Zn)	4588	14.52	22.7	33.12	1201
MOF-5(Ca)	5254	12.61	35.6	50.61	1223
MOF-5(Mg)	4563	11.42	40.5	54.25	1178
IRMOF-14(Mg)	10634	10.29	19.3	25.90	1208
IRMOF-131(Mg)	3004	15.49	61.0	72.10	912
IRMOF-132(Mg)	5539	14.90	50.0	52.45	1071

The final ingredients are the mode Grüneisen parameters, from which the mean squared Grüneisen parameters (MSGP) can be calculated according to equation (3.28). Phonopy provides a quite convenient way of computing the mode Grüneisen constants by finite differences. The phonon calculation (with the necessary supercell size) is repeated at slightly increased and decreased volumes. For that, the atomic position for the fixed new lattice vectors have to be relaxed before. In total, there are three dynamical matrices available, from which the mode Grüneisen parameters are calculated using equation (3.26). The volumes were changed isotropically, i.e. by scaling the lattice vectors with a constant close to unity. For MOF-5(Mg), MOF-5(Ca) and IRMOF-14(Mg) the lattice vectors were rescaled by a factor of $(1 \pm s)$ with $s = 0.003$, resulting in total volume changes of about 0.9 %. Interestingly, for systems that later turned out to have larger mean squared Grüneisen parameters, negative frequencies tended to appear for the decreased volumes preferentially, suggesting that the volume has been decreased too much. The parameter s had to be reduced down to a minimum of 0.0001 for IRMOF-131(Mg)

4. Computational details

and IRMOF-132(Mg).

All the important properties for the computation of the phonon lifetimes - except for the mode Grüneisen parameters - are summarised in table 4.2.

5. Results and discussion

By making use of the methods and procedures described in sections 3 and 4, the following results were obtained. As a first step, the harmonic ingredients of equation (3.9) are in the focus, as they determine both the group velocities and the heat capacities. The chosen method to investigate some vibrational properties depending on different constituents and to verify the results also experimentally was to simulate powder Raman spectra for some systems within the assumptions introduced in section 3.4.2. Since theoretical calculations do not necessarily represent the real physical world, it is, of course, necessary to verify theoretical results by experimental measurements. The results will be discussed in section 5.1. Raman scattering spectroscopy is not the optimal method to check the reliability of the simulations for several reasons that will become clear, but it is sufficient for first tests.

Due to the huge computational effort for the large systems necessary to yield physically reasonable vibrational properties, it was at some point not possible to stay with the DFT code VASP anymore. In the least expensive phonon calculation of this study already a supercell containing 848 atoms had to be considered. The method was changed to the much cheaper approach of DFTB using the DFTB+ package. Of course, this step has to be justified. One will usually expect DFTB results to be less accurate than results obtained with DFT. Therefore, in subsection 5.2 some results for the Γ frequencies obtained with the two methods are compared. By comparing the DFTB to the DFT results, which were compared to experimental data, one indirectly is able to draw conclusions, how realistic the vibrational modes obtained with DFTB+ really are.

Once the accuracy of the vibrational modes has been discussed, as a next step, the phonon lifetimes and the thermal conductivities can be calculated with the quasi-harmonic approach described above. However, a last converge issue has to be resolved before, which concerns the sampling density of \mathbf{q} points in the first Brillouin zone. For that reason subsection 5.3 will start with the description of how Bayesian probability theory was used to find the converged values for the thermal conductivity for infinitely dense meshes.

The last part of this section will then deal with the influences different constituents (organic linkers and metallic nodes) have on the thermal conductivity obtained with the described approach. In order to gain some insight into the most important effects, a detailed analysis of all the physical quantities that contribute to the thermal conductivity will be presented and discussed. In that spirit, the phonon density of states and band structures, the group velocities, the heat capacities as well as the phonon lifetimes will be analysed.

To sum up, the first step is to verify the Γ frequencies by means of comparisons to experimental Raman scattering data. Secondly, the comparison of DFT and DFTB results is necessary to justify the transition to this usually less accurate method. Finally, the results of the thermal conductivity for different systems will be discussed in detail and all relevant components are analysed.

For all the shown results the setting described in section 4 are used unless explicitly stated otherwise.

5.1. Raman spectra

As implied above, Raman scattering spectroscopy is not the optimal method to verify the ingredients for calculating the thermal conductivity. The shortcoming of this method is that visible light is used, which, on the one hand, guarantees better detectability of the Raman shift, but, on the other hand, limits the investigated region to the Brillouin zone centre. Essentially, only the frequencies at Γ can be measured. This is not optimal in the sense that actually one would need to experimentally test all the occurring frequencies as well as their dependencies on the wave vector \mathbf{q} , which would additionally allow to compute group velocities. The best experiment would thus be inelastic neutron scattering which would yield the complete phonon band structure.

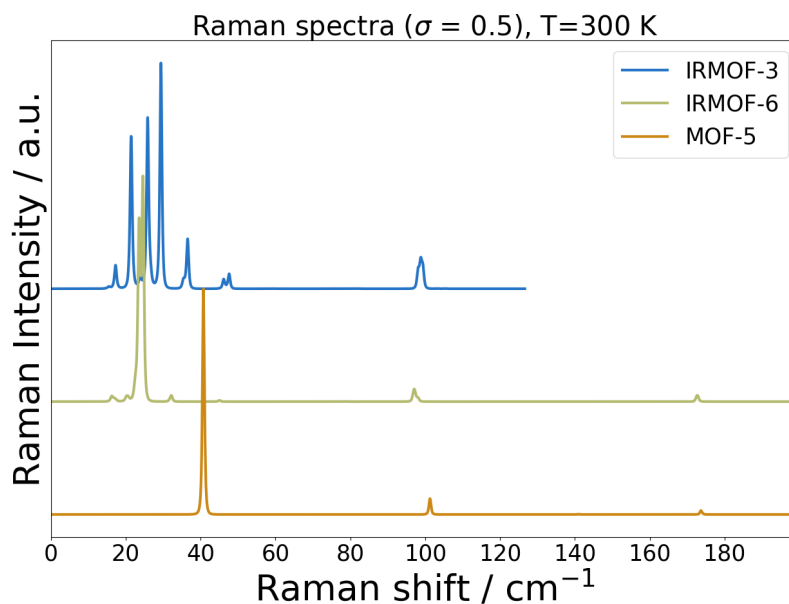
However, since neutron scattering experiments are quite expensive, an alternative method was looked for. The biggest limitation for the whole pool of experimental methods being capable of measuring vibrations in crystals or molecules was the desired measurement range. Doubtlessly, there are a lot of spectroscopic methods available which would be of not much use for our purpose. The reason for that is the following: the phonon modes with the lowest frequencies usually contribute the most to the thermal conductivity of a crystalline system. Therefore, the biggest challenge is to find an experimental setup that is able to measure in this region of very low frequencies. Obviously it would make no sense to test the simulations' accuracy in frequency regions spectroscopic methods can typically investigate, since these are not of high importance for the thermal conductivity at the end of the day. Considering all the constraints discussed above, there are only few groups in the world that have the sufficient equipment to conduct such experiments. One of those is the group of Elisabetta Venuti and Raffaele Guido Della Valle at the University of Bologna, Italy. They have a Raman scattering spectrometer available with the help of which one can at least test the accuracy of phonon modes at the Γ point of the first Brillouin zone. This provides a useful first check if the simulations are far from reality or not. One can estimate from the thermal energy at room temperature ($k_B T \approx 25$ meV) that especially the phonon modes with a frequency of up to about 200 cm^{-1} are important due to thermal occupation. Approximately this frequency range is of experimental interest.

For the purpose of experimental verification, the (powder) Raman spectra for some MOFs were calculated with VASP and the `vasp_raman` implementation. Another group which we collaborate with is the group of Paolo Falcaro at the Institute of Physical and Theoretical Chemistry at the Graz University of Technology, who synthesised two of the systems (MOF-5(Zn) and IRMOF-3(Zn) plus a mixture of both). The MOFs were sent to Bologna where the Raman scattering experiments were conducted.

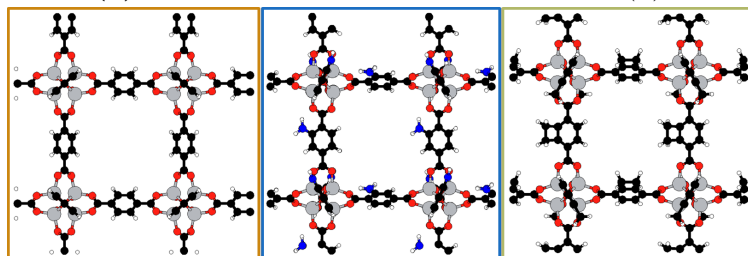
Unfortunately, the measurements were still not finished the day this thesis was finalised. So the comparison to experiments has to be postponed to later work. What can be done, however, is to discuss the results obtained in the simulations.

As they were not limited by the level of difficulty of any synthesis, Raman spectra were calculated for more than those systems. Spectra for MOF-5(Zn), IRMOF-3(Zn) and IRMOF-6(Zn) were computed. Both the spectra and two-dimensional projections of the crystals' geometries can be seen in figure 5.1. As it is shown, in IRMOF-6 one can find

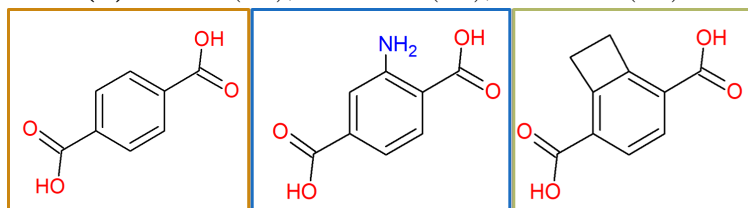
an additional four-membered ring at one side of the organic linkers and an amino group substituted in the case of IRMOF-3. Due to this substitutions, the symmetry of the system is decreased compared to that of MOF-5. This is the reason why one can find considerably more peaks for IRMOF-6 and even more for IRMOF-3.



(a) Raman spectra for the MOFs seen in (b).



(b) MOF-5(Zn), IRMOF-3(Zn), IRMOF-6(Zn)



(c) linkers used in MOF-5, IRMOF-3, and IRMOF-6

Fig. 5.1: Raman spectra for some IRMOFs calculated with the Raman-VASP implementation according to [45]. The data were broadened with a broadening parameter $\sigma = 0.5 \text{ cm}^{-1}$ according to eq. (5.2). Colouring scheme: red...oxygen, black...carbon, blue...nitrogen, white...hydrogen, grey...zinc.

5. Results and discussion

Consider the linker in IRMOF-6. By adding the additional two carbons and the four hydrogen that make up the four-membered ring, the symmetry is reduced since the long molecular axis is no longer a symmetry axis. In the case of IRMOF-3 the decrease in symmetry is even more distinct. By adding the amino groups neither the long molecular axis nor the axis orthogonal to it are symmetry axes. This reduction of symmetries is the reason why more modes correspond to movements for which the polarisability tensor changes with respect to the normal-mode coordinates. Before some of the most dominant modes will be discussed, it should be mentioned that the original Raman activities obtained from the Raman-VASP implementation have to be multiplied with the following function according to [34, 57] and [58, p. 155] to calculate the intensities.

$$\Phi(\nu, T|\nu_{in}) \propto \frac{(\nu_{in} - \nu)^4}{\nu} (f_{BE}(\nu, T) + 1) \quad (5.1)$$

By doing so, one accounts for the thermal occupation of the phonons and the frequency dependence of the intensities relative to the frequency of the incoming light ν_{in} . For the experiments a laser emitting light with a wavelength of 647.1 nm was used. This corresponds to a wavenumber of $\nu_{in} = 15454 \text{ cm}^{-1}$. Furthermore, the original delta-shaped intensities were broadened with a Lorentzian function according to equation (5.2) in order to account for finite lifetimes of the states.

$$L(\nu, \nu_0, \sigma) = \frac{1}{\pi} \frac{\sigma}{\sigma^2 + (\nu - \nu_0)^2} \quad (5.2)$$

Animations of selected Raman active phonon modes can be downloaded from https://www.dropbox.com/sh/1w0ioebya6y06do/AAD8S00qExe-KcDbRd_hmNXza?dl=0. Several further interesting features can be seen in the Raman spectra. For example, one can see a peak around 100 cm^{-1} that appears at about the same frequency in all MOFs in figure 5.1. The constituent that all three systems (MOF-5(Zn), IRMOF-3(Zn) and IRMOF-6(Zn)) have in common is the metallic node. Therefore, it is likely that this peak corresponds to a Raman active mode that is related to vibrations of the node. Indeed, this can be found when the vibrations are visualised. This mode corresponds to some kind of breathing mode of the metallic nodes, where the linkers are only moved as rigid parts. This slight motion of the linkers is most probably the reason, why the frequency of that peak is somewhat reduced in the case of IRMOF-6, which has the heaviest linkers due to the two additional carbon and hydrogen atoms compared to MOF-5. For IRMOF-3, where the additional mass due to the substituted amino group is not that large, the frequency decrease is smaller. Another mode that does not seem to change between the systems lies around a frequency of 174 cm^{-1} . Although this frequency range was not calculated for IRMOF-3 for reasons of resources, it can be seen from respective animations of the modes of MOF-5 and IRMOF-6 that this vibration corresponds to a nearly pure oscillation within the metallic node. The vibration is nearly completely localised in the modes without any significant participation of the linkers. Especially the last discussed vibrational mode is very unlikely to contribute much to thermal conductivity due to the localised nature of the oscillation. Localisation can also be observed in another set of modes. The biggest peak of MOF-5

at about 40 cm^{-1} corresponds to a torsional mode of the organic linkers around their long molecular axes. Similar modes can be found around 24 cm^{-1} for IRMOF-6 and in a region from 25 to 29 cm^{-1} for IRMOF-3 (where there are more similar vibrations due to the broken symmetry). The shift of this torsional frequency between the systems can be estimated to 0th order from classical mechanics, where the squared eigenfrequency of a torsional oscillator is given by the ratio of the (torsional) spring constant C_φ and the torsional moment of inertia I_T . When one assumes the torsional spring constants to be unaltered for this vibration between the systems, one can compute the expected ratio between the two frequencies $\nu_{i/j}$ of two systems labelled with i , j depending on their moments of inertias $I_{T,i/j}$.

$$\frac{\nu_i}{\nu_j} = \sqrt{\frac{I_{T,j}}{I_{T,i}}} \quad \text{with} \quad I_{T,k} = \sum_n m_n r_{\perp,n}^2 \quad (5.3)$$

In the equation above $r_{\perp,n}$ is the distance of the atom with mass m_n perpendicular to the rotation axis, which is always supposed to be exactly the long molecular axis of the linkers - i.e. the axis defined by the carbon atoms of the linker that are directly bonded to the two oxygen atoms. If one computes the frequency ratio by calculating the torsional moments of inertia for all three linkers and compares those values to the ratios of the phonon frequencies involved, rather acceptable agreement can be found (see table 5.1).

Tab. 5.1: Frequency ratios of the torsional modes localised in the linkers. Comparison between the calculated ratio from eq. (5.3) and the direct ratio of the phonon frequencies calculated using VASP.

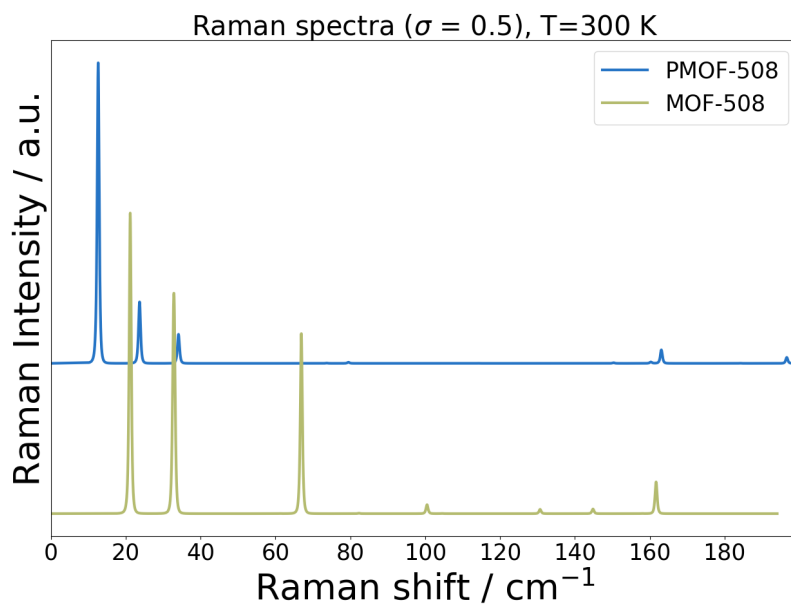
system relative to MOF-5	$\frac{\nu_i}{\nu_{MOF-5}}$ from eq. (5.3)	$\frac{\nu_i}{\nu_{MOF-5}}$ from direct division
IRMOF-6	1.82	1.74
IRMOF-3	1.55	1.51

This shows that these modes can be treated as localised vibrations where the nodes act as rigid boundaries such that one can use classical mechanics to estimate the frequency shifts with different linkers. The remaining small deviations have basically two origins. Firstly, for heavy substituents the axis of rotation will not be the long molecular axis, but another one slightly shifted towards the centre of mass. This will decrease the moment of inertia and, therefore, decrease the calculated frequency ratio a bit, approaching the observed ratio. Secondly, the interatomic force constants are not exactly the same in all three systems.

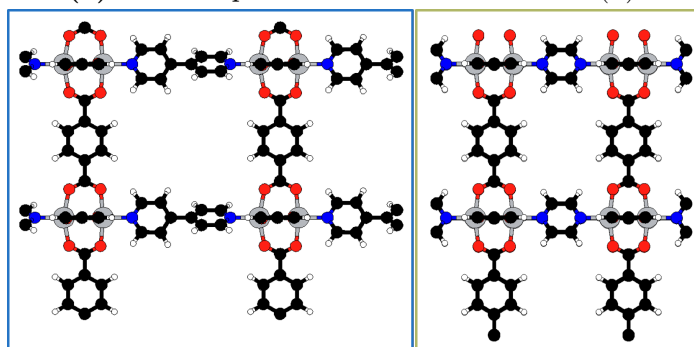
Two further systems that do not belong to the family of IRMOFs due to their anisotropic structure were also investigated in terms of their Raman spectra. Two-dimensional projections of those MOFs as well as the calculated powder Raman spectra at 300 K can be found in figure 5.2. One of the systems is MOF-508 which has appeared at some

5. Results and discussion

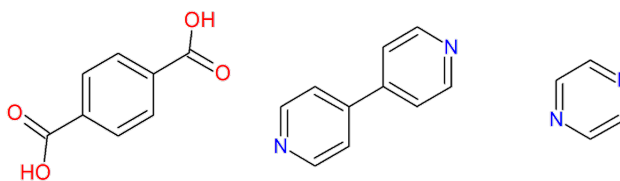
points (scaling of computational time in fig. 3.3; MOFs with cavities in fig. 2.1(b)) in this thesis already.



(a) Raman spectra for the MOFs seen in (b).



(b) MOF-508, PMOF-508



(c) linkers appearing in the two MOFs: terephthalic acid (PCB), 4,4'-bipyridine (44BP), pyrazine

Fig. 5.2: Raman spectra for MOF-508 and PMOF-508 calculated with the Raman-VASP implementation according to [45]. The data were broadened with a broadening parameter $\sigma = 0.5 \text{ cm}^{-1}$ according to eq. (5.2). Colouring scheme: red...oxygen, black...carbon, blue...nitrogen, white...hydrogen, grey...zinc

Compared to MOF-5, the metallic nodes are much simpler as they only consist of two zinc atoms. The linkers in x and y direction of the tetragonal unit cell are the same as for MOF-5 - i.e. terephthalic acid in the unreacted form (in the following abbreviated as PCB). The linker in z direction, however, is a 4,4'-bipyridine (in the following abbreviated as 44BP). A similar system that one can think of, is constructed by replacing the bipyridine with pyrazine - i.e. a heteroaromatic compound having two nitrogen atoms in opposite positions in a six-membered ring. Here this structure is referred to PMOF-508, where the P stands for pyrazine.

Although the two systems are very similar, there are some interesting differences observable in the Raman spectra. Firstly, the modes at about 160 cm^{-1} correspond to vibrations in the metallic nodes combined with rigid movement of the PCB linkers. Since all the involved parts are the same in both systems, the peak does not shift. Another interesting observation is that the mode at about 100 cm^{-1} in MOF-508 shows some kind of translational standing wave movement along the 44BP axis, where there is a node between the two pyridine rings. A similar mode can be found for PMOF-508 at about 160 cm^{-1} with the node of the wave being in the middle of the pyrazine (see fig. 5.3).

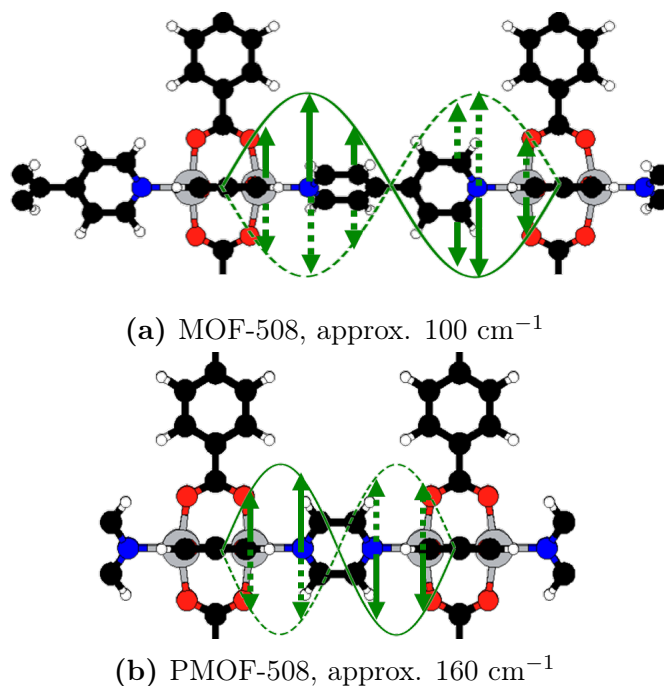


Fig. 5.3: Schematic displacement pattern for two similar oscillations (side view). The envelopes of the movements are only drawn between two neighbouring metallic nodes. Colouring scheme: red...oxygen, black...carbon, blue...nitrogen, white...hydrogen, grey...zinc

Seeing the vibrations, one is tempted to draw an analogy to a transversal standing wave. Since the "wavelength" of this vibration is shorter for PMOF-508, the frequency

has to be higher than for the respective mode in MOF-508, provided that the propagation speed of those transversal waves is approximately the same for both systems. Furthermore, the first peaks with the lowest wavenumbers for both systems are again torsional modes of the 44BP respectively the pyrazine linker. By using the same approximative procedure of how such modes should change (cf. eq. (5.3)) one obtains a not so good agreement as before. The frequency ratio from the moments of inertia should be $\sqrt{2} \approx 1.41$ whereas the direct division of the frequencies results in a value of about 1.6 by considering the peak at approximately 21 cm^{-1} of MOF-508 and the peak at about 13 cm^{-1} of PMOF-508. This can most probably be explained by the fact that here the (torsional) force constants are not the same. While the dihedral angle φ between the pyrazine ring and the PCB linkers is about 45° , both the pyridines of the 44BP in MOF-508 are closer to the PCBs, showing dihedral angles $\vartheta_{1/2}$ of around 28° . This implies that the torsional spring constants are stiffer in the case of MOF-508, thus this mode is shifted to a higher frequency.

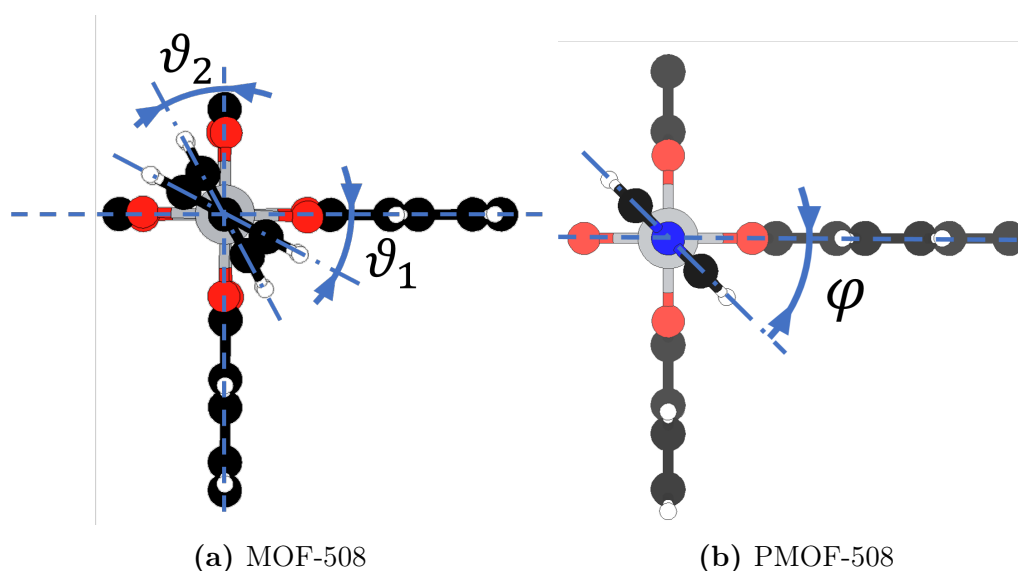
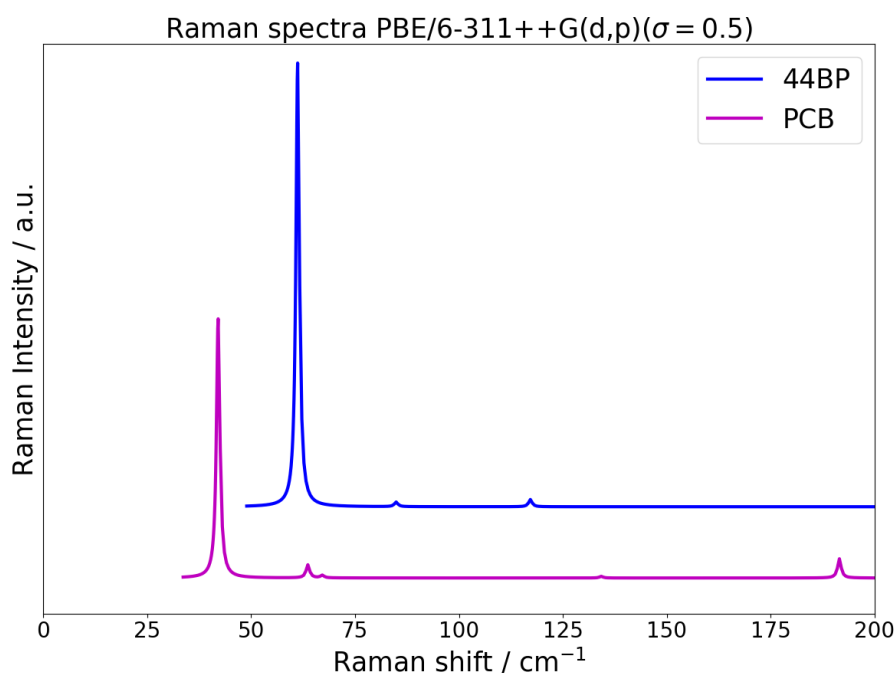


Fig. 5.4: Top view and dihedral angles of MOF-508 and PMOF-508. Colouring scheme: red...oxygen, black...carbon, blue...nitrogen, white...hydrogen, grey...zinc

A mode that is in nearly perfect agreement between both systems is the peak at about 34 cm^{-1} . This vibrational mode corresponds again to a torsional mode of the PCB linkers. Compared to MOF-5, where only this linker occurs in all three directions of space, the respective frequency is slightly decreased, suggesting that the torsional stiffness is larger for the metallic nodes of MOF-5. This makes sense if one remembers that the nodes of MOF-5 consist of very stable zinc-oxygen tetrahedra.



(a) Raman spectra for the linker molecules in MOF-508

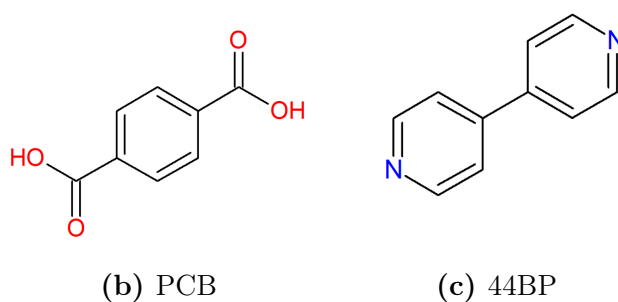


Fig. 5.5: Raman spectra of the linker molecules of MOF-508 calculated with Gaussian09 [59]. PCB...Terephthalic acid (para dicarboxybenzene), 44BP...4,4'-bipyridine. The data were broadened with a broadening parameter $\sigma = 0.5 \text{ cm}^{-1}$ according to eq. (5.2)

In order to see how the vibrational properties of the free linker molecules change when they are employed as the building blocks in a MOF, the two linkers of MOF-508 - 44BP and PCB, which happens to be the same linker as for MOF-5 - were also studied in terms of their Raman activities with Gaussian09 [59]. The Raman activities were calculated using a 6-311++G(d,p) basis set and the PBE functional after a geometry optimisation with the same functional and basis set. The conversion from activities to scattering intensities was carried out by using equation (5.1).

Interestingly, it seems that most of the low-frequency intramolecular modes of the isolated molecules are suppressed respectively turned into different modes once the

5. Results and discussion

molecules are attached to the heavy metallic nodes. Only very few vibrations "survive" the synthesis to a MOF. The first Raman scattering peak in figure 5.5 of PCB (terephthalic acid, para dicarboxybenzene) is a vibration where both carboxyl groups twist in different directions with respect to the plane of the central phenyl ring (antisymmetric torsion). When the molecule is fixed to the metallic nodes at both sides, however, this would only be possible if the phenyl ring changes its geometry to a non-planar configuration and performs separate oscillations in the left and the right side of the ring. This antisymmetric torsional mode does not appear if the molecule's movement is constrained by the metallic nodes. The symmetric torsional mode, however, that also occurs in the respective MOFs can be found at about 68 cm^{-1} which is significantly higher in frequency than the torsional modes in all the MOFs. Most probably one reason for that is that PCB has a planar configuration when used as a linker in MOFs, but is not planar as free molecule. In this mode it seems that the central phenyl ring performs a torsional oscillation inside a smaller dihedral angle range limited by those of the carboxyl groups. This would mean that the COOH groups exert an additional force on the phenyl ring, which results in an increased frequency, as it is observed by comparing the results. Furthermore, in the case of vibrations of the MOF constituents, the oscillations are supposed to have a higher "effective mass". This increased amount of inertia is expected to decrease the frequency additionally.

In contrast to PCB, some Raman active vibrations of the 44BP linker survive nearly unharmed. The distinct peak in the Raman scattering spectrum of MOF-508 at about 68 cm^{-1} corresponds to an oscillation where the dihedral angle between the pyridine rings of the 44BP linker periodically changes with time - i.e. the two pyridine rings twist with a phase shift of π against each other (antisymmetric torsion). Exactly the same vibration can also be found in the free molecule at approximately 63 cm^{-1} . In this case the dihedral angle between the pyridine rings in the free molecule is nearly the same as for the linker in MOF-508 (approx. 36°). Since the relevant geometric features seem to be mostly unaltered for this vibrational mode, it is not surprising that also the frequency stays nearly unaffected.

On the other hand, also certain modes can be distinguished, which are localised in the linkers of the MOFs, but do not show up in the Raman spectra of the free molecules. The very first peak of MOF-508 in figure 5.2 corresponds to a torsional mode of the 44BP linker as it was discussed earlier. This mode, however, is a rigid movement of the whole molecule - i.e. the two pyridine rings perform torsional in-phase movement (symmetric torsion) - that means that for the free molecule usually a frequency of 0 is assigned to this mode respectively it is not seen as a vibrational mode at all.

In spite of the fact that simulations of that kind are a convenient method to compare the results to experiments and that many vibrational properties can be learnt from the analysis of the Raman spectra, they only provide insight in the phonon modes at the Γ point. For the thermal conductivity, the phonon band structure has to be known, though. The large system sizes necessary to achieve that are often too expensive within DFT approaches. However, Raman spectra calculations and the analysis of the occurring modes are expected to have a high potential for structure investigation of MOFs. This could be feasible, once one has understood the geometric dependencies and con-

straints of certain modes. From that, one could predict, how the respective vibrations would change if the external conditions (pressure, different substrates, defects etc.) were altered and use the spectra to determine the configuration and constitution of the MOF crystal.

5.2. Comparison of the phonons obtained with DFTB+ and VASP

Since for certain systems supercells containing up to nearly 9000 atoms are required to take into consideration for the phonon calculations, it is absolutely necessary to find another numerical approach to the problem of calculating the phonons. The chosen method is DFTB. In order to justify the transition from the more accurate DFT method to DFTB, one has to make sure that at least the general tendencies of observable results remain the same. This means that a benchmark concerning the phonon frequencies obtained with the DFT-based code VASP and the DFTB-based package DFTB+ is necessary. Note that all the computational settings like energy cutoffs, self-consistency accuracy, etc. for both codes used here are the same as discussed in section 4.

Obviously, the whole band structure cannot be compared because with VASP the calculation of the essential supercells is limited by the available resources. Therefore, the next convincing quantity, which is more accessible with both approaches, was chosen as the subject of the benchmark: the phonon frequencies at Γ . For reasons of comparability, the equilibrium lattice constants found with both codes for MOF-5(Zn) and IRMOF-3(Zn), whose Γ -phonons will be used for the benchmark, are listed in table 5.2. The reported lattice parameter is the variable a of the following matrix of lattice vectors.

$$P = \begin{pmatrix} 0 & a & a \\ a & 0 & a \\ a & a & 0 \end{pmatrix} \quad (5.4)$$

By choosing a matrix like that, which contains the primitive lattice vectors of the face-centred cubic Bravais lattice as the rows, a corresponds to half the edge length of the cubes in the conventional unit cell.

Tab. 5.2: Equilibrium lattice constants a for two exemplaric systems calculated with VASP and DFTB+.

system	$a / \text{\AA}$	
	DFTB+	VASP
MOF-5(Zn)	13.19	13.03
IRMOF-3(Zn)	13.20	13.06

The comparison of the lattice constants obtained with DFTB+ with the results of VASP shows that DFTB+ tends to yield increased values of 0.16 \AA resp. 0.14 \AA . In both cases, the relative change is approximately 1 %.

5. Results and discussion

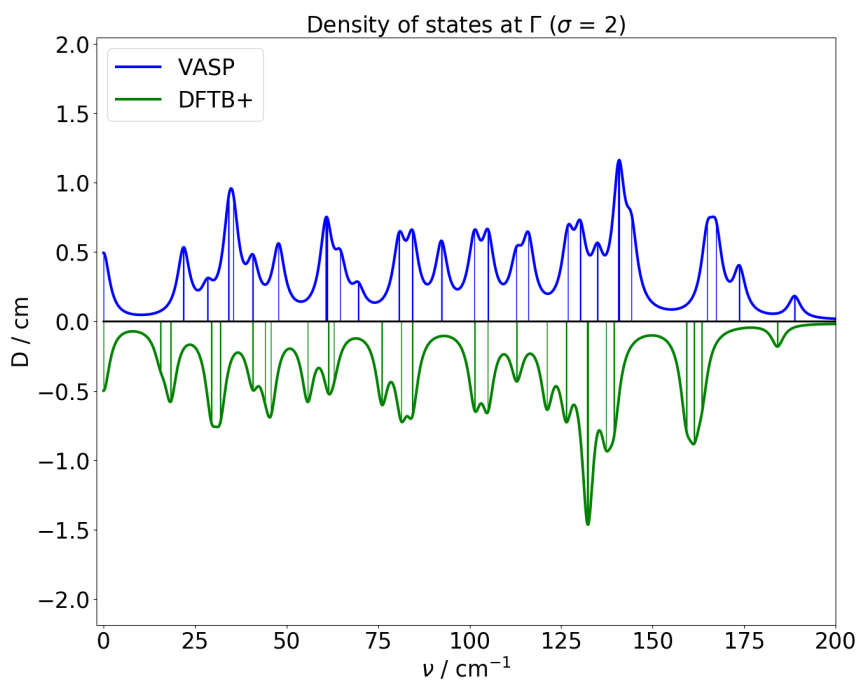
DFTB+ obviously seems to yield reasonable results concerning the geometry of the systems compared to VASP. One has to keep in mind, however, that even this small deviations will slightly alter the obtained phonon frequencies in a sense that typically the frequencies are shifted to higher values for a smaller cell volume. This can be observed in the Γ -DOS in figure 5.6. Some features that can be seen in the VASP results are slightly shifted to lower frequencies for DFTB+ partly because of the increased lattice constants. In figure 5.6 you can see the Γ -phonons of MOF-5(Zn) and IRMOF-3(Zn) once obtained with VASP and once with DFTB+. Since the frequencies are not supposed to be in one-to-one agreement between the two codes, a broadening of the modes with Lorentzians according to equation (5.2) was done. In that way, the general trends and distinct features can be compared in a more reasonable way.

The comparison reveals that both curves for the Γ -DOS show a similar behaviour for both systems. Sometimes, frequencies are slightly shifted resulting in minor changes of the envelope curves. For MOF-5 the agreement between DFTB+ and VASP seems to be better than for IRMOF-3. For the latter, the relatively small region between about 130 cm^{-1} and 140 cm^{-1} differs noticeably. But still, considering the big conceptual difference between DFT and DFTB the agreement is rather satisfactory. These results show that DFTB+ has proven to be quite well applicable for calculating vibrational properties if one is more interested in the general physical behaviour of the system rather than tight accuracy of the results.

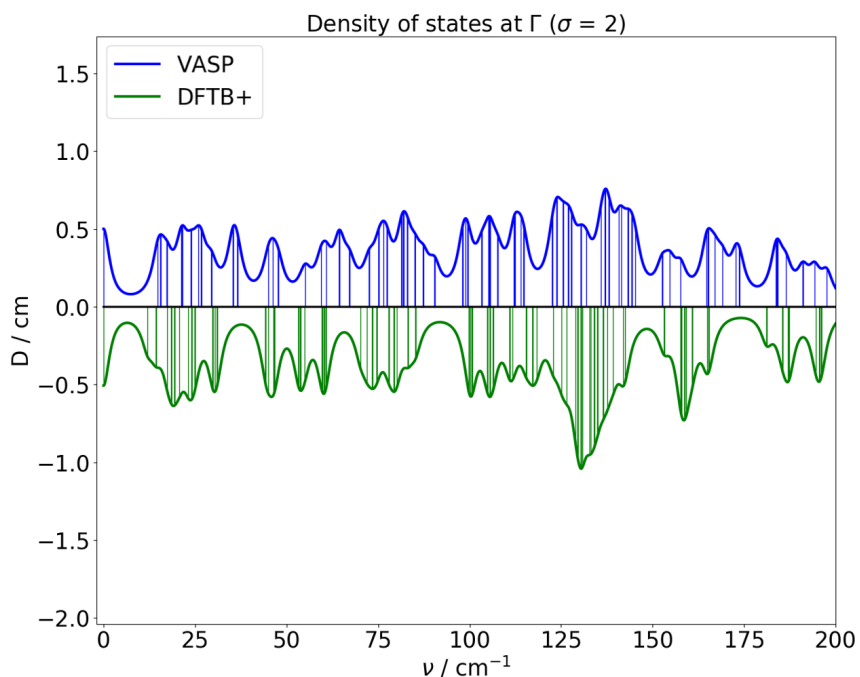
A further way to estimate the reproducibility of relevant quantities calculated with DFTB+ is to consider the phonon eigenvectors. The eigenvectors are orthonormal for one system and determine which atoms move with which amplitude in which directions for a given phonon frequency. That means that vibrations with the same physical origin and the same symmetry should have the same eigenvector. Therefore, the eigenvectors obtained with DFTB+ are compared with those of VASP. A convenient way to do this is to calculate the dot product between the vectors having $3N$ components each, where N is the number of atoms in the unit cell. Because the i^{th} eigenvector of VASP does not necessarily have to correspond to the i^{th} eigenvector of DFTB+, the following procedure was employed to identify the pair of eigenvectors that most probably have the most in common. For every eigenvector of VASP, the dot products with all the eigenvectors obtained with DFTB+ were calculated. The vector with the biggest overlap was then regarded as the corresponding eigenvector.

In figure 5.7 histograms of the overlap distributions for both compared systems are displayed. Note that the results of VASP and DFTB+ are in better agreement if only a restricted frequency region (up to 200 cm^{-1}) is considered. Especially, the carbon-hydrogen stretching vibrations are not very well described with DFTB+ resulting in disagreements in high-frequency regions. Despite this shortcoming, this is not seen as an obstacle for the computation of the thermal conductivity, since only the phonon modes with very low frequencies will be the main contributors to heat transport.

In short, DFTB+ has been shown to yield plausible results for the general trends of the physical quantities, which are in the focus of the current work. Therefore, the use of DFTB+ is justified for further calculations of the thermal conductivity in MOFs. The latter will be the topic of the next section.



(a) MOF-5(Zn)



(b) IRMOF-3(Zn)

Fig. 5.6: Phonon frequencies (ν) at the Brillouin zone center Γ calculated with VASP and DFTB+ for (a) MOF-5(Zn) and (b) IRMOF-3(Zn). The frequency spectra was broadened with a Lorentzian according to eq. (5.2) with a broadening parameter $\sigma = 2 \text{ cm}^{-1}$ to obtain a density D at Γ .

5. Results and discussion

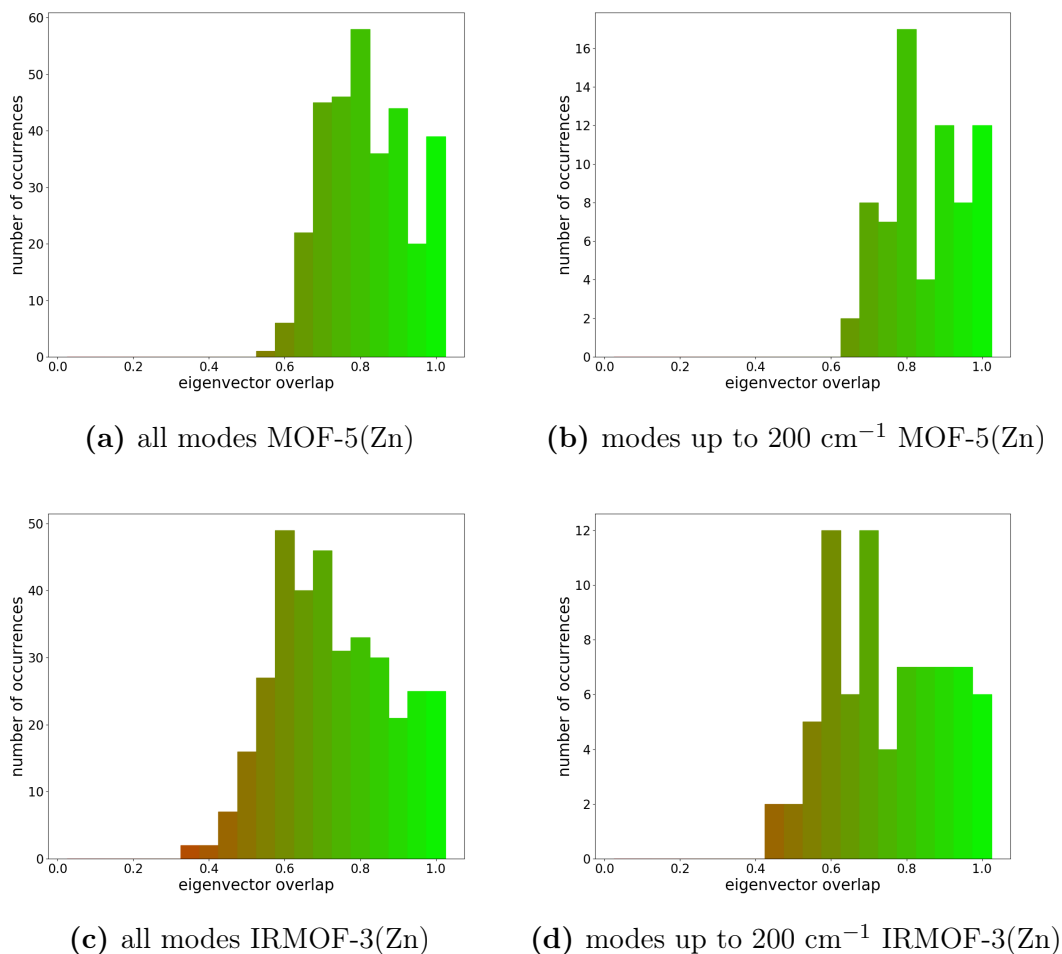


Fig. 5.7: Histograms of the dot product between phonon eigenvectors of (a),(b) MOF-5(Zn) and (c),(d) IRMOF-3(Zn) calculated with VASP and the eigenvectors calculated with DFTB+. In (a) and (c) all modes are considered, in (b) and (d) only low-frequency modes with a frequency up to 200 cm^{-1} are taken into account.

5.3. Thermal conductivity

By using the more affordable DFTB approach, one can obtain the desired phonon band structures, which are essential to know for the computation of the thermal conductivities. From the band structure, one is able to compute the harmonic ingredients of the thermal conductivity: the group velocities, the heat capacities and the phonon DOS. Although the computational effort to obtain those is relatively high, the anharmonicities are even more challenging to consider properly. In this study the model of Bjerg et al. is then used to obtain the phonon lifetimes from the mode Grüneisen parameters. The results as well as a detailed analysis are presented in the following section.

5.3.1. Brillouin zone sampling

In principle, all the necessary ingredients for calculating the thermal conductivity have been discussed already. However, there is a last technical issue that is crucial to think about before reporting any results. The general expression for the thermal conductivity (cf. eq.(3.9)) includes an integral over the first Brillouin zone. Of course, this integral has to be approximated as a sum over discrete \mathbf{q} points. As a consequence, the thermal conductivity tensor is approximated by the following double sum.

$$\kappa_{ij} \approx \frac{1}{V} \sum_n \sum_{\mathbf{q}} \tau_{n,\mathbf{q}} C(\omega_{n,\mathbf{q}}) v_{g,n,\mathbf{q},i} v_{g,n,\mathbf{q},j} \quad (5.5)$$

With the transition from the continuous integral to the discrete sum another problem arises. How many \mathbf{q} points should one choose? Which sampling density of the first Brillouin zone is necessary to see convergence of the sum formulation towards the integral expression?

The answer to this question is rather unsatisfying. It turns out that it depends on the system. Therefore, one has to investigate the convergence behaviour of every system separately. Since one could not even be sure if exactly the same convergence speed with respect to the \mathbf{q} mesh density for different temperatures will be observed, every temperature for each system is tested.

Essentially, one can think of two approaches to compute the thermal conductivity for a infinitely dense mesh. Either, one can simply increase the number of \mathbf{q} points in the first Brillouin zone further and further until there are no significant changes anymore. The downside of this approach is that it could become quite time consuming to calculate the phonons, group velocities and the Grüneisen parameters for highly dense meshes⁵. Alternatively, one can fit different functions to the dependence of the thermal conductivity on the mesh and extract the "saturation value" from those fits. This approach was considered to be the more reasonable one.

The drawback of this approach is, however, that one has to think about possible fit functions (models). It was found that the following functions usually reproduce the convergence trends best.

$$f_1(n_q | \kappa_\infty, n_q, N, \Delta N) = \kappa_\infty \left(1 - \exp \left\{ -\frac{n_q - \Delta N}{N} \right\} \right) \quad (5.6)$$

$$f_2(n_q | \kappa_\infty, n_q, N, \Delta N) = \kappa_\infty \left(\tanh \left\{ \frac{n_q - \Delta N}{N} \right\} + 1 \right) \quad (5.7)$$

The fit functions f_1 and f_2 both have κ_∞ as the limit for $n_q \rightarrow \infty$ for $n_q \times n_q \times n_q$ meshes. The parameters ΔN respectively N describe the offset respectively the convergence "speed". In order to find out which of the proposed models fits best, Bayesian model comparison is employed, assuming additive Gaussian noise of unknown standard deviation on the data. In all the reported cases the model according to equation (5.6)

⁵Especially because the `MESH_SYMMETRY = .FALSE.` option has to be used.

clearly outperforms the model according to (5.7). Furthermore, by using a Bayes approach one can extract uncertainties and even full probability density functions for the fit parameters.

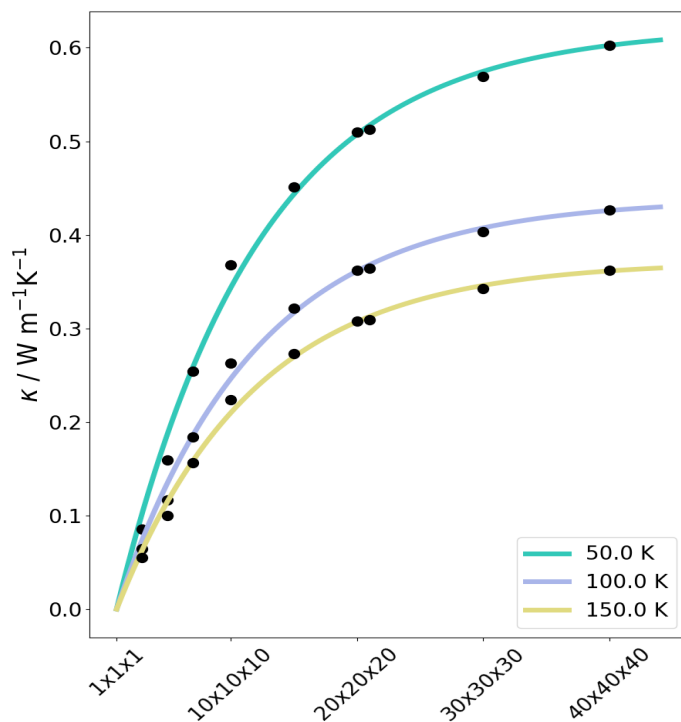


Fig. 5.8: Thermal conductivity (κ) over different \mathbf{q} point meshes for three temperatures of MOF-5(Mg).

In figure 5.8 one can see the comparison of the discrete data points that were obtained with different \mathbf{q} point meshes and the fits of model 1 according to equation (5.6). The shown data were calculated for MOF-5(Mg) at some selected temperatures. Doubtlessly, the behaviour is well described with the respective convergence model.

It must be mentioned that for sampling the \mathbf{q} points one has the opportunity to calculate the desired quantities only for an irreducible set of (properly weighed) wave vectors, which result from symmetry considerations of the system, or for the whole first Brillouin zone. For scalar quantities like energies, frequencies or the mode Grüneisen parameters it suffices to consider only the irreducible part, whereas for vector quantities like the group velocities one has to take the whole Brillouin zone into account or apply symmetry transformations afterwards. Therefore, the calculations of the Grüneisen parameters were conducted for the irreducible set of \mathbf{q} points considering their weights, while the group velocities were obtained by \mathbf{q} point sampling of the whole first Brillouin zone. With phonopy this can be done by setting the tag `MESH_SYMMETRY` to `.FALSE.` so that no symmetries are considered.

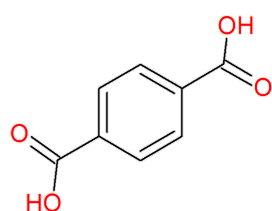
To sum up, the finally reported thermal conductivities seen in figure 5.11 and 5.21 as a function of temperature are the expectation values $\langle \kappa_\infty \rangle$ of the respective probability

distributions separately computed for each shown temperature and system with the convergence model according to equation (5.6). With that final step we are in the position to report and discuss the thermal conductivities for several MOFs, where the constituents are varied systematically.

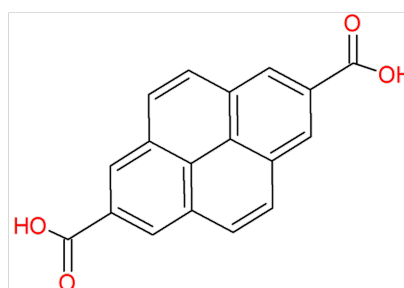
5.3.2. Influence of the organic linkers

First, the influence of different organic linkers will be discussed. In order to obtain some kind of structure-to-property relationship concerning the thermal conductivity, several systems were investigated. Based on MOF-5(Mg) the linkers were changed to other linkers showing similarly high degrees of symmetry. What is meant by this is that for IRMOF-3, for instance, there are much fewer symmetry operations due to the additional amino group as it was illustrated in section 5.1. The clear advantage of systems with more symmetries is that one can significantly reduce the number of displacements necessary to calculate the force constants. Making use of symmetries one, therefore, can map the interatomic interactions onto symmetry-equivalent atoms.

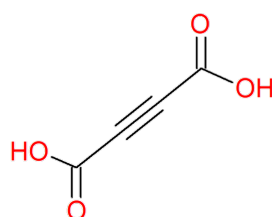
The chosen systems are rather simple so that the analysis steps can yield physically meaningful results. The systems of interest are depicted in figure 5.10. For a better understanding of the chemical differences of the linkers, the respective molecules are shown in their unreacted form in figure 5.9.



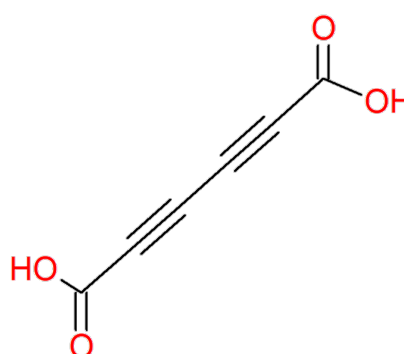
(a) linker in MOF-5



(b) linker in IRMOF-14



(c) linker in IRMOF-131



(d) linker in IRMOF-132

Fig. 5.9: Structural formulae of the unreacted linker molecules used in the studied IRMOFs.

5. Results and discussion

Note that all four systems have magnesium as the metal components in the nodes. In spite of the fact that their zinc containing equivalents are said to be synthesised more easily, magnesium is less challenging to treat in the calculations because the d-orbitals do not have to be considered. For the sake of understanding the influence of the linkers separated from that of the nodes, it was decided to study the variation of the organic constituents with the easiest and cheapest systems first. Since obviously all of the systems discussed here have the same metallic node, the indicator of the metal in the MOFs name will be omitted in the following.

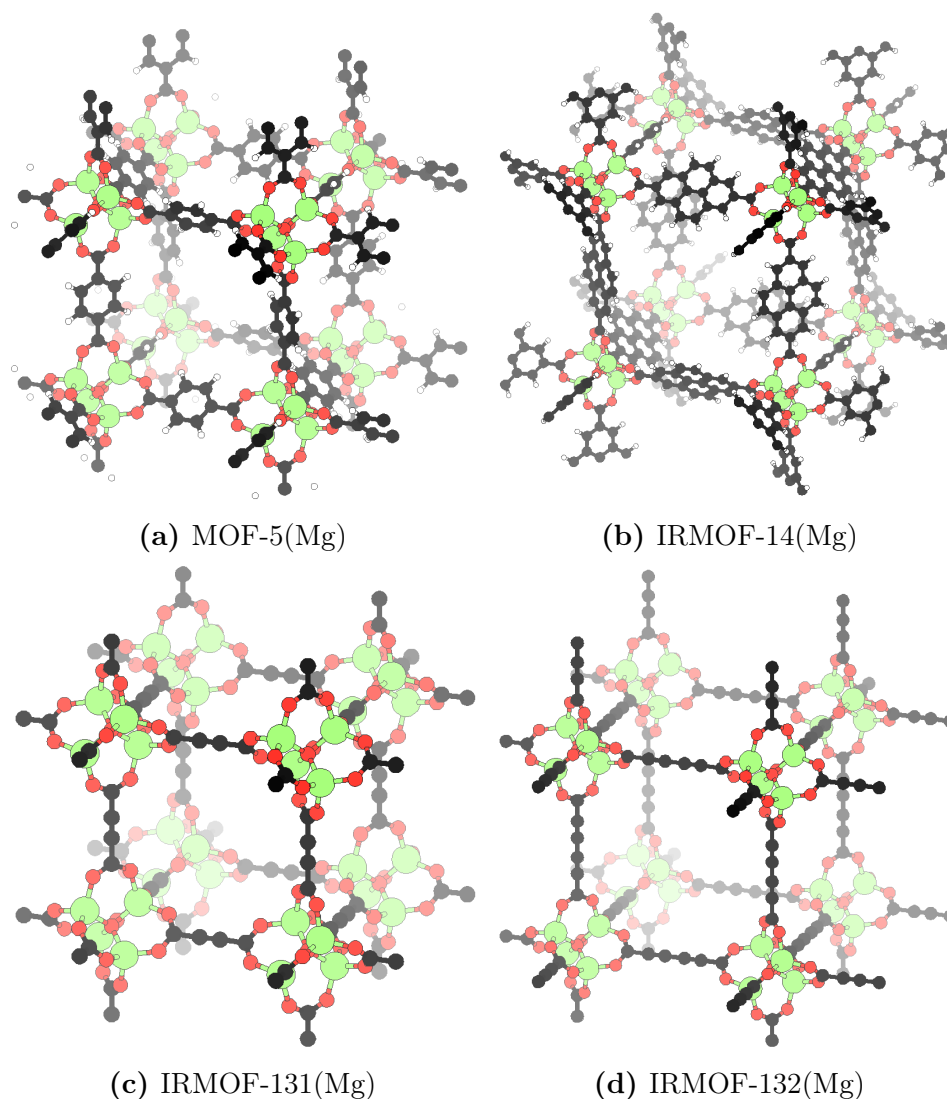


Fig. 5.10: Three-dimensional views of MOFs which differ only in the organic linkers, but not in the metallic nodes. The influences of the linkers on the thermal conductivity is discussed based on those four systems. Colouring scheme: red...oxygen, green...magnesium, black...carbon, white...hydrogen

Two of the systems, MOF-5 and IRMOF-14, have aromatic linkers. It should be emphasised that IRMOF-14 is the non-interpenetrated variant of this MOF. Due to the large free volume in the cavity of larger MOFs, there is usually another structure possible, where two frameworks interpenetrate each other. This is especially common for IRMOFs because the regular lattice can be maintained due to the cubic symmetry. For the case of the pyrene-containing linker of IRMOF-14 there is also an interpenetrated version that is usually referred to as IRMOF-13 which is not the subject of the present study.

The other two systems, IRMOF-131 and IRMOF-132, have alkynes as linkers. In the case of IRMOF-131 but-2-yne was attached to the oxygens of the linkers. Since the four carbons in the linear chain of this molecule form a single, a triple and another single bond (1-3-1), the isorecticular MOF was labelled with the number 131 as another systematic name could not be found in literature. IRMOF-132 contains hexa-2,4-diyne in its linkers, which was simply numbered with 132 as the structural successor of IRMOF-131. These systems are interesting for some reasons. Firstly, they contain fewer atoms and are seemingly easier to calculate. Secondly, the torsional movement of the organic linkers is completely suppressed for those alkyne systems as the linkers are totally rotationally symmetric. Moreover, there are no hydrogen atoms in the unit cell for which the (stretching) oscillations are not so well described with DFTB+. Another advantage of that type of linker is that one can study the effect of cell lengths on the thermal conductivity of MOFs. Although the cell of IRMOF-14 is also larger than that of MOF-5, the linker of IRMOF-14 introduces ten carbon and four additional hydrogen atoms along each edge of the cubic cell. As a consequence, the calculations are more expensive and the analysis is more challenging. By using alkyne linkers, like in IRMOF-131 and IRMOF-132, the distance of the metallic nodes can be increased without adding too many further atoms.

Since all systems in figure 5.10 have an fcc Bravais lattice, it follows from symmetry that all rank 2 tensors that describe materials properties are diagonal with the same value for all three entries. For that reason, whenever the thermal conductivity κ is plotted or mentioned, it is actually one of this components $\kappa_{xx} = \kappa_{yy} = \kappa_{zz} = \kappa$. In other words, the thermal conductivity formally reduces to a scalar so that the heat flux density is always aligned with the temperature gradient.

In figure 5.11 one can find the temperature dependent thermal conductivities for the mentioned systems. As can be seen from the graphs, MOF-5 shows much better thermal transport properties than all the other systems. Another interesting feature is that the temperature dependence of the thermal conductivity seems to be much weaker in the case of IRMOF-14 compared to the other systems. According to the results, the thermal transport will be more pronounced in IRMOF-132 at temperatures below 200 K compared to IRMOF-14. The situation changes, however, for $T > 200$ K, where the thermal conductivity decreases faster with the temperature than for IRMOF-14.

In order to understand the main influences, one has to decompose the results for κ into its ingredients. For the sake of simplicity, the following analysis will be conducted only for one fixed temperature of $T = 300$ K. The choice of temperature changes the thermal conductivity, the heat capacities and the phonon lifetimes, whereas the group velocities

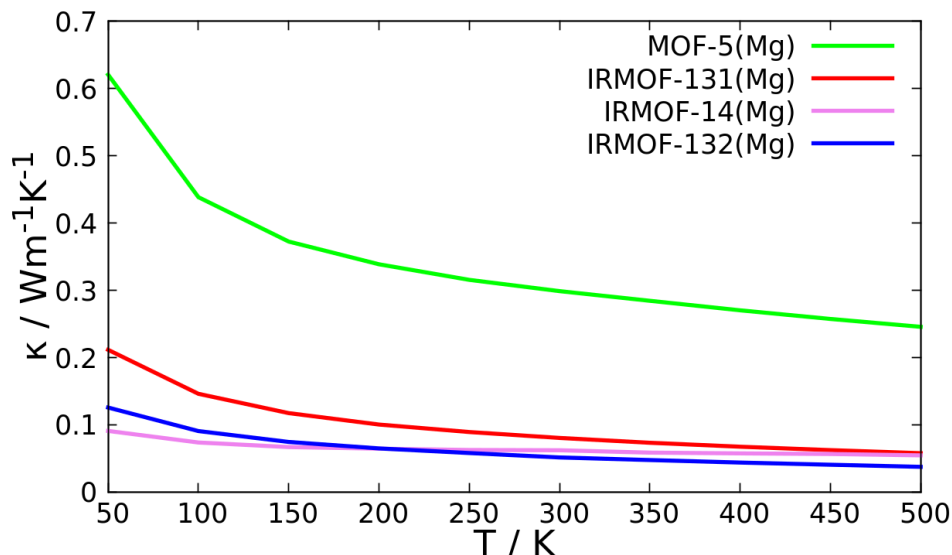


Fig. 5.11: Calculated thermal conductivity (κ) as a function of temperature (T) of some IRMOFs with different organic linkers.

stay unaltered⁶. The first step is to highlight the modes in the phonon band structure that contribute most to the thermal conductivity. Such band structure plots can be seen in figure 5.12 and 5.13. As equation (3.9) states, modes with the higher group velocities will contribute more effectively. This can be clearly seen in the band structures. Another observation is that the biggest contributions are centred around the Γ point. Since these modes usually have large group velocities and also long lifetimes, this is not surprising. Noticeably, MOF-5 shows a large degree of dispersion - i.e. many bands with non-vanishing slopes - also away from the Γ point, whereas for the other systems (especially IRMOF-14) only few contributions from \mathbf{q} points farther away from the Brillouin zone centre play a role. Possibly this is already the key to the high thermal conductivity in case of MOF-5.

In order to verify this assessment a bit more quantitatively, one can convert the integral over \mathbf{q} points in equation (3.9) to an integral over frequencies using the density of states ($\text{DOS}(\nu)$).

$$\kappa_{xx} = \int d\nu \tau(\nu) C(\nu) v_{g,x}^2(\nu) \text{DOS}(\nu) = \int d\nu \kappa_{xx}(\nu) \text{DOS}(\nu) \quad (5.8)$$

One can, therefore, calculate the product of the phonon density of states and the mode contribution per frequency ($\kappa_{xx}(\nu)$) to the thermal conductivity to find out, which phonon frequencies are the most important ones. Further relevant quantities to analyse are the squared group velocities $v_{g,x}^2(\nu)$, the heat capacities $C(\nu)$, and the phonon lifetimes $\tau(\nu)$ as well as the products of those with the DOS: $v_{g,x}^2(\nu) \cdot \text{DOS}(\nu)$, $C(\nu) \cdot \text{DOS}(\nu)$,

⁶If one neglects the influence of thermal expansion of the unit cell, which would have an influence on the band structure determined by the Grüneisen parameters.

and $\tau(\nu) \cdot \text{DOS}(\nu)$. For the DOS, a broadening with the same width as for the Raman spectra was used ($\sigma = 0.5 \text{ cm}^{-1}$).

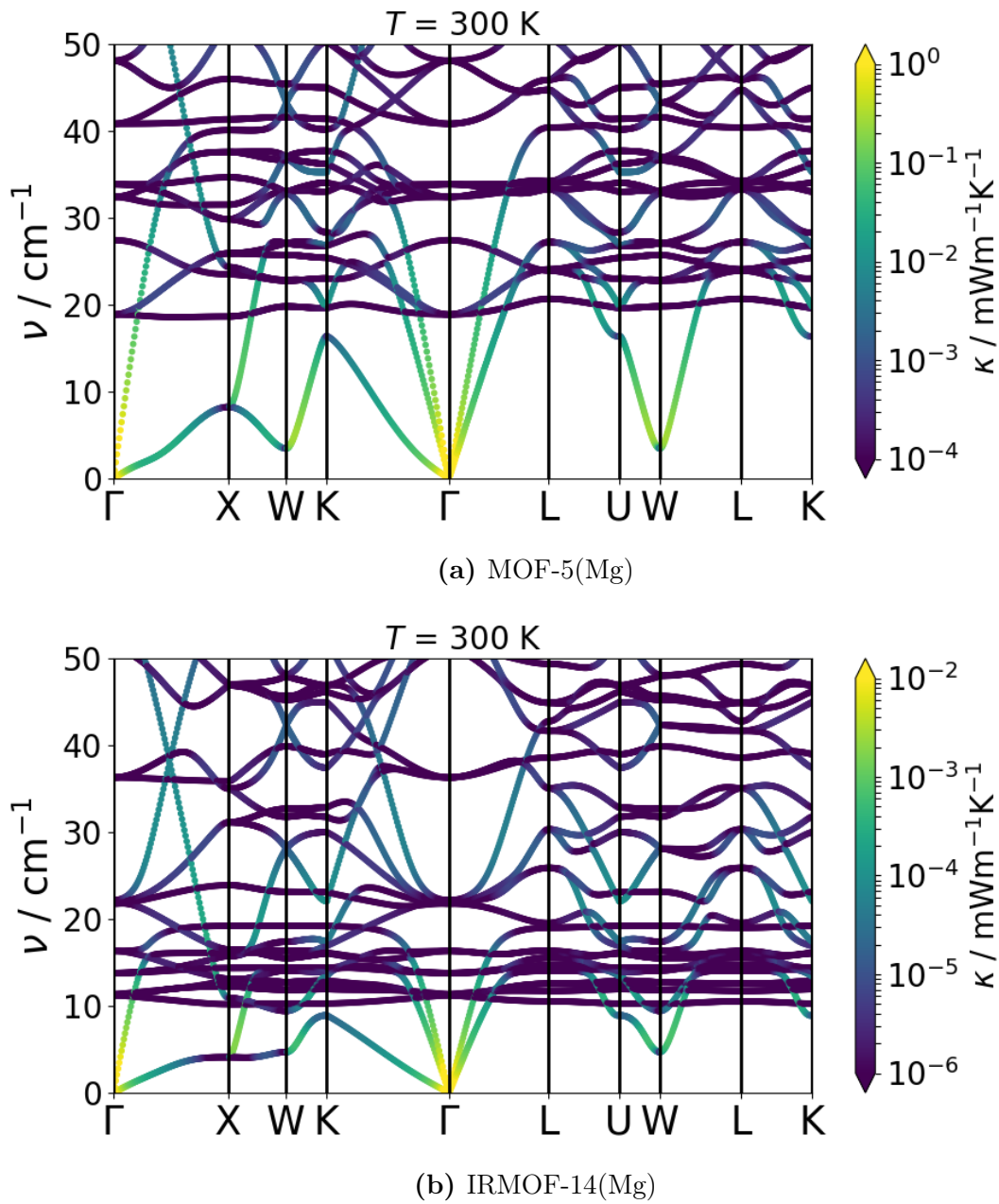


Fig. 5.12: Phonon band structure of the studied systems with aromatic linkers. All the systems have a face-centred cubic Bravais lattice. The bands are coloured in a logarithmic scale showing the contribution to the thermal conductivity κ per \mathbf{q} point and mode.

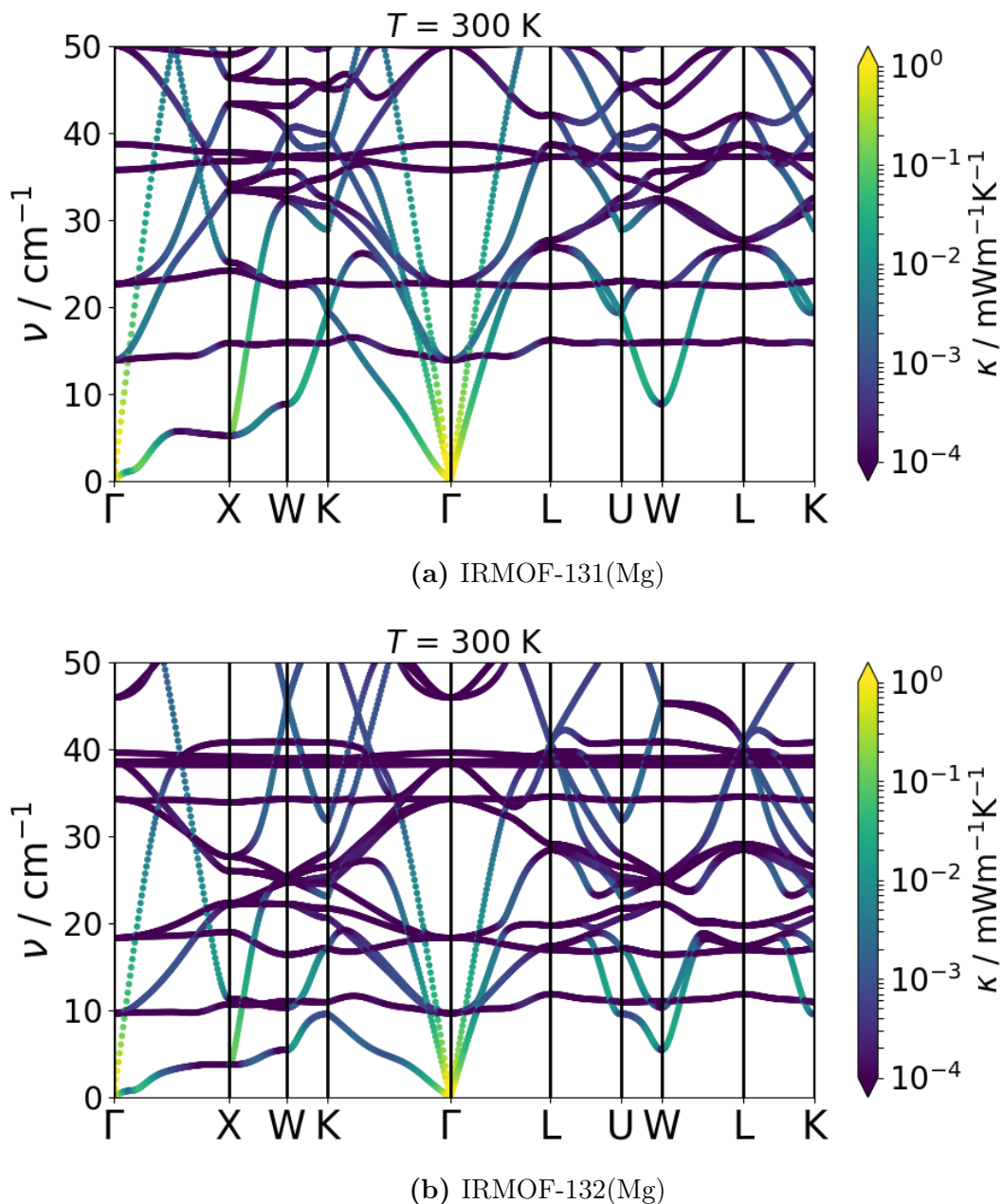
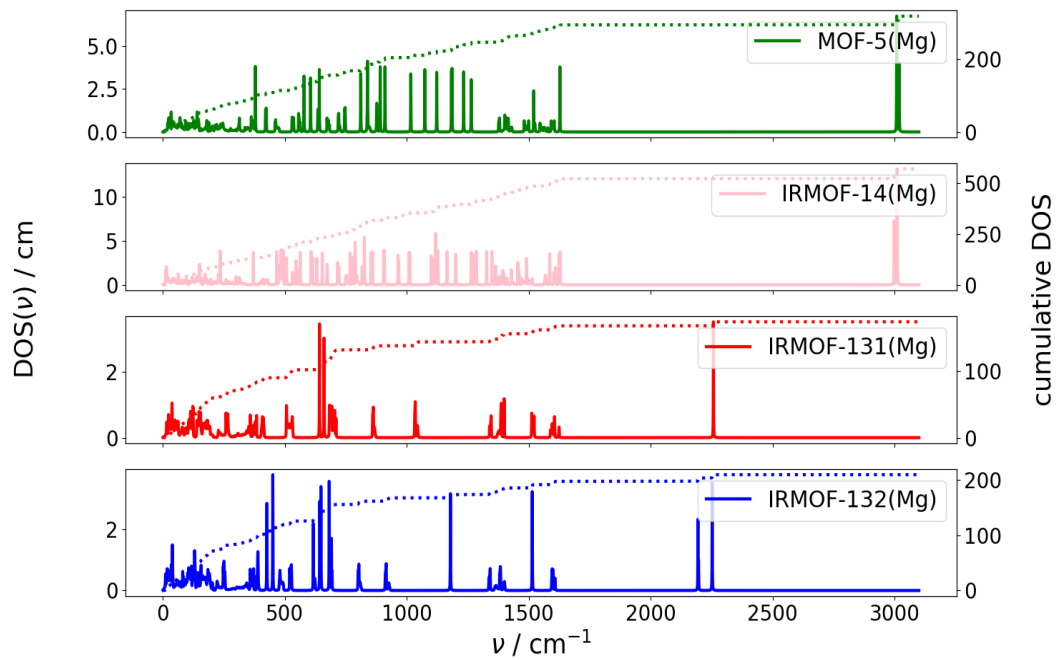
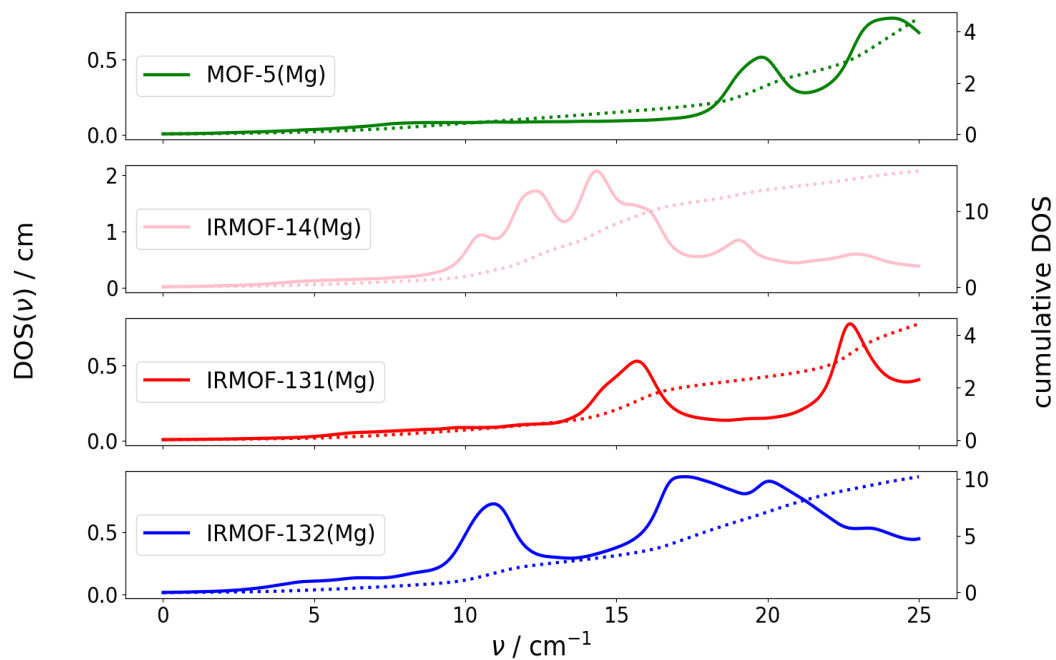


Fig. 5.13: Phonon band structure of some of the studied systems with alkyne linkers. All the systems have a face-centred cubic Bravais lattice. The bands are coloured in a logarithmic scale showing the contribution to the thermal conductivity κ per \mathbf{q} point and mode.

Since the phonon DOS is included in the products discussed before, it is useful to consider the DOS alone, at first. The DOS for the four studied IRMOFs can be seen in figure 5.14. Note that the integrated density of states (normalised with $3N$) is plotted on the secondary ordinate. Additionally, the low-frequency region is shown explicitly..



(a) Full range



(b) Zoomed in range

Fig. 5.14: Density of states (DOS) of selected IRMOFs with different organic linkers in (a) full and (b) the low-frequency (ν) range. The cumulative integrals are plotted as dotted lines on the secondary ordinates.

5. Results and discussion

For all the investigated systems, the DOS is usually characterised by rather sharp peaks instead of the comparably smooth behaviour known from typical inorganic crystals. Since the DOS was calculated for at least $40 \times 40 \times 40$ \mathbf{q} point meshes, this fact cannot result from too coarse sampling in reciprocal space, but rather from the band structure, which shows only little dispersion.

The first quantity to analyse is the integrand of the last equality in equation (5.8), which can be seen in figure 5.16. The solid lines are the mode contributions κ_{xx} multiplied with the DOS, whereas the dotted lines are the cumulative integrals, which converge to the total thermal conductivity. From the full range plot over all occurring frequencies in figure 5.16 one can find that basically every contribution to the thermal conductivity has its origin in a phonon mode with a frequency below 25 cm^{-1} . However, for MOF-5 all the contributions per frequency are significantly higher than for all the other systems, which finally results in the higher total thermal conductivity. One obvious difference between the analysis results for IRMOF-14 and IRMOF-131 is that the relevant contributions decay faster with the frequency for IRMOF-14. Although the product of the DOS and the mode contributions to the thermal conductivity are the relevant quantity for the integral in equation (5.8), it can be misleading to analyse this product, since peaks can have their origin in either a high DOS or a high $\kappa_{xx}(\nu)$. Therefore, the mode contributions without multiplication with the DOS can be found in figure 5.15.

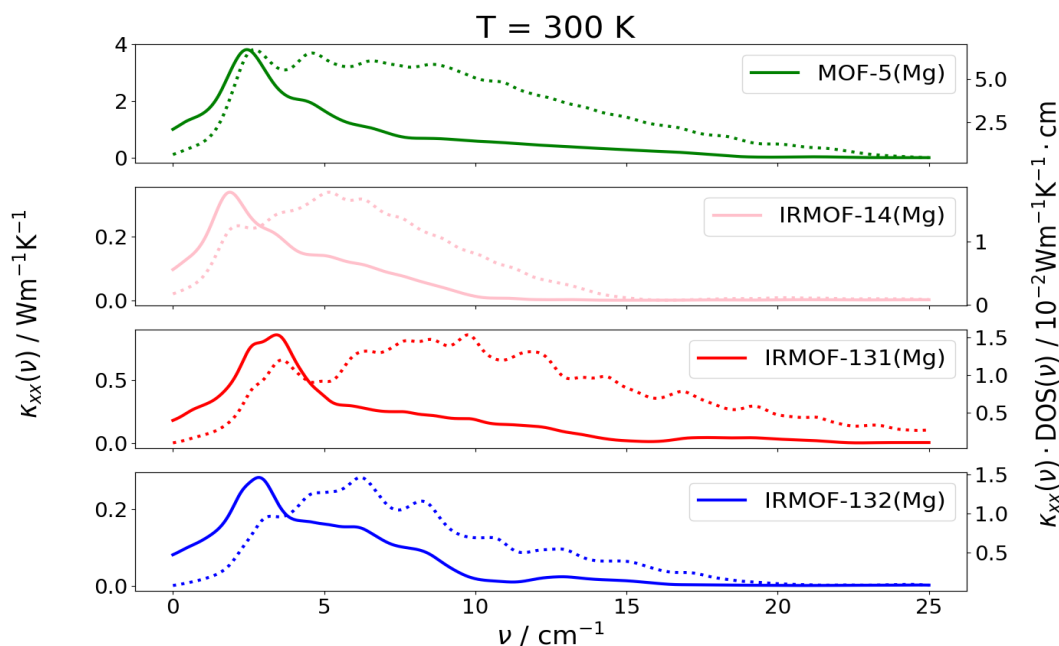


Fig. 5.15: Mode contributions to the thermal conductivity (κ_{xx}) (solid lines, left ordinate) and their products with the density of states (DOS) (dotted lines, right ordinate) of selected IRMOFs with different organic linkers in low-frequency (ν) range at 300 K.

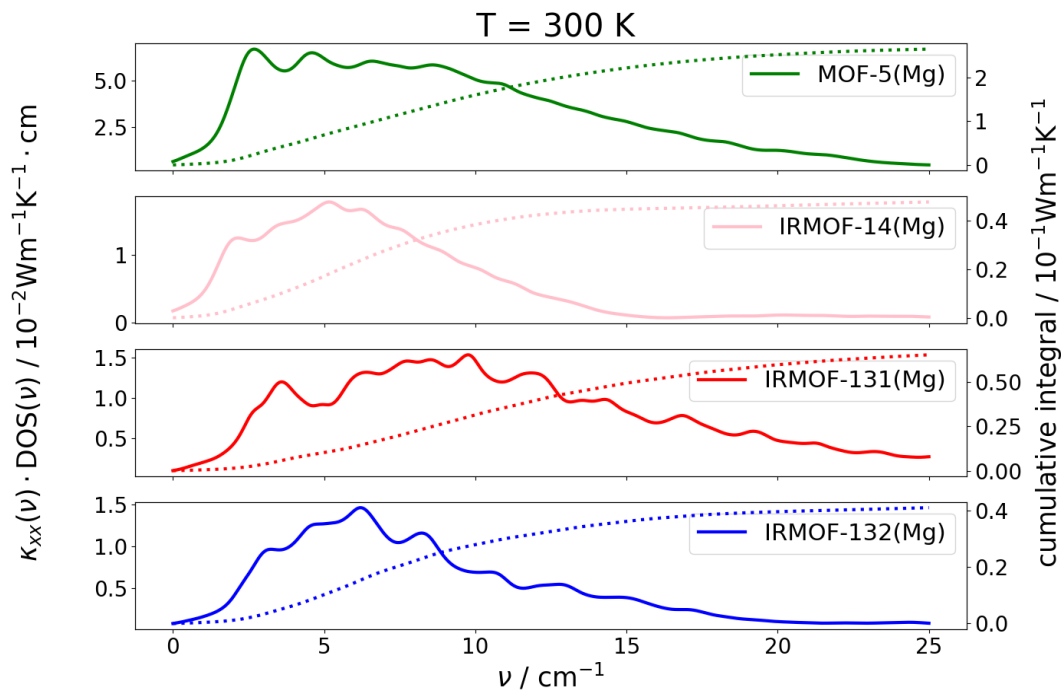
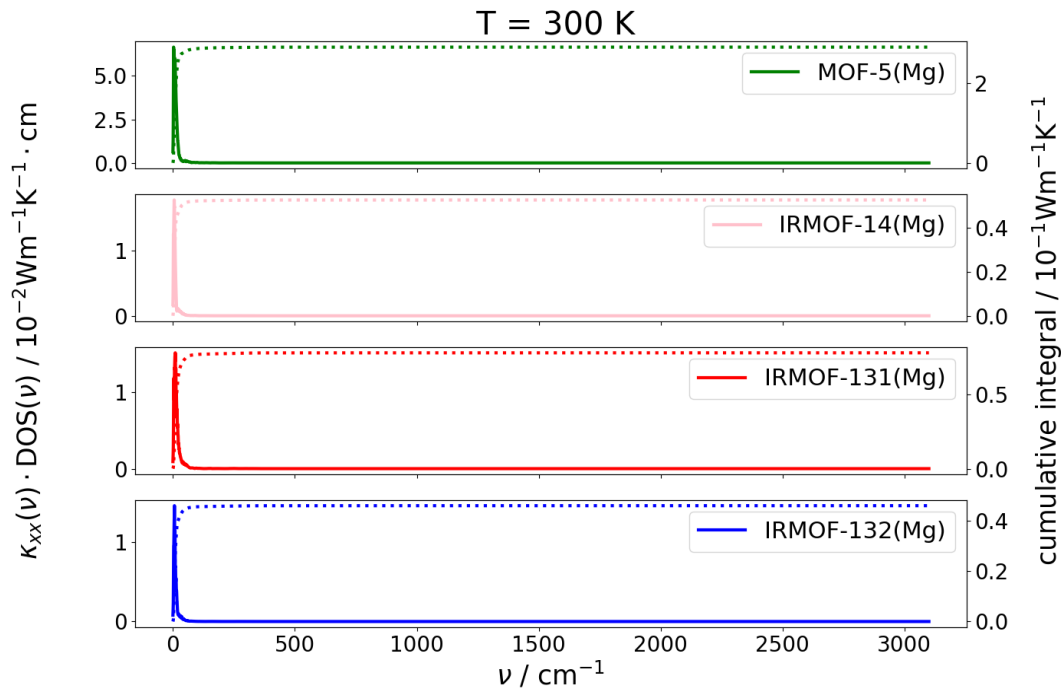


Fig. 5.16: Mode contributions to the thermal conductivity (κ) multiplied with the density of states (DOS) of selected IRMOFs with different organic linkers in (a) full and (b) the low-frequency (ν) range at 300 K. The cumulative integrals are plotted as dotted lines on the secondary ordinates.

5. Results and discussion

It can be seen in figure 5.15 that the high contributions at frequencies above 5 cm^{-1} rather result from the gradually increasing DOS, since the mode contributions $\kappa_{xx}(\nu)$ decay more quickly.

With this kind of analysis one can deduce some interesting qualitative relations, but for a more quantitative statement, what limits the thermal conductivity to that relatively small frequency region, and why the mode contributions for certain systems outweigh those of others, one has to analyse all the ingredients of the thermal conductivity according to equation (3.9) respectively (5.8): the heat capacities, the group velocities and the phonon lifetimes. This will be the topic of the following discussion. For each of these quantities the contributions per mode for both, the full range and for the range that is obviously most important for thermal transport, will be shown and discussed. As it was done for the thermal conductivity in figure 5.15 always the respective quantity and the product with the phonon density of states are plotted in the following graphs. By doing that, one prevents being misled by peaks at certain frequencies and simultaneously gains understanding of the spectral weight of the contributions.

The first element of the components analysis is the heat capacity C (cf. eq. (3.10)). Having its mathematical origin in the derivative of the Bose-Einstein distribution with respect to temperature, it is the only harmonic ingredient of the thermal conductivity, which accounts for temperature. The comparison of the heat capacity function with the Bose-Einstein distribution was shown in section 3.1 in figure 3.1(a). Since the heat capacity becomes narrower with decreasing temperature, it dictates, which phonon modes a priori come into question for contributing to the thermal conductivity. This quantity, therefore, can be seen as a filter selecting the low-frequency phonons up to a certain energy, which increases with temperature. As can be seen in figure 5.17(a) at the present temperature, some modes with higher frequencies will be suppressed by a vanishing heat capacity. However, the full width at half maximum (FWHM) at 300 K is about 622 cm^{-1} . Therefore, this quantity is not a limiting factor for the thermal conductivity for any of the systems discussed here. If one would go to really low temperatures, however, this could be different, as the plot in figure 3.1 implies. Moreover, in the frequency region, which is relevant for the thermal conductivity, the heat capacities are nearly constant and close to unity⁷ since they only decrease by $10^{-4}k_B$. This means that the heat capacities are completely irrelevant for explaining the differences of thermal conductivity in the present case at 300 K. In the low-frequency region the product of the DOS with the heat capacities essentially reproduces the density of states (see figure 5.14). That means that none of the relevant phonon modes is a priori restricted by the heat capacities at the temperature of 300 K.

The next analysed quantity is the group velocity which is tremendously more important than the heat capacities for the thermal conductivity. Since only the κ_{ii} components do not vanish, no mixed products of the group velocities $v_{g,i}v_{g,j}$ are relevant, but only those with the same component $v_{g,i}v_{g,i} = v_{g,i}^2$. It, therefore, suffices to consider only the squared group velocities in one direction (for instance x). Compared to the heat capacities the analysis of the (squared) group velocities is slightly more difficult.

⁷In units of the Boltzmann constant k_B

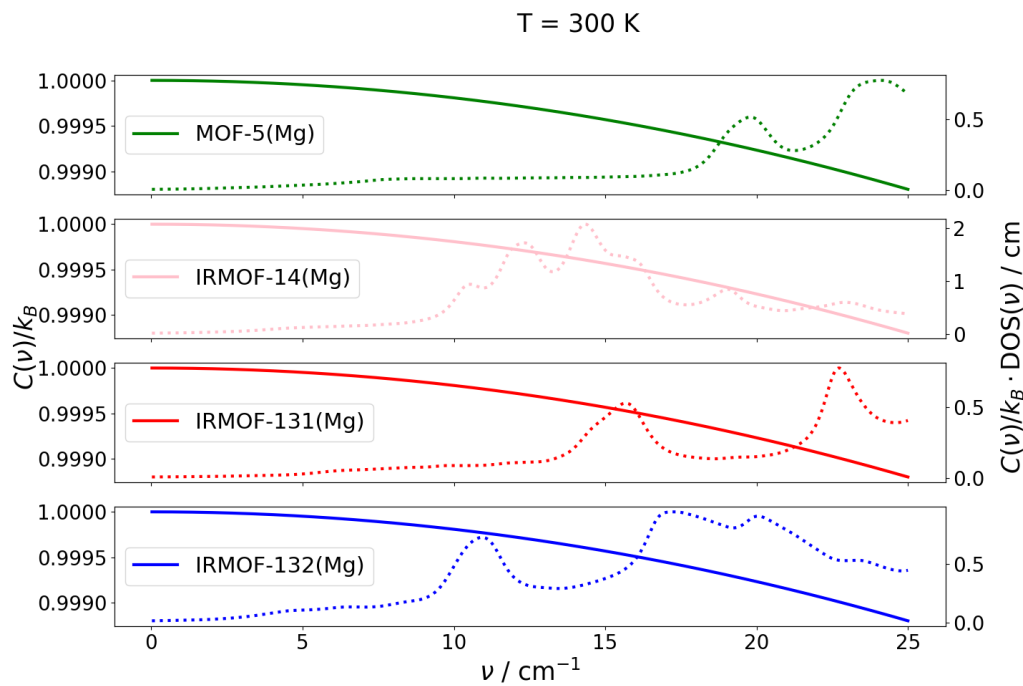
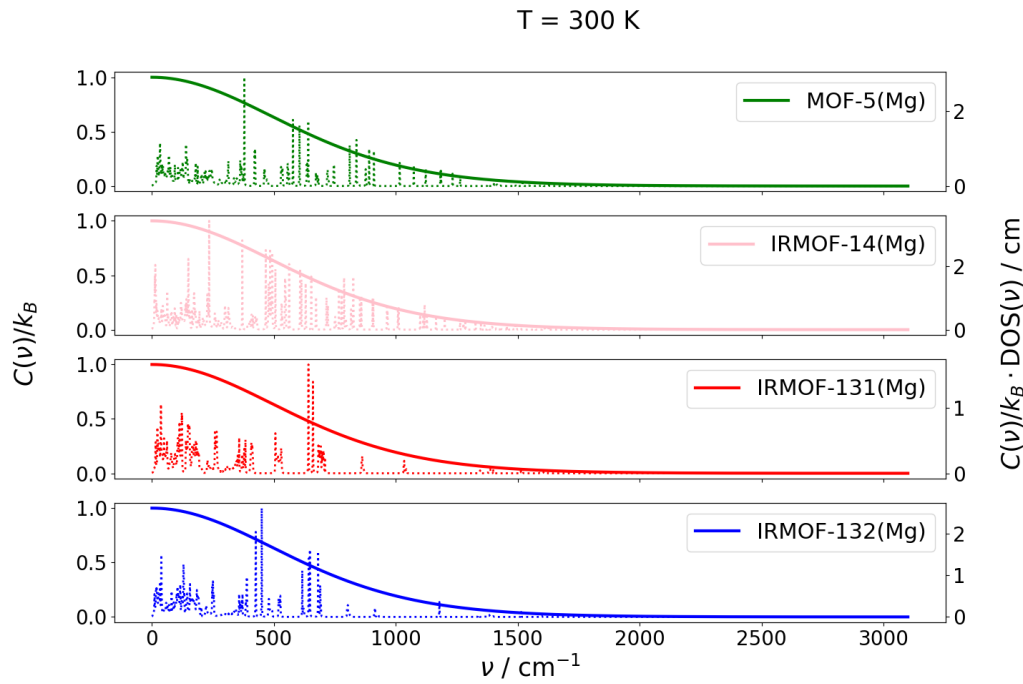


Fig. 5.17: Mode heat capacities (C) (solid lines, left ordinate) and their products with the density of states (DOS) (dotted lines, right ordinate) of selected IRMOFs with different organic linkers in (a) full and (b) the low-frequency (ν) range at 300 K.

5. Results and discussion

The frequency dependence of the group velocities in x direction as well as their products with the DOS can be seen in figure figure 5.18. Since the group velocities per definition vanish at Γ , the frequency range $\nu > 0$ is shown. In the full range plot of figure 5.18(a) it can be seen that there would be contributions from bands at around 1500 cm^{-1} , although the biggest part obviously comes from the low-frequency region of up to 500 cm^{-1} . One can observe some interesting features here. First, for IRMOF-131 and IRMOF-132 having alkyne linkers, the group velocities seem to be greater for the larger system up to a certain frequency. This can be qualitatively understood by looking at the analytical expression for the phonon dispersion of a one-dimensional chain of one atom per unit cell. Here the analytical relation for the group velocity is determined by the unit cell length a , the interatomic force constant C and the mass of the atom m .

$$v_g = a \sqrt{\frac{C}{m}} \cos\left(\frac{q a}{2}\right) \quad \forall q \in \left(0, \frac{\pi}{a}\right] \quad (5.9)$$

For very small wave vectors $q > 0$ the cosine term is approximately unity and a linear dependence on the lattice parameter a can be found. This yields a qualitative argument why larger systems have the tendency to show greater group velocities. The reason, why this quantitative argument does not apply for IRMOF-14, is probably the higher vibrational mass m in the case of IRMOF-14 compared to MOF-5. Whereas the gain of cell length a between IRMOF-131 and IRMOF-132 can be attributed to the introduction of only a few additional atoms, one increases the number of atoms in the system much more by replacing the linkers of MOF-5 with those of IRMOF-14. This is supposed to increase the effective vibrational mass more than the length of the cell parameter. As a result, the acoustic group velocities decrease, as it is observed for IRMOF-14. According to these considerations, if one wants to have higher (acoustic) group velocities, it is beneficial to use molecules as linkers that, on the one hand, have as few branchings as possible and, on the other hand, increase the distance between the nodes as much as possible.

Furthermore one can see from the zoomed in frequency range in figure 5.18 that there is a region of significantly decreased $\{v_g^2 \cdot \text{DOS}\}$ in IRMOF-14 at about 15 cm^{-1} . This can be explained by looking at the band structure of figure 5.12(b). In exactly that region IRMOF-14 has several quite flat bands, for which the group velocities are close to zero. However, the DOS is relatively high due to the same flat optical bands (between 10 and 15 cm^{-1}), which could compromise the low group velocities in the product with the DOS. The more convincing argument for the dip is the fact that the acoustic bands flatten out in this region as well. Therefore, fewer bands show a relevant dispersion. One can clearly see in the left ordinates (solid lines) in figure 5.18 that the group velocities increase up to certain frequencies, before they rather abruptly decrease. This can be assigned to the interference of the flat optical bands and the flattening out of the acoustic ones. Interestingly, neither the group velocities are the limiting factor for the thermal conductivity, since there would be contributions far above 25 cm^{-1} , which are obviously suppressed by the remaining quantity that has not been discussed yet.

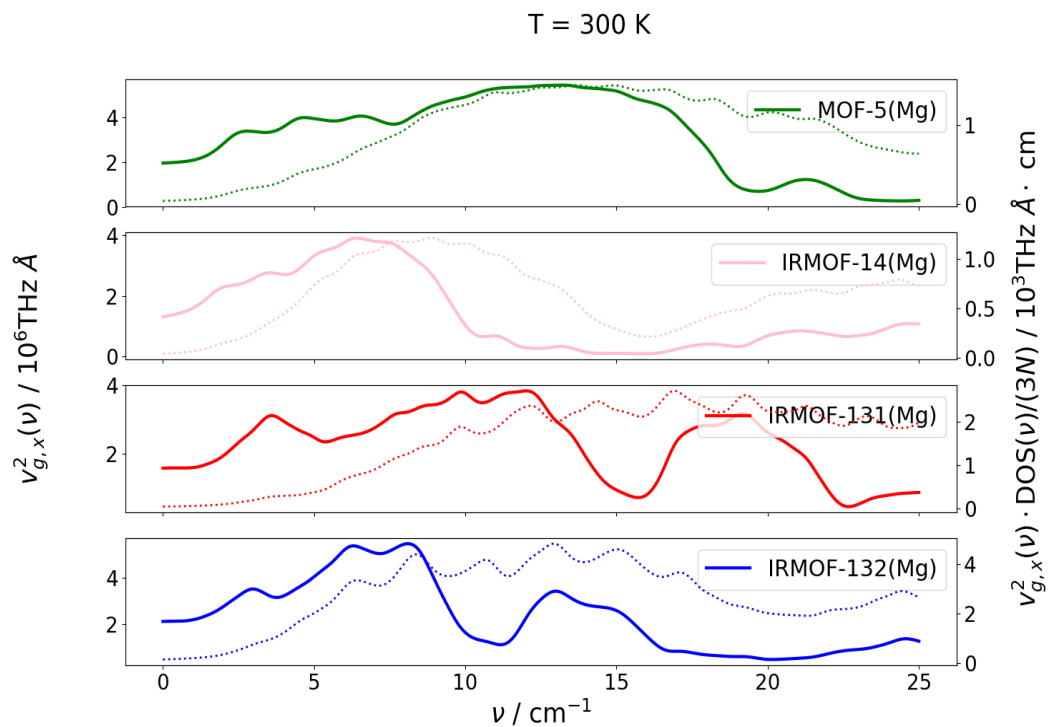
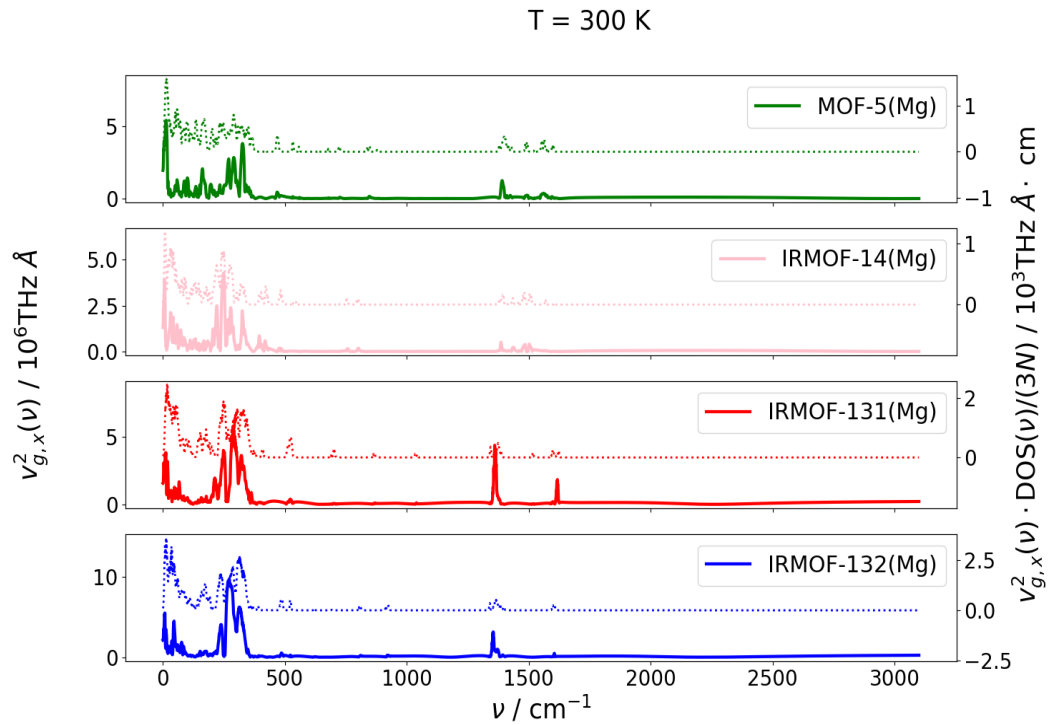


Fig. 5.18: Mode contributions of the squared group velocities in x direction ($v_{g,x}$) (solid line, left ordinate) and their products with the density of states (DOS) (dotted lines, right ordinate) of selected IRMOFs with different organic linkers in (a) full and (b) the low-frequency (ν) range.

5. Results and discussion

The phonon lifetimes according to the used models depend (inversely) on the mean squared Grüneisen parameter (MSGP) $\langle \gamma^2 \rangle$ (cf. eq. (3.29)), which is the average squared mode Grüneisen parameter weighted with the heat capacities (cf. eq. (3.28)). In this model, a higher MSGP will also result in shorter phonon lifetimes. This is understandable by the fact that the MSGP is an indicator of how anharmonic a system is. For perfectly harmonic systems, one would find only vanishing Grüneisen parameters. Therefore, one has to consider the MSGP first before discussing the phonon lifetimes. The mean squared Grüneisen parameters for the studied systems are displayed in figure 5.19. The left hand side of the plot shows the evolution of this quantity for MOF-5 with different metallic nodes, whereas the influence of the varied linkers are plotted in the right hand side, with only the latter being relevant for the current discussion.

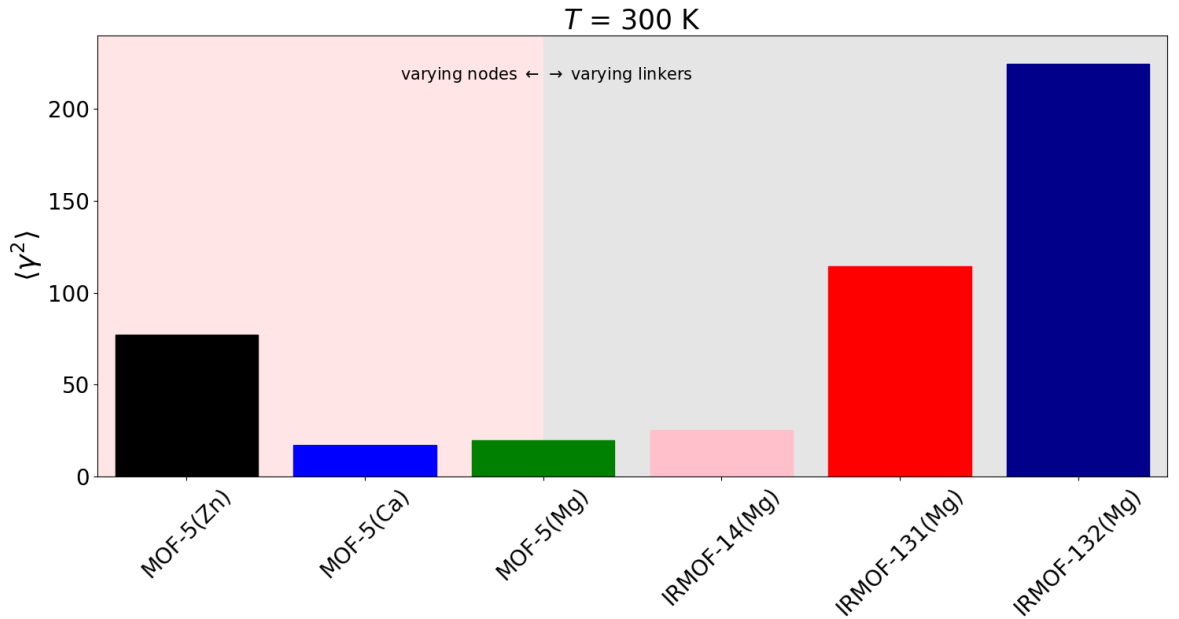


Fig. 5.19: Mean squared Grüneisen parameters at a temperature of 300 K for the studied MOFs according to eq. (3.28).

Tab. 5.3: Quantities relevant for the calculation of the phonon lifetimes according to the model of Bjerg et al. (cf. eq. (3.25).)

System	$\langle \gamma^2 \rangle _{T=300\text{ K}}$	Θ / K	$\frac{\Theta}{T_p(\langle \gamma^2 \rangle)} \exp \left\{ \frac{\Theta}{3T} \right\} \Big _{T=300\text{ K}} / \text{THz}$
MOF-5(Zn)	77	33.12	4.99
MOF-5(Ca)	17	50.95	55.61
MOF-5(Mg)	20	54.25	43.28
IRMOF-14(Mg)	25	25.90	10.00
IRMOF-131(Mg)	114	72.10	12.35
IRMOF-132(Mg)	225	52.45	5.12

It can be seen in figure 5.19 that the systems with aromatic linkers show MSGP that are about one order of magnitude less than those for the alkyne linker systems. This means that IRMOF-131 and IRMOF-132 appear to have a significantly larger degree of internal anharmonicity compared to MOF-5 and IRMOF-14, with the tendency increasing with the linker length. However, the MSGP are not the only factor of influence for the phonon lifetimes according to the used model. Considering equation (3.25), the temperature scaling factor Θ and the empirical function $p(\langle\gamma^2\rangle)$ (also containing the unit cell volume, the average mass, the temperature scaling factor and the Debye frequency; see eq. (3.29)) play an important role. Since the individual mode information in this equation for the phonon lifetimes $\tau_n(\mathbf{q})$ has its origin in the $\omega_n(\mathbf{q})^{-2}$ term, the remaining factors can be combined to a common prefactor, which is constant for every band and mode at a given temperature. The temperature scaling factors, the MSGP and this prefactor $\tau_n(\mathbf{q}) \omega_n^2(\mathbf{q}) = \frac{\Theta}{Tp(\langle\gamma^2\rangle)} \exp\left\{\frac{\Theta}{3T}\right\}$ are shown in table 5.3. The frequency dependence of the phonon lifetimes as well as their products with the respective DOS can be seen in figure 5.20. Note that according to the model function (see eq. (3.25)) the lifetimes diverge at 0 cm^{-1} . This divergence is counteracted by vanishing group velocities at Γ .

In the full range plot of the respective figure the expectation is confirmed that the lifetimes are the crucial quantities, which limit the thermal conductivity to that narrow frequency region. From the low-frequency range plot in figure 5.20(b) one also can find the same ranking for the lifetimes as the prefactors in the last column of table 5.3 suggest. Several interesting features can be observed. First, for similar linkers - i.e. aromatic or alkyne - always the system with a larger unit cell respectively more atoms in the unit cell shows decreased phonon lifetimes and greater anharmonicities. This is somehow obvious since more atoms will contribute to the total PES in a way that the harmonic approximation is even less fulfilled. Alternatively, one can think of it in the following picture. If there are more atoms in the unit cells, there are more modes which others can scatter at, which decreases their lifetimes as a result. It would be interesting, however, to study hypothetical systems that have the same number and species of atoms, but different lattice parameters in order to separate the two possible influences from each other. This is one of the reasons why the metallic nodes were varied as well as described in section 5.3.3. Furthermore, it can be seen that IRMOF-131 shows only slightly increased phonon lifetimes compared to IRMOF-14. However, for IRMOF-131, the optical bands appear at higher frequencies (approx. 15 cm^{-1}) compared to IRMOF-14 (approx. 10 cm^{-1}). Therefore, the small difference in thermal conductivity between IRMOF-131 and IRMOF-14 is determined by the group velocities, since the lifetimes are very similar and the heat capacities do not play a role in that narrow frequency region for that temperature. Although IRMOF-132 shows the highest degree of anharmonicity, resulting in the lowest phonon lifetimes, the absolute values of the group velocities are relatively high. As a result, the thermal conductivity is not much lower than for IRMOF-131 and IRMOF-14. Comparing IRMOF-132 with IRMOF-14, one can see that, although the lifetimes are higher for IRMOF-14, there are contributions from the group velocities up to higher frequencies for IRMOF-132. Thus, κ of IRMOF-132 is not that much lower as one would expect after seeing only the lifetimes.

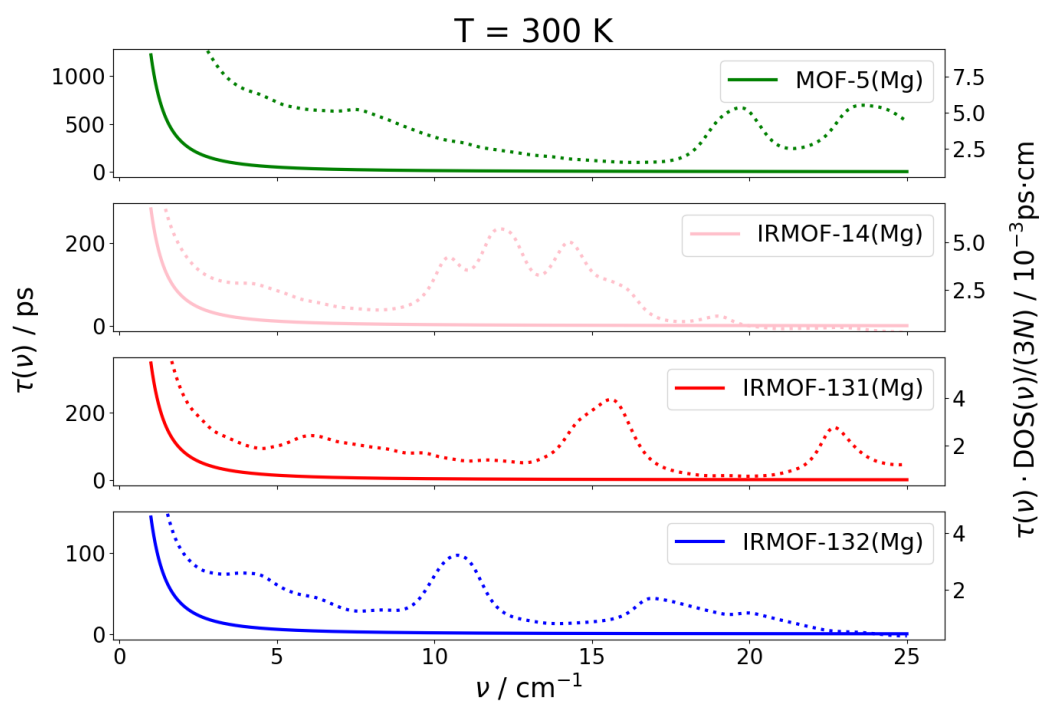
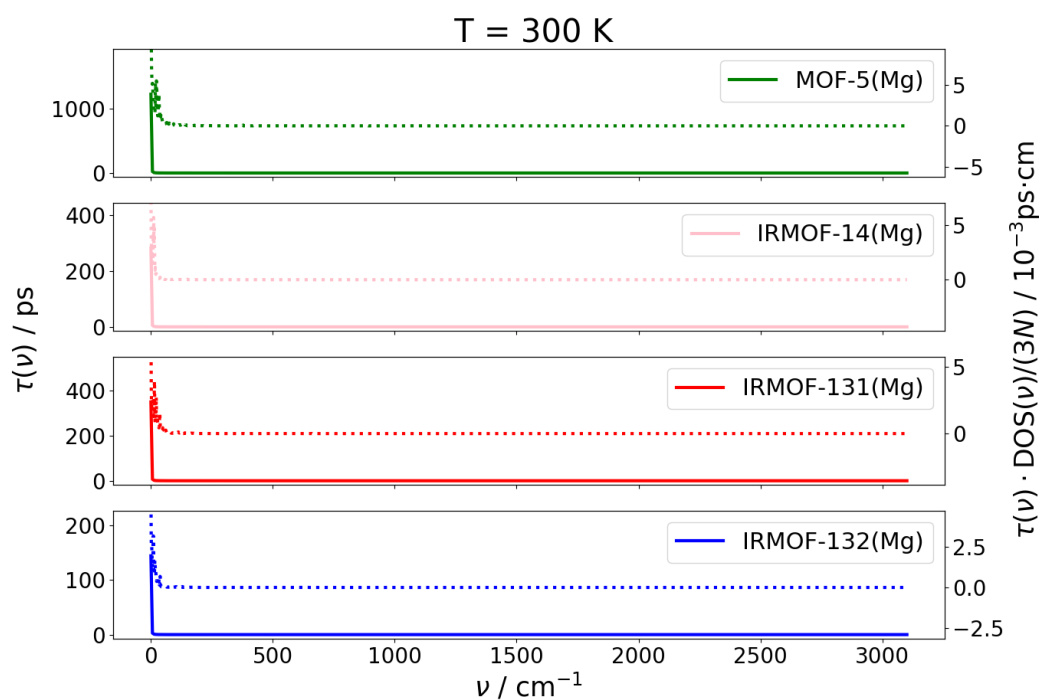


Fig. 5.20: Mode dependent phonon lifetimes (τ) (solid lines, left ordinate) and their products with the density of states (DOS) (dotted line, right ordinate) of some IRMOFs with different organic linkers in (a) full and (b) the low-frequency (ν) range at 300 K.

In summary, MOF-5 shows the highest thermal conductivity compared to the other three investigated systems with different linkers. Quantitatively, it can be said that the thermal conductivity is higher for shorter organic linkers, provided that the anharmonicities are not too large. By analysing the mode contributions of all physically relevant quantities, the following observations can be made.

Regarding the heat capacities, it can be seen that at higher temperatures (cf. fig. 5.17) they are not a limiting factor for the frequency region of mode contributions, since the FWHM at 300 K is about 622 cm^{-1} . In other words, the heat capacity function decays so slow with increasing frequency that the low-frequency modes stay nearly unaffected. Concerning the analysis of the group velocities, the tendency that was found is that for systems with larger lattice constant, greater (squared) group velocities for low frequencies up to a certain point can be expected. This statement, however, has to be seen with caution. For IRMOF-131 and IRMOF-132 there are only a few carbon atoms that make the difference between the structures and mainly influence the length of the unit cell. For IRMOF-14 there are two effects. On the one hand, the larger unit cell quantitatively yields higher group velocities according to equation (5.9). Secondly, by introducing a higher number of atoms (84 more than MOF-5) one increases the degree of inertia of the system (higher effective vibrational mass m in equation (5.9)), what counteracts the effect of an increased lattice constant. Moreover, the additional atoms result in further optical bands. These bands correspond to vibrations within the aromatic linkers. Therefore, some of the bands do not appear for MOF-5 due to the smaller number of linker atoms compared to IRMOF-14.

Regarding the phonon lifetimes, the two main influences were found to be the mean squared Grüneisen parameter (MSGP) and the temperature scaling factor Θ of equation (3.25). In all studied cases, the temperature scaling factor was observed to decrease as the cell volume increases. This trend can be put down to the fact that in those systems the acoustic bands flatten out at lower frequencies, thus, reducing the cutoff frequency for the evaluation of equation (3.30). Furthermore, it could be observed that the systems with alkyne linkers show a much larger degree of anharmonicities of the PES. This can be found by analysing the mean squared Grüneisen parameters (cf. fig. 5.19), which are about one order of magnitude higher for IRMOF-131 resp. IRMOF-132 compared to MOF-5 resp. IRMOF-14. The presence of these anharmonicities decreases the phonon lifetimes of the system considerably. By this effect, the mode contributions to the thermal conductivity of the group velocities of IRMOF-131, which are comparable in magnitude to that of MOF-5, are suppressed by the low phonon lifetimes. In order to see whether the tendency of increasing mean squared Grüneisen parameters continues for longer linkers in the same manner, it would be interesting to study thermal transport also for a MOF with linkers containing oct-2,4,6-triyne and even longer linear alkyne chains or more extended aromatic molecules. A very brief discussion of a MOF with an even shorter linker can be found in appendix A.4.

5.3.3. Influence of the metallic nodes

Besides the influence of different organic linkers on the thermal transport properties of MOFs, one can also study the effects of different metals in the system. Varying metal atoms introduce more or less additional mass to the systems. From the simplistic model of the one-dimensional chain with two atoms in the primitive unit cell, which was introduced in section 1, one can learn the basic effect of higher masses: the phonon bands flatten out and the degree of dispersion is reduced. This is another way of saying that the vibrations in real space become more localised. Increasing localisation of phonons suggests inhibited thermal conductivity. Therefore, the MOF-5 structure was investigated with Mg, Ca, and Zn atoms in the metallic nodes. According to the IUPAC [60], the respective masses of those atoms are 24.305 u, 40.078(4) u, respectively 65.38(2) u.

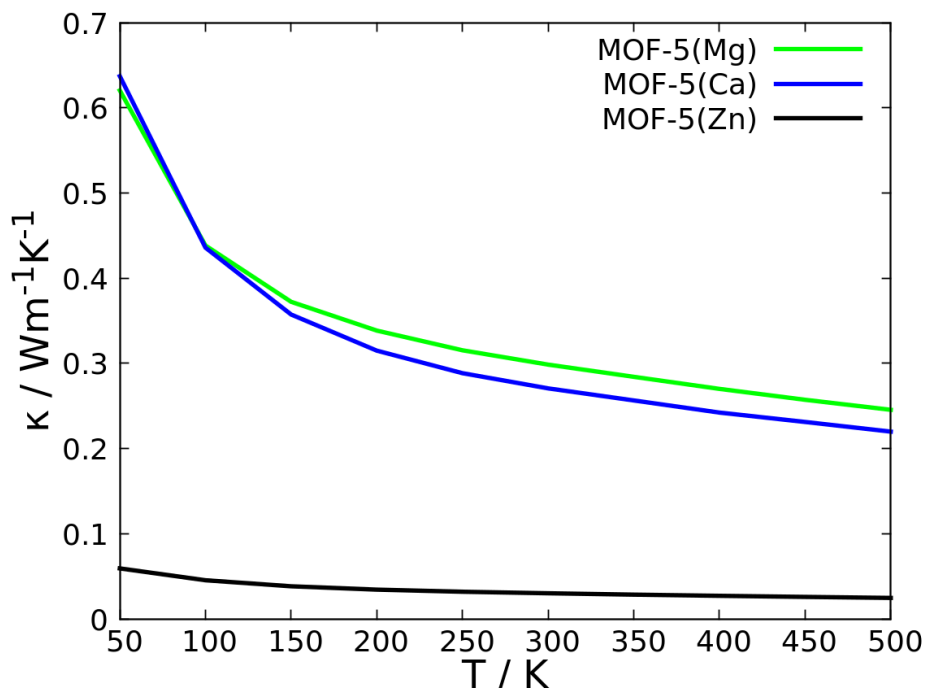


Fig. 5.21: Calculated thermal conductivity (κ) as a function of temperature (T) of MOF-5 with different metallic nodes.

The first observation one can make concerns the lattice parameters a as defined for an fcc lattice in equation (5.4). By searching for the optimal size of the systems with DFTB+ and Bayesian probability theory as described in section 4.3, the lattice parameter of MOF-5(Mg) could be determined as $a = (13.165 \pm 0.001) \text{ \AA}$, $a = (13.798 \pm 0.003) \text{ \AA}$ for MOF-5(Ca) and $a = (13.189 \pm 0.001) \text{ \AA}$ for MOF-5(Zn). The given uncertainty is the square root of the respective probability density function as described earlier. It might appear contra-intuitive that Ca with a lower atomic number than Zn causes an increased volume. However, when one considers the size⁸ of the atoms in terms of their covalent

⁸The author is well aware of the fact that quantum-mechanically speaking an atom does not have a

atomic radii, one can see that Ca tends to bind to other atoms with larger distances than Zn and Mg, which are relatively similar in this comparison of their atomic radii [17, p. 141].

The resulting thermal conductivities are displayed in figure 5.21. It can be seen that the intuitive expectation one would have, is confirmed since the thermal conductivity decreases with increasing mass of the metal atoms, although no straightforward relation can be observed.

In figure 5.22 the phonon band structure for all three studied systems is shown. By comparing the plots for each system, one can find that for MOF-5(Mg) the acoustic bands have the biggest slopes i.e. larger group velocities. Especially at the high symmetry point W the band minimum reaches to lower frequencies compared to MOF-5(Ca) and MOF-5(Zn), and the acoustic band along the path X-W-K shows considerably more dispersion. Furthermore, the (transversal) acoustic bands flatten out at higher frequencies in the case of MOF-5(Mg) compared to the other two systems. Another interesting feature concerns the optical band that has a nearly constant frequency for all \mathbf{q} points in MOF-5(Mg) at about 20 cm^{-1} . This band corresponds to torsional modes of the phenyl rings along the linker axis. It seems to go down in energy for increasing atomic mass of the metal. For the system of MOF-5(Zn) it can be seen that the phonon modes of this band seem to interact with the acoustic band. Avoided crossings are present, the most distinct one being near Γ along the Γ -X path. This mode interaction results in an overall flattening of the bands that occurs at lower frequencies compared to the systems with the alkaline earth metal systems. Due to the lower frequency, at which the acoustic bands hit the Brillouin zone boundary, the cutoff frequency ν_{cut} is reduced, which is used to truncate the integrals in the calculation of the temperature scaling factor according to equation (3.30). As a consequence, this circumstance has an influence on the Θ temperature scaling factor, having a direct impact on the phonon lifetimes according to equation (3.25).

Another interesting feature, which one can recognise from visual inspection of the band structure, is that along the \mathbf{q} point path Γ -X there is a splitting of the two transversal acoustic bands in the case of MOF-5(Zn). After it has been assured, by comparison of the band structure with the one computed with a larger super cell, that the reason for the splitting of the transversal acoustic bands is not insufficient convergence of the force constants, the symmetries of the systems were compared. It turned out that the symmetry in the relaxed geometry of MOF-5(Zn) is reduced compared to MOF-5(Mg) and MOF-5(Ca) and that no increased tolerance of phonopy could restore it. While for MOF-5 with the alkaline earth metals the symmetry analysis revealed the space group $Fm\bar{3}m$ (225), the slightly less symmetric cubic space group $Fm\bar{3}$ (202) was found for MOF-5(Zn). This can be explained by investigating the geometry of MOF-5(Zn) in more detail. It turns out that in the systems with higher symmetry (MOF-5(Mg) and MOF-5(Ca) with space group $Fm\bar{3}m$), all phenyl rings of the linkers lie in planes, which are aligned along the face diagonals of the cubic cell. The phenyl rings of MOF-5(Zn) show a slightly different dihedral angle, what obviously disturbs the symmetry of the

defined size, but rather its extent in space decays with distance, with approaching 0 at infinity.

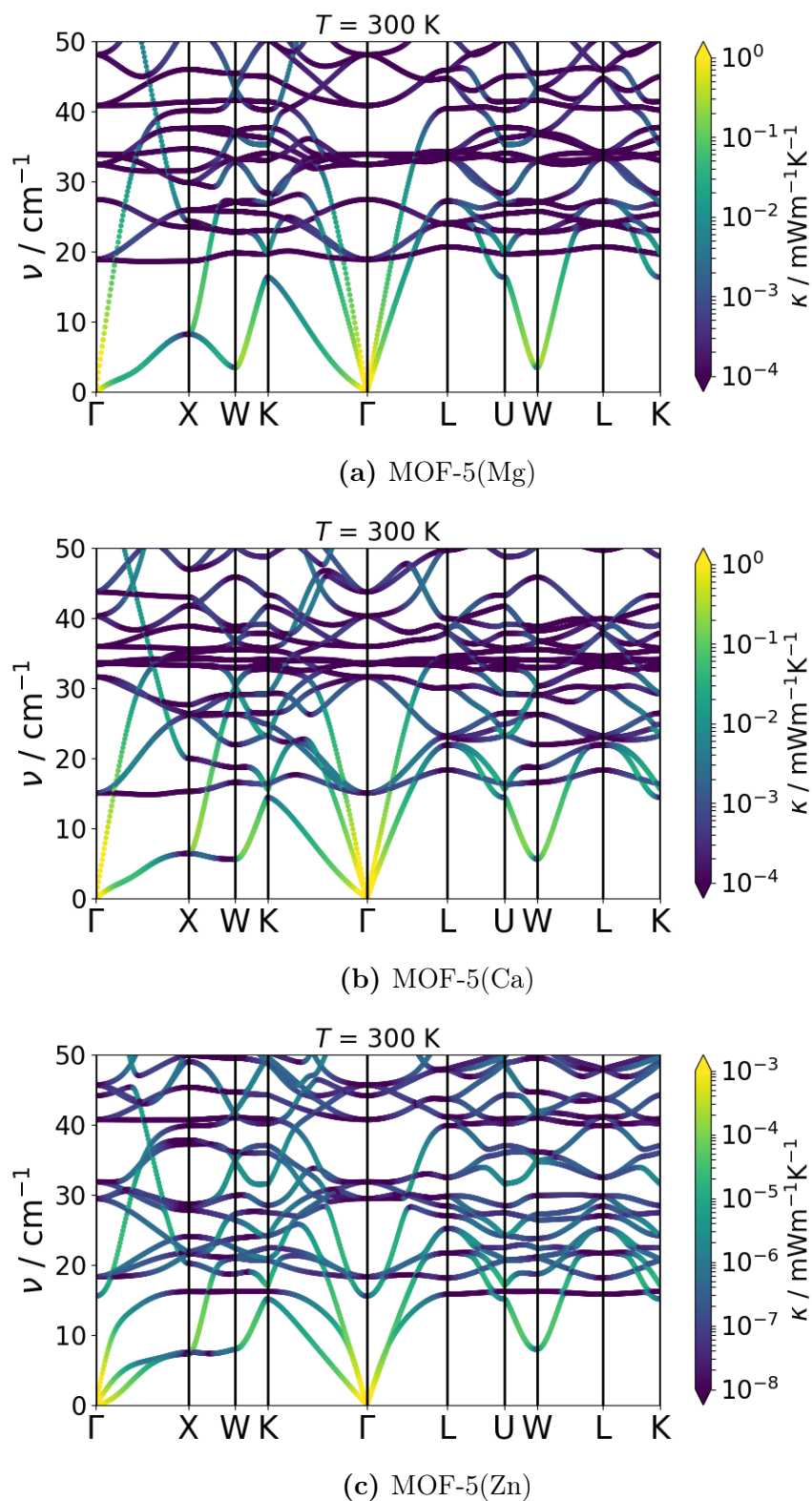


Fig. 5.22: Phonon band structure of the MOF-5 structure where the metallic nodes were varied. All the systems have an fcc Bravais lattice. The bands are coloured in a logarithmic scale showing the contribution to the thermal conductivity κ per \mathbf{q} point and mode.

system. A measure for this misalignment is the dihedral angle between the face diagonal plane and the plane of the phenyl ring $\Delta\phi \approx 4.6^\circ$. For better understanding, the geometry of MOF-5(Zn) is compared with that of MOF-5(Mg) in figure 5.23. Interestingly, for lattice constants $a > 13.4 \text{ \AA}$, much larger than the found equilibrium value, the space group with more symmetries is restored. This means that the symmetries and the band structure could be manipulated by varying the external pressure.

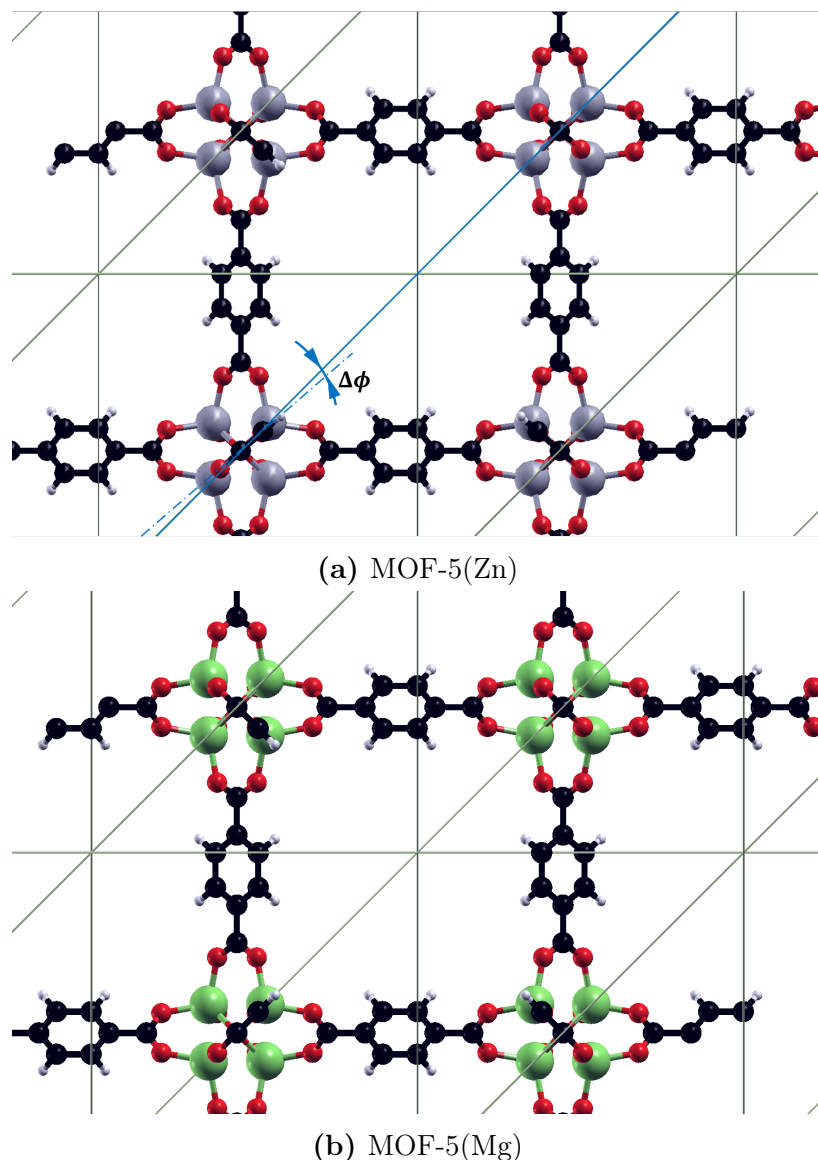
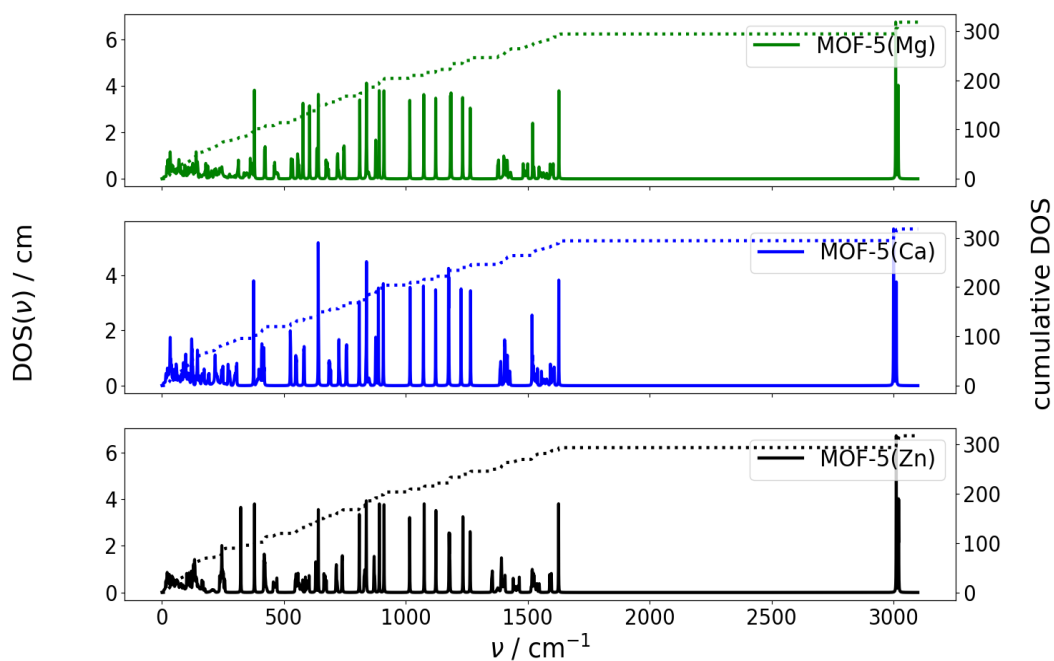
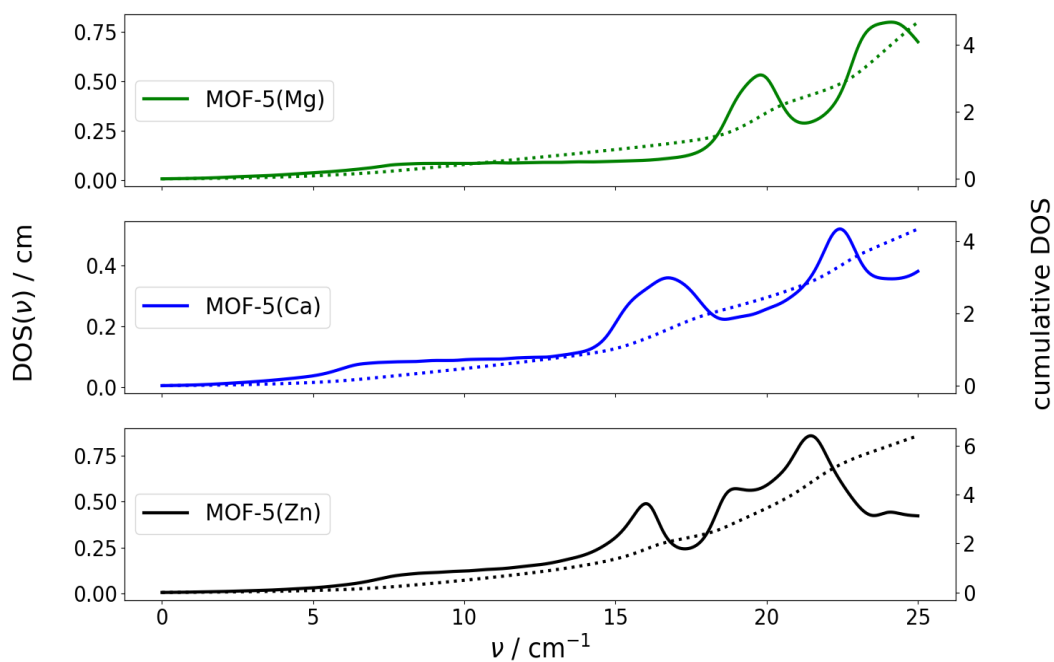


Fig. 5.23: Geometries of MOF-5(Zn) and MOF-5(Mg) relaxed with DFTB+. The linkers of MOF-5(Zn) pointing out of the paper plane are not perfectly aligned with the planes, which correspond to the lines drawn with an angle of 45° between the long molecular axes of the linkers of one face of the cubes. The result is the dihedral misalignment $\Delta\phi$.



(a) Full range



(b) Zoomed in range

Fig. 5.24: Density of states (DOS) of MOF-5 with with different metallic nodes in (a) full and (b) the low-frequency (ν) range. The cumulative DOS is plotted as dotted line on the secondary ordinates.

Finally, it can be seen in the band structures that the longitudinal acoustic bands - i.e. in the present cases, the acoustic bands with the highest frequency - contribute more to the thermal conductivity than the transversal acoustic bands. This can be explained by the fact that the longitudinal ones have greater slopes, which enter squared in the equation of the thermal conductivity.

By converting the integral over the \mathbf{q} points of the first Brillouin zone to an integral over frequencies by using the phonon DOS (cf. eq. (5.8)), the contribution per phonon frequency can be obtained, as it was done for the linker variation in the previous section. The DOS for the three investigated systems is shown in figure 5.24, broadened in the same way as in section 5.3.2 ($\sigma = 0.5 \text{ cm}^{-1}$). As it could have been expected by now, the relevant frequency region is a small part of the spectra, restricted to an interval of 0 to approximately 25 cm^{-1} . Both, the full and a zoomed in range of the products of the contributions to the thermal conductivity and the phonon density of states $\{\kappa_{xx} \cdot \text{DOS}\}$ can be seen in figure 5.26 in order to illustrate that absolutely no effect comes from higher frequency. The mode contribution without multiplication with the DOS can be found in figure 5.25 so that one can distinguish between frequencies with just a high density of states and ones, which really tend to be more important for the thermal conductivity.

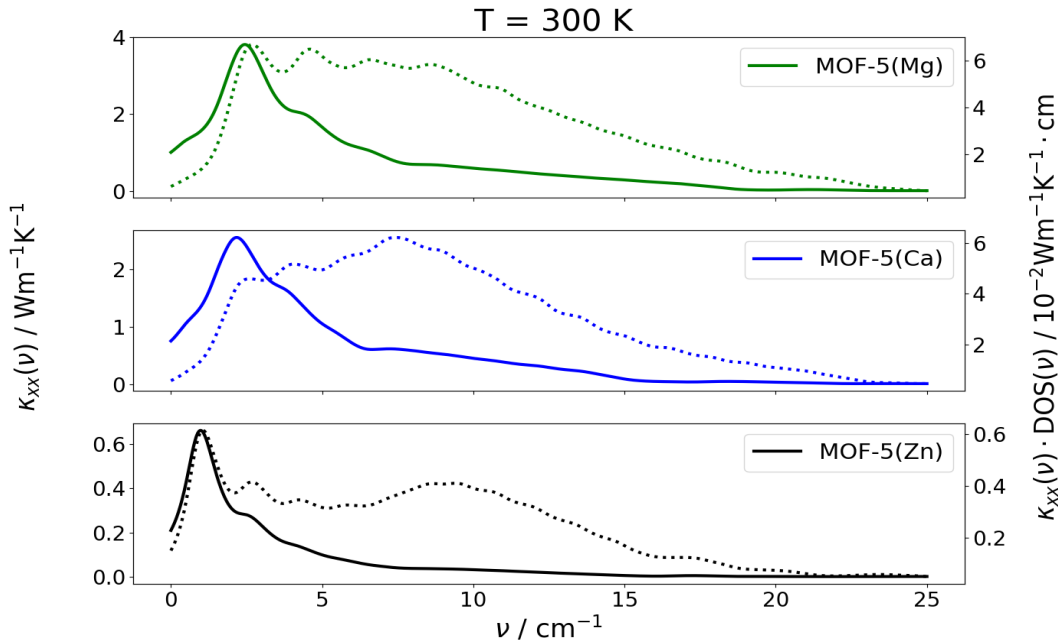
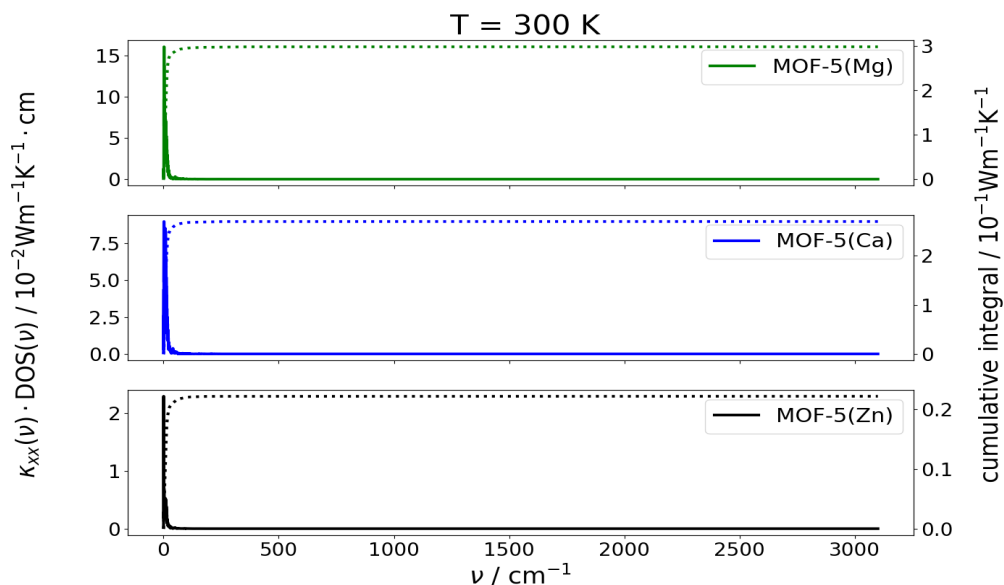
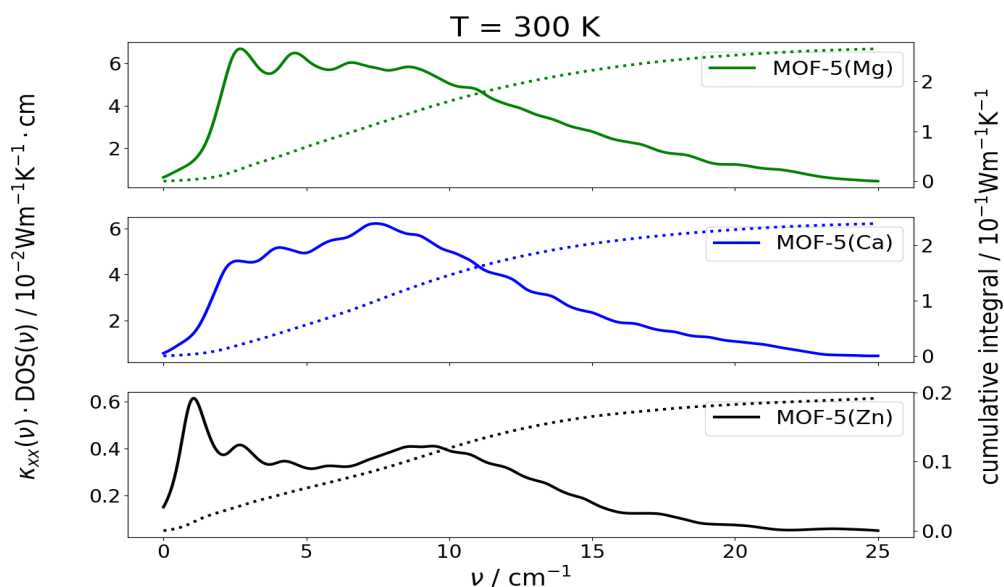


Fig. 5.25: Mode contributions to the thermal conductivity (κ_{xx}) (solid lines, left ordinate) and their products with the density of states (DOS) (dotted lines, right ordinate) of MOF-5 with different metallic nodes in low-frequency (ν) range at 300 K.



(a) Full range



(b) Zoomed in range

Fig. 5.26: Mode contributions to the thermal conductivity (κ) multiplied with the density of states (DOS) of MOF-5 with different metallic nodes in (a) full and (b) the low-frequency (ν) range at 300 K. The cumulative integrals are plotted as dotted lines on the secondary ordinates.

These plots show that the general behaviours of the contributions for MOF-5(Mg) and MOF-5(Ca) are very similar, except for the region from about 3 to 8 cm^{-1} with slightly

enhanced contributions in the case of MOF-5(Mg). This can be understood by looking at the band structure plots of figure 5.22. The enhanced contributions are assumed to stem from the regions of higher dispersion along the X-W path and from the band minimum at W, which happens to extend far down to lower frequencies, where besides the group velocities also the phonon lifetimes are larger within the assumed model. This region up to about 8 cm^{-1} seems to be the main reason why the thermal conductivity of MOF-5(Ca) is not quite as high as for MOF-5(Mg).

For MOF-5(Zn), however, the situation is rather different. Apart from the relatively large contributions at 0 to 3 cm^{-1} , there is only a more or less extended background of thermal conductivity contributors which have already decayed when the frequency of 25 cm^{-1} is reached. Note that even the initial high contributions are reduced by a factor of approximately 3 compared to MOF-5(Ca) in that region. It is, therefore, obvious that the thermal conductivity is so much lower in MOF-5(Zn) compared to the other systems. Why exactly this is the case, is the topic of the following discussion.

Conducting the same analysis for the variation of the metallic nodes as before, one can start with discussing the quantity that is least likely to have a huge impact on the contributions. The mode-dependent contributions to the heat capacity at a temperature of 300 K can be seen in full and the low-frequency range in figure 5.27. The heat capacity function (solid lines) at this temperature is still broad enough to cover a region extending to much higher frequencies than the relevant region for the thermal conductivity. Like it has been found when comparing different organic linkers, the heat capacity is nearly completely irrelevant for the differences of thermal conductivities between the three systems at this temperature.

Much more important is the influence of the group velocities which can be seen in figure 5.28. As for the MOFs with different linkers, both, the squared x -component of the group velocities and their products with the DOS (normalised with $\int d\nu D(\nu) = 3N$) are shown. For all three systems, high-frequency contributions around 1500 cm^{-1} exist that will be cancelled by vanishing phonon lifetimes and mode-dependent contributions to the heat capacity in that region. In the detailed plot of figure 5.28 one can see that MOF-5(Mg) shows the greatest group velocities of the three investigated systems. A small dip in the frequency-dependent (squared) group velocities can be found between 5 and 10 cm^{-1} in every case. The origin of this small minimum is probably the flattening out of the transversal acoustic bands, which can be seen in figure 5.22 along the Γ -X-W path. For MOF-5(Zn) the group velocities are not reduced so drastically as one would expect from seeing the relatively low thermal conductivity. In the interesting frequency region it is comparable to MOF-5(Mg) and MOF-5(Ca), with the squared absolute values differing by about a factor of 2 between MOF-5(Mg) and MOF-5(Zn). So, the group velocities alone would not be able to explain the rather significant differences in thermal conductivities between the systems. The last group velocity related feature that should be discussed is that MOF-5(Zn) shows relatively large peaks at about 500 and 1400 cm^{-1} . This means that there are band slopes for those higher frequencies that are even comparable with those of the acoustic bands near Γ . If one could find a temperature ($< 300 \text{ K}$), where, on the one hand, the phonon lifetime decays slowly enough to make these vibrations accessible and, on the other hand, the heat capacity function

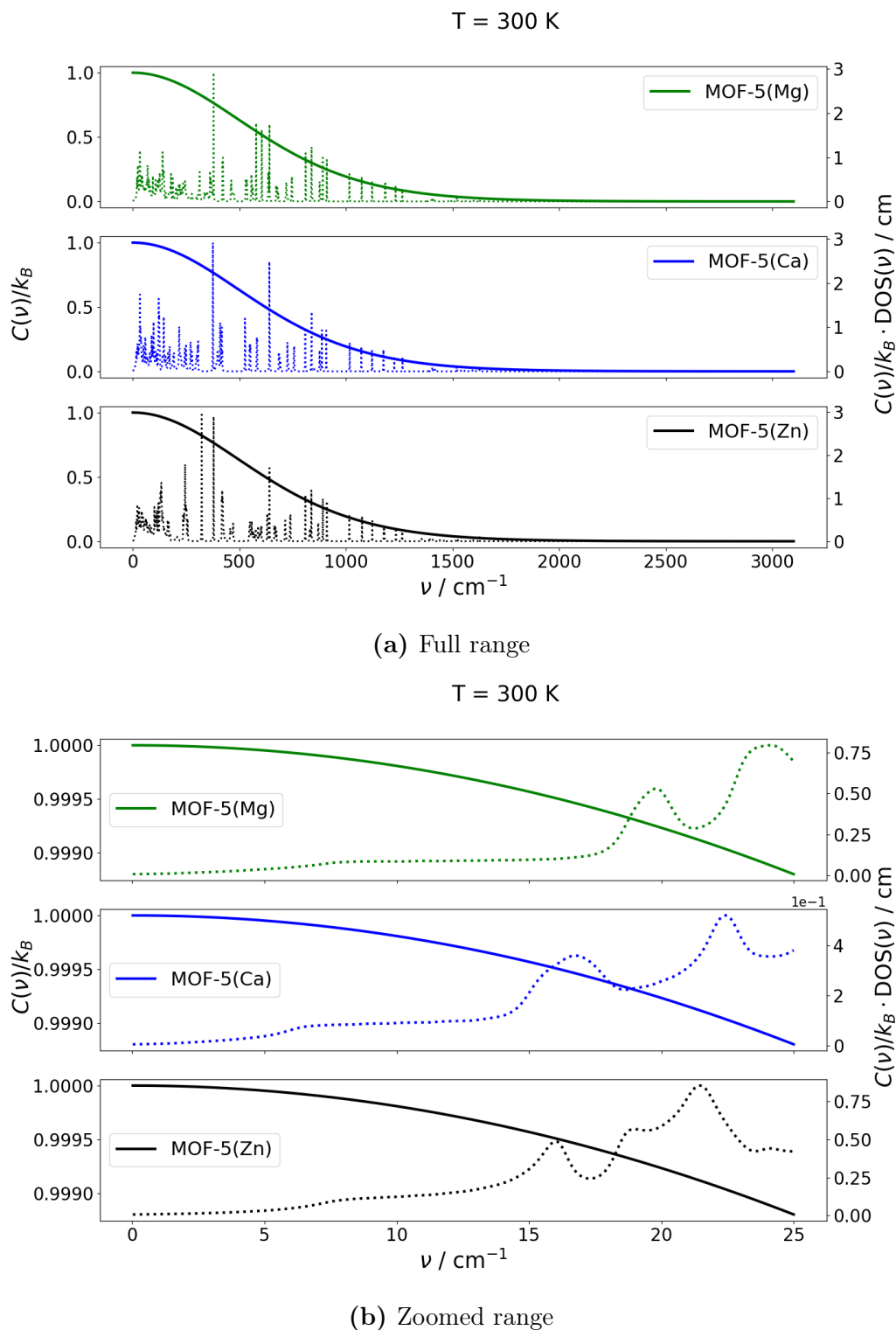


Fig. 5.27: Mode heat capacities (C) (solid lines, left ordinate) and their products with the density of states (DOS) (dotted lines, right ordinate) of MOF-5 with different metallic nodes in (a) full and (b) the low-frequency (ν) range at 300 K.

(see eq. (3.10), fig. 3.1) still extends to high enough frequencies, it is very likely that the thermal conductivity of MOF-5(Zn) increases more than those of MOF-5(Mg) and MOF-5(Ca) would.

Finally, the most interesting quantities that appear to constrain the relevant contributions from the group velocities to that rather small frequency range, the phonon lifetimes, are shown as the (properly normalised) product with the density of states in figure 5.29. The main reason for the decreased thermal conductivity of MOF-5(Zn) compared to the other two systems are, therefore, the lower phonon lifetimes that are reduced by about a factor of 10. This can be rationalised by looking at the relatively large MSGP of MOF-5(Zn) as displayed in figure 5.19 and the prefactors according to equation (3.25) listed in table 5.3. The higher MSGP, which are a measure of anharmonicities in the system, and the lower temperature scaling factor Θ directly decrease the phonon lifetimes. If this was not the case, MOF-5(Ca) and MOF-5(Zn) would have very similar thermal conductivities as their group velocities are both in the same range, while those of MOF-5(Mg) are slightly higher.

Another very interesting feature that is directly related to the previous discussion about the phonon lifetimes is the fact that for low temperatures (< 100 K) MOF-5(Ca) appears to have a higher thermal conductivity than MOF-5(Mg). This can be understood in the following way. Obviously, MOF-5(Ca) has a lower degree of anharmonicity, which results in a slightly smaller mean squared Grüneisen parameter (MSGP) than MOF-5(Mg). Therefore, for low temperatures the phonon lifetimes increase, while the heat capacity envelope becomes narrower and narrower. When the heat capacities become the limiting quantity, only the group velocities of the very low frequency modes can contribute. Those modes, however, are then mainly the acoustic ones, where the group velocities do not differ significantly between MOF-5(Mg) and MOF-5(Ca). If the group velocity influences are (roughly) the same for both systems, the only remaining effect is that of the phonon lifetimes, which is higher for MOF-5(Ca) due to the lower MSGP. Therefore, for low temperatures, MOF-5(Ca) supersedes MOF-5(Mg) as the system with the highest thermal conductivity.

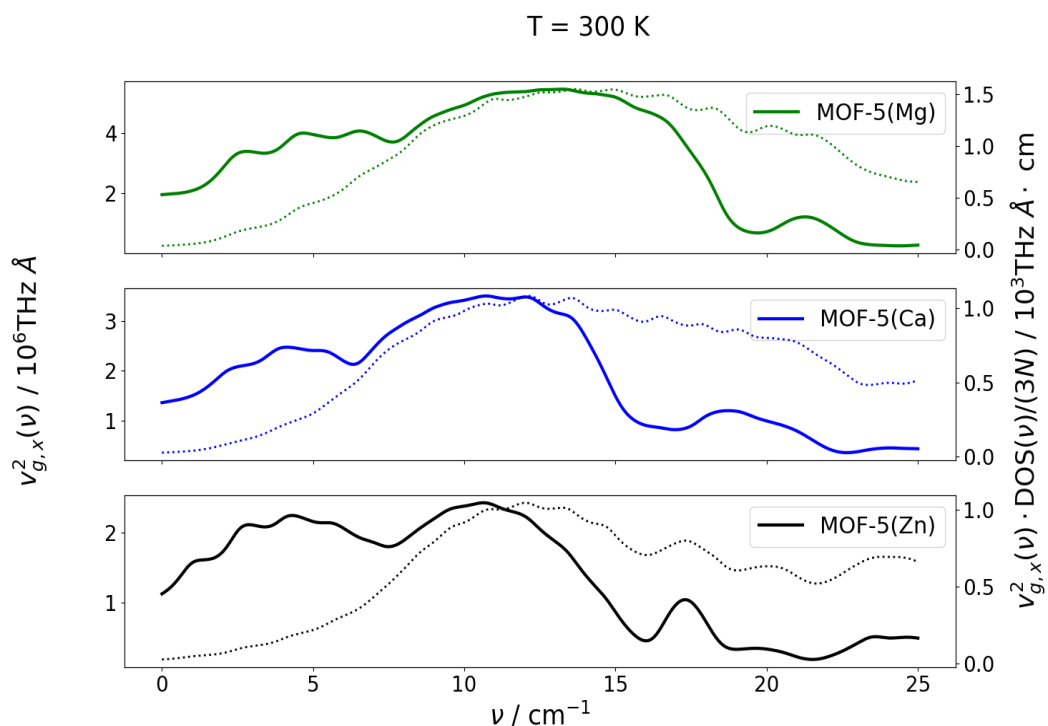
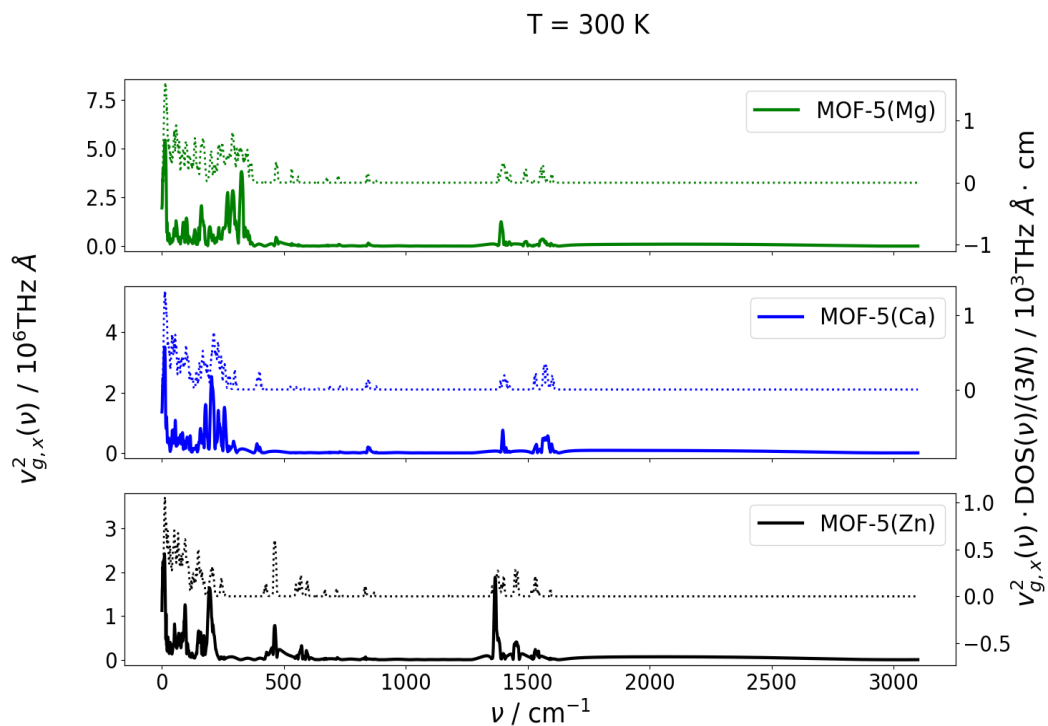


Fig. 5.28: Mode contributions of the squared group velocities in x direction ($v_{g,x}$) (solid line, left ordinate) and their products with the density of states (DOS) (dotted line, right ordinate) of MOF-5 with different metallic nodes in (a) full and (b) the low-frequency (ν) range.

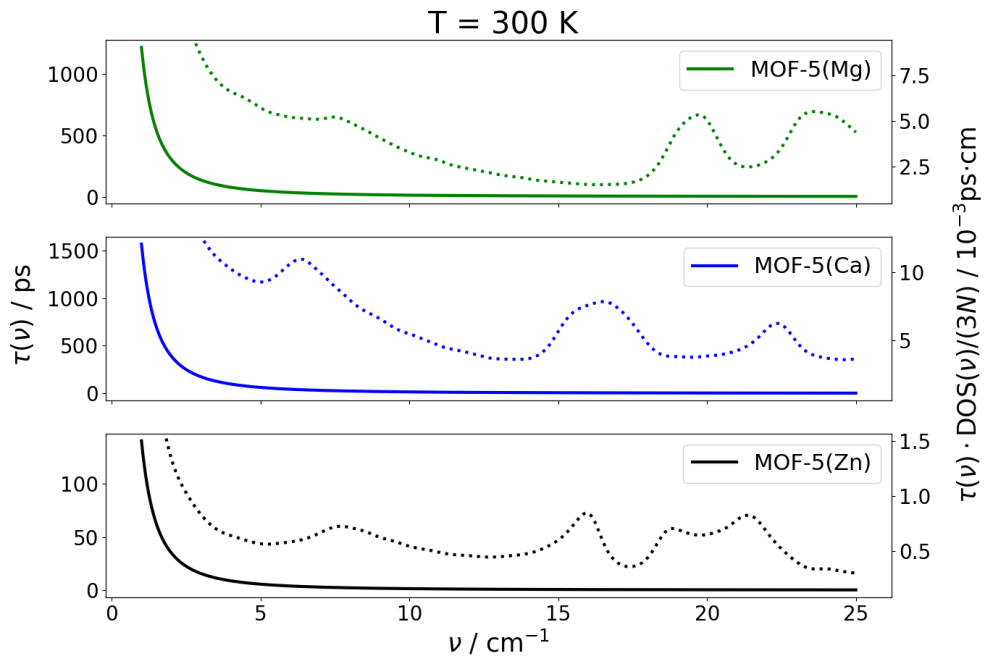
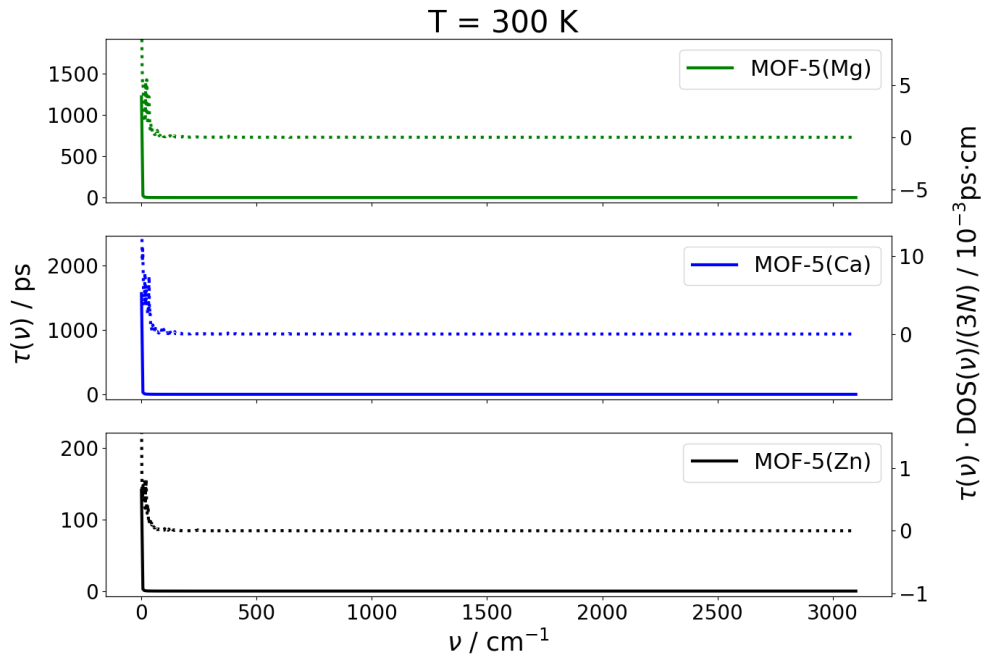


Fig. 5.29: Mode dependent phonon lifetimes (τ) multiplied with the density of states (DOS) of MOF-5 with different metallic nodes in (a) full and (b) the low-frequency (ν) range at 300 K.

5. Results and discussion

Another kind of analysis that especially makes sense when one considers different atoms, but the same geometries - i.e. linkers - is to evaluate the projected phonon density of states (PDOS). By making use of a PDOS analysis one can assign the degree of participation of certain atoms in each part of the density of states. Since a separate PDOS for every atom in the considered systems (106 atoms in the primitive unit cell) would be rather unclear, the PDOS is calculated for atoms of the same species which are in chemically inequivalent positions, though. The (arbitrary) labelling of the inequivalent atoms can be seen in figure 5.30.

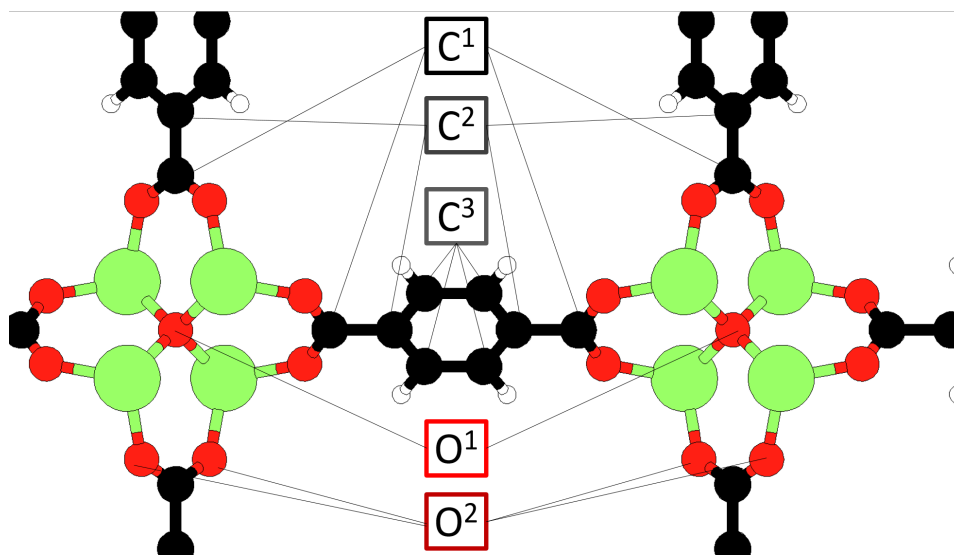


Fig. 5.30: Indication of how atoms that are in chemically inequivalent positions in the MOF-5 geometries are labelled in the projected density of states plots in fig. 5.31, 5.32, and 5.33.

All the hydrogen and metal (Mg, Ca or Zn) atoms in the cell are equivalent, whereas for oxygen and carbon there are different chemical environments, as can be seen in the sketch above. In the case of oxygen, there is one atom in the middle of the metallic nodes participating in the structure of all four metal-oxygen tetrahedra, while all the others are acting as the connection between the metal atoms and the organic linkers. For the carbon species one can even find three different chemical environments depending on the position within the linker.

The general definition of the phonon PDOS according to [61] contains the squared absolute value of the projection of the complex eigenvectors \mathbf{e}_n (corresponding to a certain eigenmode ω_n) onto a unit vector, representing the direction along which the projection is accomplished. Here, no distinction will be made between different directions of the oscillations, but rather between the participation of certain atoms in order to see, which of the atoms are the most important ones for the thermal transport properties. Therefore, the PDOS for an atom j , as it is used here, will be defined as the sum of the general PDOS expression over the cartesian directions x , y , z . This can be mathematically

expressed by equation (5.10). In this relation the summation is to be performed over all the bands indices n and \mathbf{q} points in the first Brillouin zone, which label the eigenfrequencies $\omega_{n,\mathbf{q}}$ and orthonormal eigenvectors $\mathbf{e}_{n,\mathbf{q}}$ ⁹. The summation over n, \mathbf{q} means to sum over every band and wavevector. Therefore, all occurring phonon modes sampled on a discrete mesh in the first Brillouin zone are considered. Note that by the variables $\mathbf{e}_{n,\mathbf{q},i}^j$ with $i = x, y, z$ it is meant that only those three components of the full eigenvector (of length $3N$) are considered that correspond to the atom labelled as j .

$$\text{PDOS}^j(\omega) = \sum_{n,\mathbf{q}} \delta(\omega - \omega_{n,\mathbf{q}}) \left(|\mathbf{e}_{n,\mathbf{q},x}^j|^2 + |\mathbf{e}_{n,\mathbf{q},y}^j|^2 + |\mathbf{e}_{n,\mathbf{q},z}^j|^2 \right) \quad (5.10)$$

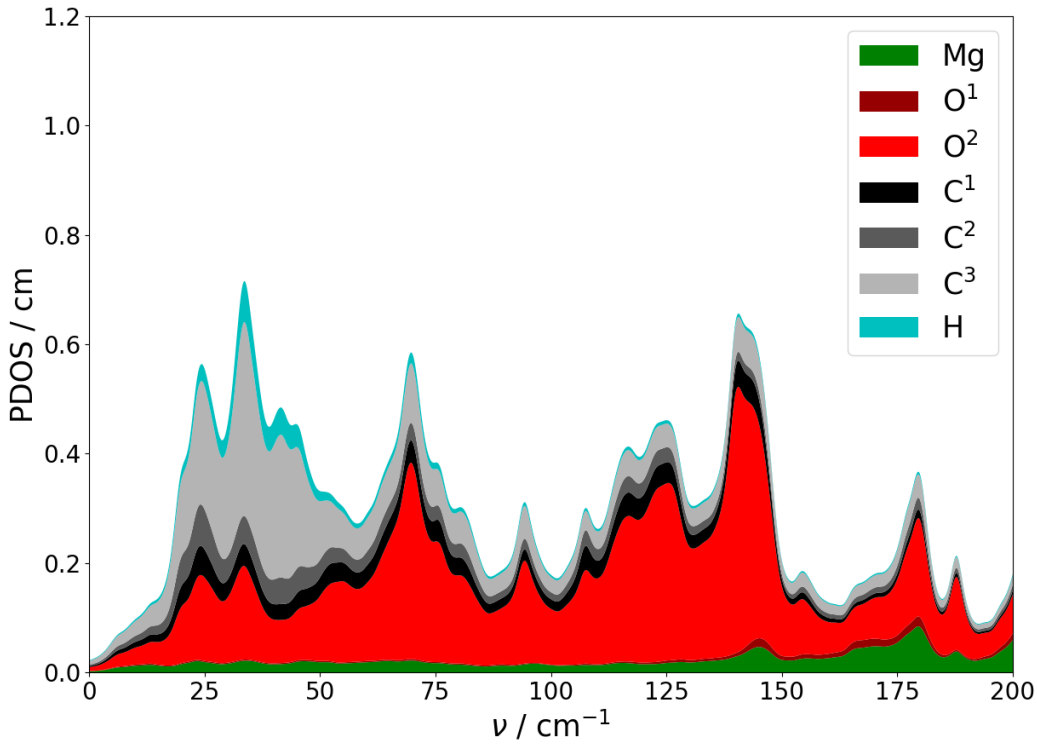


Fig. 5.31: Projected density of states (PDOS) for MOF-5(Mg). The PDOS is normalized in such a way that the integration over the wavenumber ν gives three times the number of the respective atoms. The labelling of the chemically inequivalent atoms can be found in fig. 5.30. A broadening has been introduced by means of eq. (5.2) with $\sigma = 2 \text{ cm}^{-1}$.

Like it was done at several points earlier, the delta distribution of equation (5.10) is replaced by a Lorentzian function (see eq. (5.2)) with a broadening parameter $\sigma = 2 \text{ cm}^{-1}$

⁹The eigenvectors of the dynamical matrix have to be multiplied with the square roots of the respective atomic masses in order to obtain the real space displacements.

5. Results and discussion

to account for finite linewidths, or similar deviations from the perfect situation. In contrast to previously applied broadening, which was consistently chosen with $\sigma = 0.5 \text{ cm}^{-1}$, a higher width was used in the analysis of the PDOS because a larger region of the spectrum is considered.

The PDOS for MOF-5(Mg), MOF-5(Ca), and MOF-5(Zn) can be found in figures 5.31, 5.32, and 5.33. As before, the normalisation of the DOS is defined in such a way that the integration should yield three times the total number of atoms in the system. Similarly, by using equation (5.10) it is assured that the integration of a particular PDOS, corresponding to N_a atoms, yields $3N_a$. Note that the PDOS contributions are displayed in a stacked way so that the outermost contour can be directly interpreted as the total phonon DOS.

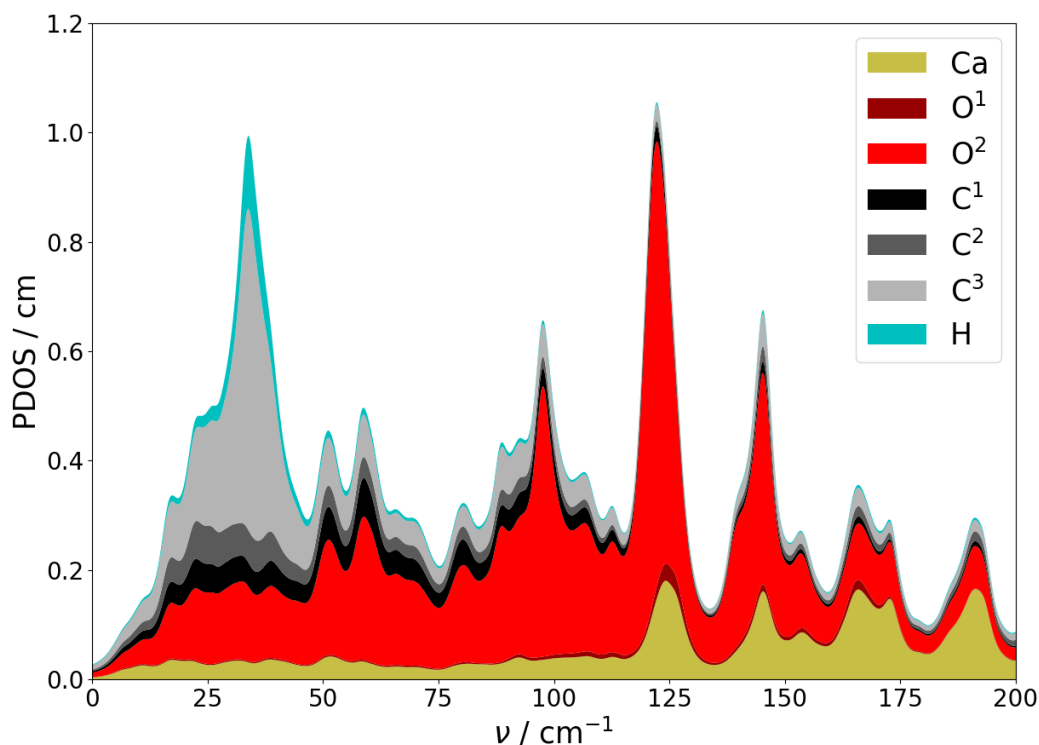


Fig. 5.32: Projected density of states (PDOS) for MOF-5(Mg). The PDOS is normalized in such a way that the integration over the wavenumber ν gives three times the number of the respective atoms. The labelling of the chemically inequivalent atoms can be found in fig. 5.30. A broadening has been introduced by means of eq. (5.2) with $\sigma = 2 \text{ cm}^{-1}$.

It is obvious that in the case of MOF-5(Mg) especially the oxygen atoms O^2 participate in all the shown modes up to about 150 cm^{-1} at a high percentage. The central

oxygen, however, appears to be rather reluctant to movement at all. There are only tiny contributions coming from O^1 at about 140 cm^{-1} and slightly above. This means that this atom does not contribute to the thermal transport properties, which were found to be significant only up to a frequency of 25 cm^{-1} for 300 K, at all. Its purpose is only that of a structural element stabilising the metallic nodes. This trend can be observed also for MOF-5(Ca) and MOF-5(Zn).

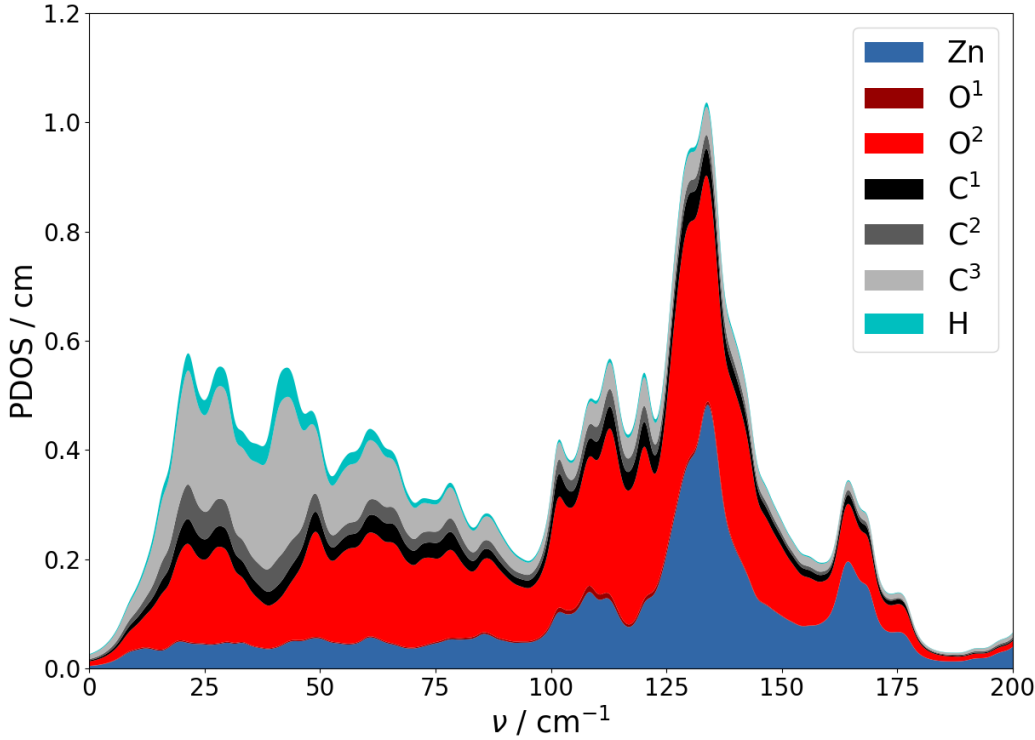


Fig. 5.33: Projected density of states (PDOS) for MOF-5(Mg). The PDOS is normalized in such a way that the integration over the wavenumber ν gives three times the number of the respective atoms. The labelling of the chemically inequivalent atoms can be found in fig. 5.30. A broadening has been introduced by means of eq. (5.2) with $\sigma = 2 \text{ cm}^{-1}$.

Furthermore, one can learn from the PDOS that the different metal atoms participate in the low-frequency modes to a varying extent. While Mg seems to contribute to phonon modes only negligibly in the displayed frequency range, there is a larger overlap of the Ca parts of the eigenvectors and even larger ones for Zn. There is obviously a tendency that the heavier the metal atom is, the larger are its projected contributions to low-frequency modes. This observation fits well to the simple picture of the one-dimensional chain with different masses. With heavier atoms being involved, the phonon modes tend to be more localised. This usually goes hand in hand with an increase in the relative amplitude of

the heavier atoms compared to the lighter ones. This means, when the mass of the heavier atom is increased, the vibrations become more localised - i.e. only certain parts of the chains move. The low-frequency modes typically correspond to vibrations, in which the heavier atoms move with larger amplitudes than the lighter ones. For heavier metals in MOF-5, the modes become more localised and the amplitudes of the heavier atoms increase, resulting in larger components in the eigenvectors and, therefore, higher contributions to the PDOS (at lower frequencies).

Another observations one can make by comparing the contributions from the different species for each MOF is that the relative participation of the carbon atoms is usually the highest at low frequencies, up to 100 cm^{-1} . For higher frequencies the relative contributions from the carbon atoms decrease and oxygen related modes with increasing involvement of the metals seem to dominate. Noticing that the high participation of carbon atoms can be mostly attributed to movement of the C^3 atoms and that exactly for those modes there is a non-vanishing involvement of the hydrogen atoms, it is clear that the linker constitution and configuration is crucial for this part of the DOS. Therefore, it clearly makes sense to vary the linker molecules in order to achieve different thermal transport properties.

The hydrogen contributions start to be significant only at considerably higher frequencies, what renders this species as well rather unimportant for thermal transport.

In summary, the analysis of the results from the variation of the metallic nodes revealed the following tendencies. First, using metals with higher atomic mass does not necessarily bring about an increase in volume of the unit cell, since for MOF-5(Ca) a larger lattice parameter a than MOF-5(Zn) was obtained. This could sometimes be useful to remember if one needs MOF geometries that are more open and provide more cavity space, without changing, for example, the thermal transport properties too much. Second, a correlation between the atomic mass of the metals in the nodes and the thermal conductivity was found as one would qualitatively expect. The thermal conductivity decreases with increasing mass, mainly due to a flattening of the phonon bands and, therefore, decreasing group velocities. However, no straightforward quantitative relationship can be observed. It turns out that especially deep minima in the bands - like that one at the high symmetry point W in the band structure of MOF-5(Mg) - are beneficial for thermal transport in two ways: such band minima can show increased phonon lifetimes if they are deep enough. This usually goes hand in hand with higher group velocities along the path towards the minimum. This was found to be the main reason for the higher thermal conductivity of MOF-5(Mg) compared to MOF-5(Ca) because the gradients of the bands are greater.

It could be shown that the presence of heavier atoms can lead to changes in the band structures, which results in decreased group velocities and a larger degree of anharmonicity. The mean squared Grüneisen parameters (MSGP) of MOF-5(Zn) was significantly greater than those of the other two systems (cf. fig. 5.19 and tab. 5.3). From the calculation of the MSGP it emerged that by introducing Ca as metal in the MOF-5 geometry, the harmonic approximation is restored to some extent compared to MOF-5(Mg). As a result, the phonon lifetimes of MOF-5(Ca) are higher. At temperatures higher than ap-

proximately 100 K, the longer lifetimes are compensated, however, by the slightly smaller group velocities of MOF-5(Ca). Therefore, for temperatures $T > 50$ K MOF-5(Mg) has the highest thermal conductivity. For lower temperatures, the low-frequency modes become increasingly relevant because the heat capacity function gets narrower with higher temperatures, favouring low-frequency phonons. The acoustic bands, which usually have the smallest frequencies, show comparable group velocities between MOF-5(Mg) and MOF-5(Ca). Additionally, the phonon lifetimes, which are larger in MOF-5(Ca) than in MOF-5(Mg), increase with decreasing temperature, compensating the vanishing difference in group velocities between the two systems at those temperatures. Therefore, the thermal conductivity in MOF-5(Ca) exceeds that of MOF-5(Mg) at low temperatures. It would be interesting to study the influence of the metal mass, separated from other influences. This could be achieved by studying hypothetical systems, containing (unrealistic) isotopes of the respective metal atoms.

By analysing the projected density of states (PDOS) of the systems, it was shown that the metal atoms participate in the low-frequency modes to different extents. The found tendency is that the heavier the metal is, the greater are the respective eigenvector components for lower vibrational energies. A further observation is that a significant amount of the DOS can be attributed to oscillations, in which the oxygen atoms connecting the linkers to the nodes are involved, whereas the central oxygen atom contributes to a negligible extent. Therefore, it would be interesting to study also the influence of those atoms in particular by attempting to (partly) replace them with other species like sulphur, if possible. The carbon contribution to the PDOS is noticeably present in the low-frequency region, resulting from oscillations that are low in vibrational energy. Therefore, if one tries to tailor the thermal transport properties of a MOF, it is crucial to consider both main constituents, the linkers and the nodes, with the linker being expected to usually have a larger impact.

5.4. Concluding remarks

Aside from the analysis of the results obtained with the presented methods and models, there remain some technical issues that have to be discussed at this point. The biggest source of inaccuracy is supposed to be the phonon lifetimes according to the model introduced in section 3.3. The main concern about the model of Bjerg et al. is that it was not designed for organic or metal-organic systems. Especially critical is the question, whether the empiric expression of the phonon lifetimes according to equation (3.25) can be used straightforwardly for this class of materials. A more or less simple solution is to adapt the fit parameters α and β in that equation in order to reproduce measured results. The complication simply is that there are only few experimental results available yet. Wang et al. studied the thermal conductivity of another MOF (MOF-74) with anisotropic geometry used the "exact" way to determine the phonon lifetimes via the third order derivatives of the PES [25]. They observe a deviation from the $\tau_n^{-1} \propto \omega_n^2$ relation for low frequencies.

Furthermore, the way in which the phonon lifetimes are calculated from the Grüneisen parameters heavily relies on the Debye model and an empirically found relation for the

thermal conductivity in noble gas crystals. Moreover, a possible anisotropy of the system is not contained in the lifetime model. Some steps in the model would have to be adapted in order to be able to use it for anisotropic systems. One has to scrutinise the calculation of the mode Grüneisen parameters at first, which is performed after isotropic expansion or compression of the system volume. Furthermore, the prefactor in the lifetimes model depends on the mean squared Grüneisen parameter. This quantity can neither account for anisotropy. For cubic systems, such as those that were discussed in section 5.3.2 and 5.3.3, the insufficient treatment of anisotropy is not a problem. However, it would be interesting to study the change of the mode Grüneisen parameters with the (isotropic) expansion/compression of the system. Since this step is the computationally most expensive one of the whole calculation procedure to obtain the thermal conductivity, as it relies on three phonon calculations, this test could not be conducted. In principle, one can even verify the mean Grüneisen parameter $\gamma(T)$ experimentally. According to equation (5.11) (cf. [17, p. 242]) the Grüneisen parameter is related to the linear thermal expansion coefficient $\alpha(T)$ via the isochoric heat capacity $C_V(T)$, the bulk modulus B and the volume V . Therefore, the Grüneisen parameter can be evaluated in practice by measuring these properties that are usually experimentally accessible.

$$\alpha(T) = \frac{\gamma(T)C_V(T)}{3VB} \quad (5.11)$$

Obviously, there is room for improvement in the used phonon lifetimes model. Especially the Debye model is problematic for systems with numerous rather flat optical bands. In the Debye model, every band is supposed to have a linear dispersion relation, which is not the case here. Already in the original model this was accounted for to some extent by not using the Debye temperature as the temperature scaling factor Θ in equation (3.25), but rather scaling it with $N^{-1/3}$, with N being the number of atoms in the unit cell, although the correct derivation would require the Debye temperature Θ_D to be Θ . The introduction of the additional factor $N^{-1/3}$, which Bjerg et al. suggested, is mathematically equivalent to using a different value than 3 for β in equation (3.25) and rescaling p accordingly. The way which is used here to define Θ for our systems, as described in section 4.5, is somewhat different as the definition of the Debye temperature via equation (3.30) is used employing the second and zeroth momenta of the phonon DOS. However, the integral is truncated at the highest frequency an (longitudinal) acoustic band hits the boundary of the first Brillouin zone. This is actually in better agreement to the fundamental idea of the Debye model of linear dispersion relations for the bands. Up to now, the way how to obtain this truncation frequency (ν_{cut}), however, is not very sophisticated: the band structure is displayed and ν_{max} is read from the plot. The high symmetry point at which this frequency should be read out is problematic, because it changes with factors like the symmetries of the systems, the presence of avoided crossings etc. A better method one can think of would be to employ a routine to search for modes which fulfil two essential criteria: the same symmetry in the eigenvector as the acoustic bands emerging from Γ (considering the complex exponentials) and vanishing group velocities. The maximum frequency of the found modes should then be the truncation frequency ν_{cut} .

In order to test the reliability of the model to compute the phonon lifetimes, it is planned to employ molecular dynamics (MD) simulations. In those calculations, one can track the total energy of the system for each time step and determine the relaxation times from its autocorrelation function. The challenge is, however, to obtain this quantity for a \mathbf{q} point grid that is dense enough to be representative. In order to obtain the phonon lifetimes for a $10 \times 10 \times 10$ \mathbf{q} mesh in reciprocal space, one has to run a MD simulation with a $10 \times 10 \times 10$ supercell, which is computationally very expensive. It is planned to conduct simulations of that kind with DFTB+ using the same Slater-Koster files that were used to calculate the phonon etc. to assure comparability between the results. The results of the MD simulations should then be used to benchmark the model of Bjerg et al. and adapt it if necessary.

Before this method has been verified, the results should be seen in such a way that the general qualitative trends for the thermal conductivity for different systems are described, but the absolute values are most probably not very accurate yet. Experimental data as well as comparisons with different approaches like MD would be beneficial for this benchmarking. Huang et al. published two studies, one experimental and another employing MD calculations, where they investigated the thermal conductivity of MOF-5(Zn) [55, 56]. They report values for the thermal conductivity of about $0.3 \text{ Wm}^{-1}\text{K}^{-1}$, whereas the result presented here was about $0.03 \text{ Wm}^{-1}\text{K}^{-1}$ at 300 K. Their results are actually in better agreement with the ones obtained for MOF-5(Mg) and MOF-5(Ca). It has to be mentioned, however, that Huang et al. performed MD simulations for $1 \times 1 \times 1$, $2 \times 2 \times 2$, and $3 \times 3 \times 3$ super cells, amongst which the reported thermal conductivities still vary by about 10 %. Although their solution might not be converged yet with respect to the system size, it is very improbable that even the converged solution would be in agreement with the results presented here. Nevertheless, the tendency that the temperature dependence of the thermal conductivity is very weak, was also found by them (within certain uncertainties).

6. Summary

Metal-organic frameworks (MOFs) are crystalline systems with a nearly unlimited number of different constitutions and configurations. By varying the main constituents - the metallic nodes or the organic linkers connecting those - one can control their properties in a convenient manner. Due to the high porosity of MOFs, people came up with numerous applications exploiting the large amount of internal surface area in fields like catalysis, gas storage, and cooling. In most applications of MOFs, temperature gradients are present. So the question arises, how efficient (fast) heat can be transported through such materials. The origin of that heat can be exothermal reactions, the latent heat of adsorption and many others. Although the thermal transport aspect of the applications is one of the most crucial ones in practice, the fundamental relations and main influences on the thermal conductivity have been hardly investigated yet. It is, therefore, vital to study the thermal transport behaviour for this class of materials, which has gained a lot of scientific attention in recent years. The biggest potential of MOFs can be most probably attributed to the variety of possible structures using the tool box of organic chemistry. If one can understand what governs thermal transport in detail, one can make use of that knowledge and construct even anisotropic systems with the desired properties in specific directions.

Since both, the synthesis and the experimental evaluation of the thermal conductivity in MOFs can be rather expensive and challenging in practice, it is beneficial to predict the properties of certain structures based on simulation results. The approach that was chosen to model the thermal conductivity of MOFs is that of quasi-harmonic lattice dynamics. Therefore, the lattice vibrations (phonons) are considered as being the dominant thermal transport mechanism present in this kind of material. As a consequence, to understand thermal transport, the vibrational properties have to be investigated as a first step. From the Boltzmann transport equation within the relaxation time approximation, an expression for the thermal conductivity is derived by comparison to the classical law of Fourier. Most of the required quantities can be calculated from phonon band structure calculations. This was done with first-principle calculations based on density functional theory (DFT) and density functional tight binding (DFTB) within the harmonic approximation.

In order to be able to compare the results of the simulations to experimental data without having to measure the entire phonon band structure, powder Raman scattering spectra were calculated for some MOFs according to the method proposed by Porezag et al. [34]. The frequency shifts of phonon modes are rationalised by structural considerations of different linkers and nodes for various systems. By studying how and why certain vibrational modes change between different MOF geometries, one can understand the modified band structures and, therefore, estimate the expected changes in the thermal conductivity. The shifts of some Raman active peaks from one MOF to another can be understood by considerations based on classical properties of the constituents like atomic mass, bond angles and lengths etc.

However, it was found at a relatively early point that large supercell sizes are necessary to calculate the lattice vibration by means of the finite differences approach - sometimes

requiring 8000 atoms and more in the cells. This can be rationalised by looking at the pairwise interaction between the involved atoms in the system, which is modelled as a set of linear springs the atoms are connected by. In the finite differences method for calculating phonons, the Fourier transform of the force constants (the dynamical matrix) is calculated, whose eigenvalues are the squared phonon frequencies. If one considers too small supercells, one risks truncating the Fourier series too early, introducing artefacts in the calculations, which usually appear as negative or imaginary frequencies. The longer distances it takes to make the interatomic force constants decay, the larger supercells are needed for a converged solution. In all the studied cases, the systems are too big to be handled with the DFT based programme VASP [18, 19, 20]. This is where DFTB had to be employed, using the DFTB+ code [46].

As the DFT calculations can be compared to experimentally obtained Raman scattering spectra, it had to be made sure that also DFTB+ yields results with acceptable accuracy. A brief benchmark of the vibrational properties at the Brillouin zone centre Γ for MOF-5(Zn) and IRMOF-3(Zn) obtained with VASP and DFTB+ is presented. Besides a direct comparison of the phonon frequencies, where it is possible to reproduce the general tendencies and the envelope of the density of states (DOS) at Γ (cf. fig. 5.6), also an analysis evaluating the eigenvectors of the dynamical matrix was carried out. The purpose of comparing the overlap of the eigenvectors from different calculations is to test, whether the vibrational motion of the nodes could be reproduced. If one restricts oneself to the very low frequency region of up to 50 cm^{-1} , one can find that more than 50 % of the eigenvectors of VASP and DFTB+ have overlaps ≥ 0.9 . The eigenvectors characterised by their scalar products could be shown to be in not so perfect agreement for higher frequencies, with the most significant deviations being found at the carbon hydrogen valence stretch oscillations at about 3100 cm^{-1} . It is shown, however, that such high frequencies are completely irrelevant for thermal transport for several reasons. In conclusion, the benchmark shows that DFTB+ can be used without a too significant loss of accuracy as long as the relevant frequency range is low enough in vibrational energy. Since those low-frequency modes typically contribute more to the thermal conductivity, one can neglect the differences at very high frequencies.

Up to this point it has been discussed, how to obtain the harmonic phonon modes in a relatively cheap way and how to verify the results by comparing them with experiments or more accurate simulations. However, the question about the last missing quantity has been completely neglected yet, namely the phonon lifetimes. Since the procedure using the analytical expression usually is infeasible in terms of available resources, the model of Bjerg et al. [16] has been employed. The central part of this model is a relation for the phonon lifetimes in which the Grüneisen parameters enter, which can be seen as measures for the degree of anharmonicities present in the system. Using this model, which has been verified several times for inorganic crystals [16, 27], the thermal conductivity for some selected MOFs has been calculated.

As a first step to deduce structure-to-property relationships for the thermal transport behaviour of MOFs, a systematic concept to vary the constituents had to be introduced. MOF-5(Mg) is regarded as the reference structure based on which certain constituents are substituted. One can think of two possible directions: vary the metallic nodes or the

6. Summary

organic linkers. In order to study the influence of the metal atoms, Mg is replaced with Ca or Zn. The linkers are substituted by a larger aromatic molecule (IRMOF-14(Mg)) or by alkyne chains (IRMOF-131(Mg), IRMOF-132(Mg)) as displayed in figure 5.10. Summarising the results for the variation of the organic linkers, it could be found that the MOF-5 structure shows the highest thermal conductivity of all systems with different linkers (cf. fig. 5.11). The three essential quantities - the heat capacities, the group velocities, and the phonon lifetimes - were analysed in detail. The heat capacities, which are related to the temperature occupation factors, do not limit the mode contributions to the thermal conductivity at room temperature. The stronger constraint is exerted by the phonon lifetimes, which limit the relevant frequency region to a range from 0 to approximately 25 cm^{-1} . The alkyne linkers show much larger mean squared Grüneisen parameters (cf. eq. (3.28), fig. 5.19, tab. 5.3). Obviously, the degree of anharmonicity is much larger in the alkyne MOFs resulting in decreased phonon lifetimes. It could be seen that if two MOFs with similar linkers are compared, usually the system with the larger lattice constant shows increased group velocities, provided that not too many additional atoms are introduced. The overall temperature dependence of the thermal conductivity of IRMOF-14 was shown to be the weakest of the studied systems.

Regarding the variation of the metallic nodes, the results are in qualitative agreement with intuition. The higher the mass of the metal atoms, the lower the thermal conductivity. Although the group velocities are observed to be in the same range for Zn, Mg or Ca nodes, MOF-5(Zn) has a lower thermal conductivity than the other systems by about a factor of 10. The analysis shows that the reason for that can be found in very low phonon lifetimes having its origin in a significantly increased mean squared Grüneisen parameter of MOF-5(Zn). An interesting finding is that MOF-5(Ca) has higher phonon lifetimes than MOF-5(Mg). This increases the thermal conductivity of MOF-5(Ca) more rapidly for decreasing temperatures than for MOF-5(Mg). Therefore, at low temperatures MOF-5(Ca) has the highest thermal conductivity of the three systems. One can even go a step further and study the contributions of every species to the phonon DOS to see, which atoms are more important than others for the relevant oscillations. It turns out that for the low frequency modes, the carbon atoms of the linkers contribute the most to the projected DOS (PDOS). Therefore, it appears to be more important to vary the linkers than the metals in order to observe strong changes in the thermal conductivity. However, the low-frequency bands of the linker oscillations are typically relatively flat, which does not result in large thermal conductivity contributions. The relative participation of the metal in low-frequency vibration increases with increasing atomic mass.

It shall be stressed that the results are to be seen as qualitative tendencies, but not as quantitative ones. For these classes of materials the model for the phonon lifetimes still has to be verified using, for example, experimental data. In order to test the semi-empirical relations, the phonon lifetimes are planned to be compared to molecular dynamics simulations or to exact anharmonic lattice dynamics calculations.

References

- [1] Anne Boutin, David Bousquet, Aurélie U. Ortiz, François-Xavier Coudert, Alain H. Fuchs, Anthony Ballandras, Guy Weber, Igor Bezverkhyy, Jean-Pierre Bellat, Guillaume Ortiz, Gérald Chaplais, Jean-Louis Paillaud, Claire Marichal, Habiba Nouali, and Joël Patarin. Temperature-induced structural transitions in the gallium-based mil-53 metal–organic framework. *The Journal of Physical Chemistry C*, 117(16):8180–8188, 2013.
- [2] Hiroyasu Furukawa, Kyle E. Cordova, Michael O’Keeffe, and Omar M. Yaghi. The chemistry and applications of metal-organic frameworks. *Science*, 341(6149), 2013.
- [3] Andrew R. Millward and Omar M. Yaghi. Metal–organic frameworks with exceptionally high capacity for storage of carbon dioxide at room temperature. *Journal of the American Chemical Society*, 127(51):17998–17999, 2005. PMID: 16366539.
- [4] Hong-Cai Zhou, Jeffrey R. Long, and Omar M. Yaghi. Introduction to metal–organic frameworks. *Chemical Reviews*, 112(2):673–674, 2012. PMID: 22280456.
- [5] Michael Hirscher and Barbara Panella. Hydrogen storage in metal–organic frameworks. *Scripta Materialia*, 56(10):809 – 812, 2007. Viewpoint set no. 42 “Nanoscale materials for hydrogen storage”.
- [6] Hiroyasu Furukawa, Felipe Gándara, Yue-Biao Zhang, Juncong Jiang, Wendy L. Queen, Matthew R. Hudson, and Omar M. Yaghi. Water adsorption in porous metal–organic frameworks and related materials. *Journal of the American Chemical Society*, 136(11):4369–4381, 2014. PMID: 24588307.
- [7] Bin Li, Hui-Min Wen, Wei Zhou, Jeff Q. Xu, and Banglin Chen. Porous metal-organic frameworks: Promising materials for methane storage. *Chem*, 1(4):557 – 580, 2016.
- [8] Martijn F. de Lange, Karlijn J. F. M. Verouden, Thijs J. H. Vlugt, Jorge Gascon, and Freek Kapteijn. Adsorption-driven heat pumps: The potential of metal–organic frameworks. *Chemical Reviews*, 115(22):12205–12250, 2015. PMID: 26492978.
- [9] Martijn F. de Lange, Benjamin L. van Velzen, Coen P. Ottevanger, Karlijn J. F. M. Verouden, Li-Chiang Lin, Thijs J. H. Vlugt, Jorge Gascon, and Freek Kapteijn. Metal–organic frameworks in adsorption-driven heat pumps: The potential of alcohols as working fluids. *Langmuir*, 31(46):12783–12796, 2015. PMID: 26523608.
- [10] Ahmed Rezk, Raya Al-Dadah, Saad Mahmoud, and Ahmed Elsayed. Characterisation of metal organic frameworks for adsorption cooling. *International Journal of Heat and Mass Transfer*, 55(25):7366 – 7374, 2012.
- [11] Daiane Damasceno Borges, Guillaume Maurin, and Douglas Galvao. Design of porous metal-organic frameworks for adsorption driven thermal batteries. 01 2017.

References

- [12] JeongYong Lee, Omar K. Farha, John Roberts, Karl A. Scheidt, SonBinh T. Nguyen, and Joseph T. Hupp. Metal-organic framework materials as catalysts. *Chem. Soc. Rev.*, 38:1450–1459, 2009.
- [13] Lauren E. Kreno, Kirsty Leong, Omar K. Farha, Mark Allendorf, Richard P. Van Duyne, and Joseph T. Hupp. Metal–organic framework materials as chemical sensors. *Chemical Reviews*, 112(2):1105–1125, 2012. PMID: 22070233.
- [14] H. Ibach and H. Lüth. *Festkörperphysik: Einführung in die Grundlagen*. Springer-Lehrbuch. Springer Berlin Heidelberg, 2009.
- [15] Glen A. Slack. The thermal conductivity of nonmetallic crystals. volume 34 of *Solid State Physics*, pages 1 – 71. Academic Press, 1979.
- [16] Lasse Bjerg, Bo B. Iversen, and Georg K. H. Madsen. Modeling the thermal conductivities of the zinc antimonides ZnSb and Zn₄Sb₃. *Phys. Rev. B*, 89:024304, Jan 2014.
- [17] R. Gross and A. Marx. *Festkörperphysik*. Oldenbourg Wissenschaftsverlag, 2012.
- [18] G. Kresse and J. Hafner. Ab initio molecular dynamics for liquid metals. *Phys. Rev. B*, 47:558–561, Jan 1993.
- [19] G. Kresse and J. Furthmüller. Efficiency of ab-initio total energy calculations for metals and semiconductors using a plane-wave basis set. *Computational Materials Science*, 6(1):15 – 50, 1996.
- [20] G. Kresse and J. Furthmüller. Efficient iterative schemes for ab initio total-energy calculations using a plane-wave basis set. *Phys. Rev. B*, 54:11169–11186, Oct 1996.
- [21] Paolo Giannozzi, Stefano Baroni, Nicola Bonini, Matteo Calandra, Roberto Car, Carlo Cavazzoni, Davide Ceresoli, Guido L Chiarotti, Matteo Cococcioni, Ismaila Dabo, Andrea Dal Corso, Stefano de Gironcoli, Stefano Fabris, Guido Fratesi, Ralph Gebauer, Uwe Gerstmann, Christos Gougoussis, Anton Kokalj, Michele Lazzeri, Layla Martin-Samos, Nicola Marzari, Francesco Mauri, Riccardo Mazzarello, Stefano Paolini, Alfredo Pasquarello, Lorenzo Paulatto, Carlo Sbraccia, Sandro Scandolo, Gabriele Sclauzero, Ari P Seitsonen, Alexander Smogunov, Paolo Umari, and Renata M Wentzcovitch. Quantum espresso: a modular and open-source software project for quantum simulations of materials. *Journal of Physics: Condensed Matter*, 21(39):395502 (19pp), 2009.
- [22] P Giannozzi, O Andreussi, T Brumme, O Bunau, M Buongiorno Nardelli, M Calandra, R Car, C Cavazzoni, D Ceresoli, M Cococcioni, N Colonna, I Carnimeo, A Dal Corso, S de Gironcoli, P Delugas, R A DiStasio Jr, A Ferretti, A Floris, G Fratesi, G Fugallo, R Gebauer, U Gerstmann, F Giustino, T Gorni, J Jia, M Kawamura, H-Y Ko, A Kokalj, E Küçükbenli, M Lazzeri, M Marsili, N Marzari, F Mauri, N L Nguyen, H-V Nguyen, A Otero de-la Roza, L Paulatto, S Poncé, D Rocca,

- R Sabatini, B Santra, M Schlipf, A P Seitsonen, A Smogunov, I Timrov, T Thonhauser, P Umari, N Vast, X Wu, and S Baroni. Advanced capabilities for materials modelling with quantum espresso. *Journal of Physics: Condensed Matter*, 29(46):465901, 2017.
- [23] J. E. Turney, E. S. Landry, A. J. H. McGaughey, and C. H. Amon. Predicting phonon properties and thermal conductivity from anharmonic lattice dynamics calculations and molecular dynamics simulations. *Phys. Rev. B*, 79:064301, Feb 2009.
- [24] Laurent Chaput, Atsushi Togo, Isao Tanaka, and Gilles Hug. Phonon-phonon interactions in transition metals. *Phys. Rev. B*, 84:094302, Sep 2011.
- [25] Xinjiang Wang, Ruiqiang Guo, Dongyan Xu, JaeDong Chung, Massoud Kaviani, and Baoling Huang. Anisotropic lattice thermal conductivity and suppressed acoustic phonons in mof-74 from first principles. *The Journal of Physical Chemistry C*, 119(46):26000–26008, 2015.
- [26] Glen A. Slack and S. Galginaitis. Thermal conductivity and phonon scattering by magnetic impurities in cdte. *Phys. Rev.*, 133:A253–A268, Jan 1964.
- [27] Madsen Georg K. H., Katre Ankita, and Bera Chandan. Calculating the thermal conductivity of the silicon clathrates using the quasi-harmonic approximation. *physica status solidi (a)*, 213(3):802–807.
- [28] Robert G. Parr. Density functional theory. *Ann. Rev. Phys. Chem.*, 34:631–656, 1983.
- [29] R. O. Jones. Density functional theory: Its origins, rise to prominence, and future. *Rev. Mod. Phys.*, 87:897–923, Aug 2015.
- [30] P. Hohenberg and W. Kohn. Inhomogeneous electron gas. *Phys. Rev.*, 136:B864–B871, Nov 1964.
- [31] W. Kohn and L. J. Sham. Self-consistent equations including exchange and correlation effects. *Phys. Rev.*, 140:A1133–A1138, Nov 1965.
- [32] John P. Perdew, Kieron Burke, and Matthias Ernzerhof. Generalized gradient approximation made simple. *Phys. Rev. Lett.*, 77:3865–3868, Oct 1996.
- [33] P. E. Blöchl. Projector augmented-wave method. *Phys. Rev. B*, 50:17953–17979, Dec 1994.
- [34] Dirk Porezag and Mark R. Pederson. Infrared intensities and raman-scattering activities within density-functional theory. *Phys. Rev. B*, 54:7830–7836, Sep 1996.
- [35] Augusto F. Oliveira, Gotthard Seifert, Thomas Heine, and Hélio A. Duarte. Density-functional based tight-binding: an approximate DFT method. *Journal of the Brazilian Chemical Society*, 20:1193 – 1205, 00 2009.

- [36] G. Seifert. Tight-binding density functional theory: an approximate kohn–sham dft scheme. *The Journal of Physical Chemistry A*, 111(26):5609–5613, 2007. PMID: 17439198.
- [37] David Dubbeldam, Patrick Fuller, Castillo Sanches, Tina Düren, and Takuji Nishimura. Raspa2. <https://github.com/numat/RASPA2/tree/master/structures/mofs/cif>, 2015.
- [38] Mohamed Eddaoudi, Jaheon Kim, Nathaniel Rosi, David Vodak, Joseph Wachter, Michael O’Keeffe, and Omar M Yaghi. Systematic design of pore size and functionality in isorecticular mofs and their application in methane storage. 295:469–72, 02 2002.
- [39] G. Kresse and D. Joubert. From ultrasoft pseudopotentials to the projector augmented-wave method. *Phys. Rev. B*, 59:1758–1775, Jan 1999.
- [40] Alexandre Tkatchenko, Robert A. DiStasio, Roberto Car, and Matthias Scheffler. Accurate and efficient method for many-body van der waals interactions. *Phys. Rev. Lett.*, 108:236402, Jun 2012.
- [41] Ariel Lozano, Bruno Escribano, Elena Akhmatkaya, and Javier Carrasco. Assessment of van der waals inclusive density functional theory methods for layered electroactive materials. *Phys. Chem. Chem. Phys.*, 19:10133–10139, 2017.
- [42] Bess Vlasisavljevich, Johanna Huck, Zeric Hulvey, Kyuho Lee, Jarad A. Mason, Jeffrey B. Neaton, Jeffrey R. Long, Craig M. Brown, Dario Alfè, Angelos Michaelides, and Berend Smit. Performance of van der waals corrected functionals for guest adsorption in the m2(dobdc) metal–organic frameworks. *The Journal of Physical Chemistry A*, 121(21):4139–4151, 2017. PMID: 28436661.
- [43] Rafael L. H. Freire, Diego Guedes-Sobrinho, Adam Kiejna, and Juarez L. F. Da Silva. Comparison of the performance of van der waals dispersion functionals in the description of water and ethanol on transition metal surfaces. *The Journal of Physical Chemistry C*, 122(3):1577–1588, 2018.
- [44] Tomás Bucko, J Hafner, and János Ángyán. Geometry optimization of periodic systems using internal coordinates. *The Journal of chemical physics*, 122:124508, 04 2005.
- [45] A. Fonari and S. Stauffer. vasp_raman.py. <https://github.com/raman-sc/VASP/>, 2013.
- [46] B. Aradi, B. Hourahine, and Th. Frauenheim. Dftb+, a sparse matrix-based implementation of the dftb method. *The Journal of Physical Chemistry A*, 111(26):5678–5684, 2007. PMID: 17567110.

- [47] Ney H. Moreira, Grygoriy Dolgonos, Bálint Aradi, Andreia L. da Rosa, and Thomas Frauenheim. Toward an accurate density-functional tight-binding description of zinc-containing compounds. *Journal of Chemical Theory and Computation*, 5(3):605–614, 2009. PMID: 26610226.
- [48] Michael Gaus, Albrecht Goez, and Marcus Elstner. Parametrization and benchmark of dftb3 for organic molecules. *Journal of Chemical Theory and Computation*, 9(1):338–354, 2013. PMID: 26589037.
- [49] Maximilian Kubillus, Tomáš Kubař, Michael Gaus, Jan Řezáč, and Marcus Elstner. Parameterization of the dftb3 method for br, ca, cl, f, i, k, and na in organic and biological systems. *Journal of Chemical Theory and Computation*, 11(1):332–342, 2015.
- [50] Xiya Lu, Michael Gaus, Marcus Elstner, and Qiang Cui. Parametrization of dftb3/3ob for magnesium and zinc for chemical and biological applications. *The Journal of Physical Chemistry B*, 119(3):1062–1082, 2015. PMID: 25178644.
- [51] Michael Gaus, Albrecht Goez, and Marcus Elstner. Parametrization and benchmark of dftb3 for organic molecules. *Journal of Chemical Theory and Computation*, 9(1):338–354, 2013. PMID: 26589037.
- [52] W. von der Linden, V. Dose, and U. von Toussaint. *Bayesian Probability Theory: Applications in the Physical Sciences*. Bayesian Probability Theory: Applications in the Physical Sciences. Cambridge University Press, 2014.
- [53] A Togo and I Tanaka. First principles phonon calculations in materials science. *Scr. Mater.*, 108:1–5, Nov 2015.
- [54] Donald T. Morelli and Glen A. Slack. *High Lattice Thermal Conductivity Solids*, pages 37–68. Springer New York, New York, NY, 2006.
- [55] B.L. Huang, A.J.H. McGaughey, and M. Kaviani. Thermal conductivity of metal-organic framework 5 (mof-5): Part i. molecular dynamics simulations. *International Journal of Heat and Mass Transfer*, 50(3):393 – 404, 2007.
- [56] B.L. Huang, Z. Ni, A. Millward, A.J.H. McGaughey, C. Uher, M. Kaviani, and O. Yaghi. Thermal conductivity of a metal-organic framework (mof-5): Part ii. measurement. *International Journal of Heat and Mass Transfer*, 50(3):405 – 411, 2007.
- [57] Razvan Caracas. Raman spectra and lattice dynamics of cubic gauche nitrogen. *The Journal of Chemical Physics*, 127(14):144510, 2007.
- [58] H. Kuzmany. *Festkörperspektroskopie: eine Einführung*. Springer, 1990.

- [59] M. J. Frisch, G. W. Trucks, H. B. Schlegel, G. E. Scuseria, M. A. Robb, J. R. Cheeseman, G. Scalmani, V. Barone, B. Mennucci, G. A. Petersson, H. Nakatsuji, M. Caricato, X. Li, H. P. Hratchian, A. F. Izmaylov, J. Bloino, G. Zheng, J. L. Sonnenberg, M. Hada, M. Ehara, K. Toyota, R. Fukuda, J. Hasegawa, M. Ishida, T. Nakajima, Y. Honda, O. Kitao, H. Nakai, T. Vreven, J. A. Montgomery, Jr., J. E. Peralta, F. Ogliaro, M. Bearpark, J. J. Heyd, E. Brothers, K. N. Kudin, V. N. Staroverov, R. Kobayashi, J. Normand, K. Raghavachari, A. Rendell, J. C. Burant, S. S. Iyengar, J. Tomasi, M. Cossi, N. Rega, J. M. Millam, M. Klene, J. E. Knox, J. B. Cross, V. Bakken, C. Adamo, J. Jaramillo, R. Gomperts, R. E. Stratmann, O. Yazyev, A. J. Austin, R. Cammi, C. Pomelli, J. W. Ochterski, R. L. Martin, K. Morokuma, V. G. Zakrzewski, G. A. Voth, P. Salvador, J. J. Dannenberg, S. Dapprich, A. D. Daniels, Ö. Farkas, J. B. Foresman, J. V. Ortiz, J. Cioslowski, and D. J. Fox. Gaussian~09 Revision D.01. Gaussian Inc. Wallingford CT 2009.
- [60] IUPAC. Periodic table of the elements. <https://iupac.org/what-we-do/periodic-table-of-elements/>, July 2018.
- [61] Atsushi Togo. Phonopy setting tags. <https://atztogo.github.io/phonopy/setting-tags.html#dos-related-tags>, 2018.
- [62] Wahyu Setyawan and Stefano Curtarolo. High-throughput electronic band structure calculations: Challenges and tools. *Computational Materials Science*, 49(2):299 – 312, 2010.
- [63] W. Nolting. *Grundkurs Theoretische Physik 6: Statistische Physik*. Springer-Lehrbuch. Springer Berlin Heidelberg, 2013.
- [64] Yang, Haibo Yu, Darrin York, Qiang Cui, and Marcus Elstner. Extension of the self-consistent-charge density-functional tight-binding method: third-order expansion of the density functional theory total energy and introduction of a modified effective coulomb interaction. *The Journal of Physical Chemistry A*, 111(42):10861–10873, 2007. PMID: 17914769.

List of Figures

1.1.	Phonon band structure of a linear one-dimensional chain of two atoms with different masses m_1 and m_2 in a primitive unit cell of length a . The optical and acoustic bands are plotted for different mass ratios m_2/m_1 . $\omega \dots$ phonon frequency, $q \dots$ phonon wave vector.	2
1.2.	Number of publications listed by Web of Science that have "MOF" or "metal-organic framework" as their topic. Evaluated at 2 July 2018, 7 pm.	3
2.1.	Some exemplaric MOF structures forming cavities with (a) simple cubic and (b) simple tetragonal Bravais lattice.	5
2.2.	Some exemplaric MOF structures forming channels trough the crystal.	6
3.1.	Heat capacities according to eq. (3.10) for (a) the general univariate function compared to the Bose-Einstein distribution f_{BE} and (b) for different temperatures T as parameter over a frequency range ν . Mind that the curves for different temperatures correspond to a rescaling of the abscissa in (a).	11
3.2.	Lennard-Jones potential plotted as a function of the distance in comparison with its harmonic approximation around the minimum.	16
3.3.	Computational time scaling behaviour for single point calculations of different super cells of MOF-508 with VASP (EDIFF = 1E-8, ALGO = Fast, PREC = Accurate). The Brillouin zone sampling has been adapted to the supercell sizes.	23
3.4.	Flow chart of the self-consistent charge approach in DFTB.	25
4.1.	Flow chart of the general steps in order to calculate the thermal conductivity tensor. The code packages used are assigned to certain steps.	27
5.1.	Raman spectra for some IRMOFs calculated with the Raman-VASP implementation according to [45]. The data were broadened with a broadening parameter $\sigma = 0.5 \text{ cm}^{-1}$ according to eq. (5.2). Colouring scheme: red...oxygen, black...carbon, blue...nitrogen, white...hydrogen, grey...zinc.	39
5.2.	Raman spectra for MOF-508 and PMOF-508 calculated with the Raman-VASP implementation according to [45]. The data were broadened with a broadening parameter $\sigma = 0.5 \text{ cm}^{-1}$ according to eq. (5.2). Colouring scheme: red...oxygen, black...carbon, blue...nitrogen, white...hydrogen, grey...zinc	42
5.3.	Schematic displacement pattern for two similar oscillations (side view). The envelopes of the movements are only drawn between two neighbouring metallic nodes. Colouring scheme: red...oxygen, black...carbon, blue...nitrogen, white...hydrogen, grey...zinc	43
5.4.	Top view and dihedral angles of MOF-508 and PMOF-508. Colouring scheme: red...oxygen, black...carbon, blue...nitrogen, white...hydrogen, grey...zinc	44

5.5.	Raman spectra of the linker molecules of MOF-508 calculated with Gaussian09 [59]. PCB...Terephthalic acid (para dicarboxybenzene), 44BP...4,4'-bipyridine. The data were broadened with a broadening parameter $\sigma = 0.5 \text{ cm}^{-1}$ according to eq. (5.2)	45
5.6.	Phonon frequencies (ν) at the Brillouin zone center Γ calculated with VASP and DFTB+ for (a) MOF-5(Zn) and (b) IRMOF-3(Zn). The frequency spectra was broadened with a Lorentzian according to eq. (5.2) with a broadening parameter $\sigma = 2 \text{ cm}^{-1}$ to obtain a density D at Γ . . .	49
5.7.	Histograms of the dot product between phonon eigenvectors of (a),(b) MOF-5(Zn) and (c),(d) IRMOF-3(Zn) calculated with VASP and the eigenvectors calculated with DFTB+. In (a) and (c) all modes are considered, in (b) and (d) only low-frequency modes with a frequency up to 200 cm^{-1} are taken into account.	50
5.8.	Thermal conductivity (κ) over different \mathbf{q} point meshes for three temperatures of MOF-5(Mg).	52
5.9.	Structural formulae of the unreacted linker molecules used in the studied IRMOFs.	53
5.10.	Three-dimensional views of MOFs which differ only in the organic linkers, but not in the metallic nodes. The influences of the linkers on the thermal conductivity is discussed based on those four systems. Colouring scheme: red...oxygen, green...magnesium, black...carbon, white...hydrogen	54
5.11.	Calculated thermal conductivity (κ) as a function of temperature (T) of some IRMOFs with different organic linkers.	56
5.12.	Phonon band structure of the studied systems with aromatic linkers. All the systems have a face-centred cubic Bravais lattice. The bands are coloured in a logarithmic scale showing the contribution to the thermal conductivity κ per \mathbf{q} point and mode.	57
5.13.	Phonon band structure of some of the studied systems with alkyne linkers. All the systems have a face-centred cubic Bravais lattice. The bands are coloured in a logarithmic scale showing the contribution to the thermal conductivity κ per \mathbf{q} point and mode.	58
5.14.	Density of states (DOS) of selected IRMOFs with different organic linkers in (a) full and (b) the low-frequency (ν) range. The cumulative integrals are plotted as dotted lines on the secondary ordinates.	59
5.15.	Mode contributions to the thermal conductivity (κ_{xx}) (solid lines, left ordinate) and their products with the density of states (DOS) (dotted lines, right ordinate) of selected IRMOFs with different organic linkers in low-frequency (ν) range at 300 K.	60
5.16.	Mode contributions to the thermal conductivity (κ) multiplied with the density of states (DOS) of selected IRMOFs with different organic linkers in (a) full and (b) the low-frequency (ν) range at 300 K. The cumulative integrals are plotted as dotted lines on the secondary ordinates.	61

5.17. Mode heat capacities (C) (solid lines, left ordinate) and their products with the density of states (DOS) (dotted lines, right ordinate) of selected IRMOFs with different organic linkers in (a) full and (b) the low-frequency (ν) range at 300 K.	63
5.18. Mode contributions of the squared group velocities in x direction ($v_{g,x}$) (solid line, left ordinate) and their products with the density of states (DOS) (dotted lines, right ordinate) of selected IRMOFs with different organic linkers in (a) full and (b) the low-frequency (ν) range.	65
5.19. Mean squared Grüneisen parameters at a temperature of 300 K for the studied MOFs according to eq. (3.28).	66
5.20. Mode dependent phonon lifetimes (τ) (solid lines, left ordinate) and their products with the density of states (DOS) (dotted line, right ordinate) of some IRMOFs with different organic linkers in (a) full and (b) the low-frequency (ν) range at 300 K.	68
5.21. Calculated thermal conductivity (κ) as a function of temperature (T) of MOF-5 with different metallic nodes.	70
5.22. Phonon band structure of the MOF-5 structure where the metallic nodes were varied. All the systems have an fcc Bravais lattice. The bands are coloured in a logarithmic scale showing the contribution to the thermal conductivity κ per \mathbf{q} point and mode.	72
5.23. Geometries of MOF-5(Zn) and MOF-5(Mg) relaxed with DFTB+. The linkers of MOF-5(Zn) pointing out of the paper plane are not perfectly aligned with the planes, which correspond to the lines drawn with an angle of 45° between the long molecular axes of the linkers of one face of the cubes. The result is the dihedral misalignment $\Delta\phi$	73
5.24. Density of states (DOS) of MOF-5 with with different metallic nodes in (a) full and (b) the low-frequency (ν) range. The cumulative DOS is plotted as dotted line on the secondary ordinates.	74
5.25. Mode contributions to the thermal conductivity (κ_{xx}) (solid lines, left ordinate) and their products with the density of states (DOS) (dotted lines, right ordinate) of MOF-5 with different metallic nodes in low-frequency (ν) range at 300 K.	75
5.26. Mode contributions to the thermal conductivity (κ) multiplied with the density of states (DOS) of MOF-5 with different metallic nodes in (a) full and (b) the low-frequency (ν) range at 300 K. The cumulative integrals are plotted as dotted lines on the secondary ordinates.	76
5.27. Mode heat capacities (C) (solid lines, left ordinate) and their products with the density of states (DOS) (dotted lines, right ordinate) of MOF-5 with different metallic nodes in (a) full and (b) the low-frequency (ν) range at 300 K.	78
5.28. Mode contributions of the squared group velocities in x direction ($v_{g,x}$) (solid line, left ordinate) and their products with the density of states (DOS) (dotted line, right ordinate) of MOF-5 with different metallic nodes in (a) full and (b) the low-frequency (ν) range.	80

5.29. Mode dependent phonon lifetimes (τ) multiplied with the density of states (DOS) of MOF-5 with different metallic nodes in (a) full and (b) the low-frequency (ν) range at 300 K.	81
5.30. Indication of how atoms that are in chemically inequivalent positions in the MOF-5 geometries are labelled in the projected density of states plots in fig. 5.31, 5.32, and 5.33.	82
5.31. Projected density of states (PDOS) for MOF-5(Mg). The PDOS is normalized in such a way that the integration over the wavenumber ν gives three times the number of the respective atoms. The labelling of the chemically inequivalent atoms can be found in fig. 5.30. A broadening has been introduced by means of eq. (5.2) with $\sigma = 2 \text{ cm}^{-1}$	83
5.32. Projected density of states (PDOS) for MOF-5(Mg). The PDOS is normalized in such a way that the integration over the wavenumber ν gives three times the number of the respective atoms. The labelling of the chemically inequivalent atoms can be found in fig. 5.30. A broadening has been introduced by means of eq. (5.2) with $\sigma = 2 \text{ cm}^{-1}$	84
5.33. Projected density of states (PDOS) for MOF-5(Mg). The PDOS is normalized in such a way that the integration over the wavenumber ν gives three times the number of the respective atoms. The labelling of the chemically inequivalent atoms can be found in fig. 5.30. A broadening has been introduced by means of eq. (5.2) with $\sigma = 2 \text{ cm}^{-1}$	85
A.1. Phonon frequencies (ν) at the Brillouin zone centre Γ calculated within DFTB and DFTB+ for MOF-5(Mg). Both simulations were carried out with the DFTB+ package. The frequency spectra was broadened with a Lorentzian according to eq. (5.2) with a broadening parameter $\sigma = 2 \text{ cm}^{-1}$ in order to obtain a density D at Γ	107
A.2. Histograms of the dot product between phonon eigenvectors of MOF-5(Mg) calculated within DFTB and the eigenvectors calculated within DFTB3. Both simulations were carried out with the DFTB+ package. In (a) all modes are considered, in (b) only modes low-frequency modes with a frequency up to 200 cm^{-1}	107
A.3. PES with respect to the dihedral angle φ measured between the symmetry plane between the pyridine rings of 44BP and one of the terephthalic acid linkers in MOF-508 obtained with DFTB and DFTB3. The tetragonal symmetry is kept by the better description of the hydrogen-hydrogen interaction of DFTB3.	108
A.4. First Brillouin zone of an fcc Bravais lattice. By courtesy of Elsevier [62]	109
A.5. Two-dimensional views of IRMOFs which differ only in the length of the linear organic linkers, but not in the metallic nodes.	110
A.6. Calculated thermal conductivity (κ) as a function of temperature (T) of some IRMOFs with different linear organic linkers.	111
A.7. Phonon band structure of IRMOF-130(Mg) with a fcc Bravais lattice. The bands are coloured in a logarithmic scale showing the contribution to the thermal conductivity κ per \mathbf{q} point and mode.	111

A.8. Density of states (DOS) of the IRMOFs with linear linkers in (a) full and (b) the low-frequency (ν) range. The cumulative DOS is plotted as dotted line on the secondary ordinates.	112
A.9. Mean squared Grüneisen parameters at a temperature of 300 K for the studied IRMOFs with linear linkers according to eq. (3.28).	113
A.10. Mode contributions to the thermal conductivity (κ_{xx}) (solid lines, left ordinate) and their products with the density of states (DOS) (dotted lines, right ordinate) of the IRMOFs with linear linkers in low-frequency (ν) range at 300 K.	113
A.11. Mode contributions to the thermal conductivity (κ) multiplied with the density of states (DOS) of the IRMOFs with linear linkers in (a) full and (b) detailed frequency (ν) range at 300 K. The cumulative integrals are plotted as dotted lines on the secondary ordinates.	114
A.12. Mode heat capacities (C) (solid line, left ordinate) and their product with the the density of states (DOS) (dotted line, right ordinate) of the IRMOFs with linear linkers in (a) full and (b) detailed frequency (ν) range at 300 K.	115
A.13. Mode contributions of the squared group velocities in x direction ($v_{g,x}$) (solid line, left ordinate) and their product with the the density of states (DOS) (dotted line, right ordinate) of the IRMOFs with linear linkers in (a) full and (b) the low-frequency (ν) range.	116
A.14. Mode dependent phonon lifetimes (τ) (solid line, left ordinate) and their product with the density of states (DOS) (dotted line, right ordinate) of the IRMOFs with linear linkers in (a) full and (b) the low-frequency (ν) range at 300 K.	117

List of Tables

4.1.	Systems with converged force constants allowing to calculate phonons for generic \mathbf{q} points. The supercell size necessary for this, the number of atoms in the primitive (N) and supercells ($N_{supercell}$) as well as the lattice parameters according to eq. (5.4) are listed.	33
4.2.	Quantities necessary to calculate the phonon lifetimes for the studied systems. All listed values were obtained from DFTB+ calculations. . . .	35
5.1.	Frequency ratios of the torsional modes localised in the linkers. Comparison between the calculated ratio from eq. (5.3) and the direct ratio of the phonon frequencies calculated using VASP.	41
5.2.	Equilibrium lattice constants a for two exemplaric systems calculated with VASP and DFTB+.	47
5.3.	Quantities relevant for the calculation of the phonon lifetimes according to the model of Bjerg et al. (cf. eq. (3.25).)	66
A.1.	DFTB3 parameters of the 3ob Slater-Koster files [48]. The Hubbard derivatives are listed in atomic units.	106

A. Appendices

A.1. Heat capacity for a system of harmonic oscillators

The following derivation of the heat capacity of a system of independent harmonic oscillators is inspired by [63, p. 140], although it is not done comprehensively there. One starts by expressing the Hamiltonian, \hat{H} , as a sum of its eigenenergies $\hbar\omega_j$ multiplied with the respective number operator of the j^{th} oscillator, \hat{N}_j . The index j can be seen as a shorthand notation for the quantum numbers \mathbf{q} and n that are used in section 3.

$$\hat{H} = \sum_j \hbar\omega_j \left(\hat{N}_j + \frac{1}{2} \hat{\mathbb{1}} \right) \quad (\text{A.1})$$

In the above equation the Hamiltonian has been expressed in its eigenbasis, in which it is diagonal. The term including the identity operator $\hat{\mathbb{1}}$ will be neglected in the following derivation since it only shifts the energy scale by a constant which is irrelevant, if one is interested in the heat capacity, i.e. the derivative of the energy with respect to the temperature.

In the canonical ensemble the partition sum Z is defined as the trace of the density operator $\hat{\rho}$.

$$Z = \text{tr} \{ \hat{\rho} \} \quad \text{with} \quad \hat{\rho} = \exp \left\{ -\beta \hat{H} \right\} \quad \text{and} \quad \beta = \frac{1}{k_B T} \quad (\text{A.2})$$

Using the Hamiltonian of equation (A.1) and evaluating the trace in its eigenbasis, one obtains the following result for the partition sum. The occupation number n_j is the respective eigenvalue of the number operator \hat{N}_j .

$$\begin{aligned} Z &= \sum_{n_1} \sum_{n_2} \cdots \sum_{n_M} \exp \left\{ -\beta \sum_j \hbar\omega_j n_j \right\} \\ &= \prod_j \sum_{n_j=0}^{\infty} \exp \{ -\beta \hbar\omega_j n_j \} \\ &= \prod_j \frac{1}{1 - \exp \{ -\beta \hbar\omega_j \}} \end{aligned} \quad (\text{A.3})$$

The natural logarithm of the partition sum can, therefore, be written as:

$$\ln Z = - \sum_j \ln \{ 1 - \exp \{ -\beta \hbar\omega_j \} \} \quad (\text{A.4})$$

This expression is helpful, when one wants to calculate the internal energy U according to the following equation.

A. Appendices

$$\begin{aligned}
 U = \langle \hat{H} \rangle &= \text{tr} \left\{ \hat{\rho} \hat{H} \right\} = \frac{1}{Z} \sum_{n_1} \sum_{n_2} \cdots \sum_{n_M} \hbar \omega_j n_j \exp \left\{ -\beta \sum_j \hbar \omega_j n_j \right\} \\
 &= \frac{1}{Z} \prod_j \sum_{n_j=0}^{\infty} \hbar \omega_j n_j \exp \left\{ -\beta \hbar \omega_j n_j \right\} = -\frac{\partial \ln Z}{\partial \beta} = -\sum_j \frac{\hbar \omega_j}{\exp \left\{ \beta \hbar \omega_j \right\} - 1}
 \end{aligned} \tag{A.5}$$

From this expression of the internal energy, one can easily compute the heat capacity as the derivative with respect to temperature:

$$C = \frac{\partial U}{\partial T} = \frac{\partial U}{\partial \beta} \frac{\partial \beta}{\partial T} = k_B \sum_j \frac{(\hbar \omega_j \beta)^2 \exp \left\{ \hbar \omega_j \beta \right\}}{(\exp \left\{ \hbar \omega_j \beta \right\} - 1)^2} \tag{A.6}$$

A.2. DFTB3

DFTB3 is the acronym for a density functional tight binding method that expands the DFT energy to third order with respect to the charge density[64]. In ordinary DFTB this expansion is truncated after the second order. There are certain Slater-Koster files available that offer the possibility to use the DFTB3 approach, where one has to set further special parameters. In order to estimate the influence of the method on the phonon frequencies, the vibrations at Γ were calculated for MOF-5(Mg) with DFTB and DFTB3. This was done with the DFTB+ code. All simulation parameters were the same as those reported in section 4.2. The additional parameters for DFTB3 are listed in the following table.

Tab. A.1: DFTB3 parameters of the 3ob Slater-Koster files [48]. The Hubbard derivatives are listed in atomic units.

Type of parameter	Value of parameter
Short range damping ζ	4.00
Hubbard derivative Mg	-0.02
Hubbard derivative O	-0.1575
Hubbard derivative C	-0.1492
Hubbard derivative H	-0.1857

Comparing the lattice parameter a (cf. eq. (5.4)) for the two methods, DFTB3 yields a slightly increased value of 13.175 Å compared to the result with ordinary DFTB of 13.165 Å. As can be seen in the following figures, neither the Γ point frequencies nor the eigenvectors change significantly between the results obtained with DFTB and DFTB3. The biggest relative change in the frequencies was a carbon-hydrogen vibration. This makes sense, since there is this special treatment of interactions of hydrogen with other atoms, based on a damping of short range interactions. However, this frequency is so high (approx. 3000 cm⁻¹) so that it has absolutely no influence on the thermal conductivity

that depends only on modes in the low-frequency region. The biggest relative deviation of DFTB from DFTB3 was less than 4 % in the range of 0 - 200 cm^{-1} .

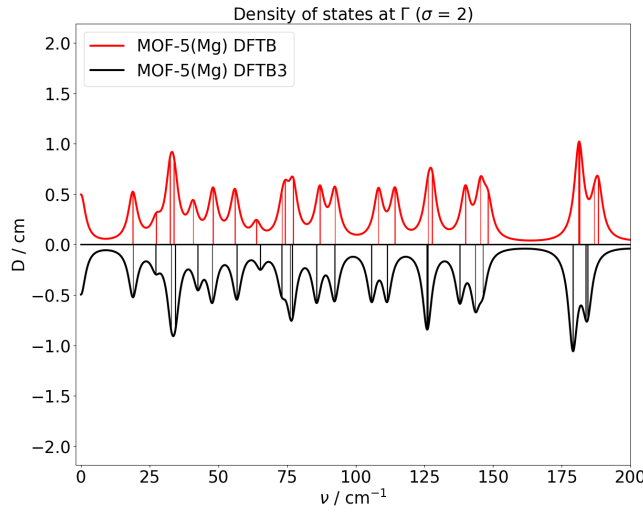


Fig. A.1: Phonon frequencies (ν) at the Brillouin zone centre Γ calculated within DFTB and DFTB+ for MOF-5(Mg). Both simulations were carried out with the DFTB+ package. The frequency spectra was broadened with a Lorentzian according to eq. (5.2) with a broadening parameter $\sigma = 2 \text{ cm}^{-1}$ in order to obtain a density D at Γ .

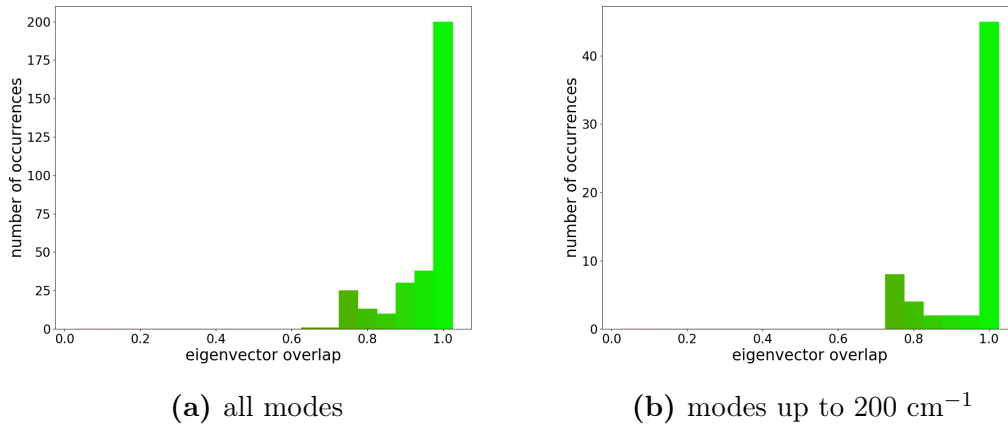


Fig. A.2: Histograms of the dot product between phonon eigenvectors of MOF-5(Mg) calculated within DFTB and the eigenvectors calculated within DFTB3. Both simulations were carried out with the DFTB+ package. In (a) all modes are considered, in (b) only modes low-frequency modes with a frequency up to 200 cm^{-1} .

A. Appendices

The only case, where it was essential to use DFTB3 together with a van der Waals (vdW) correction (D3 with Becke-Johnson damping and the standard parameters for DFTB3) was the geometry relaxation of MOF-508. The third order correction is supposed to improve the description of non-covalent interactions, which are important for the alignment of the 4,4'-bipyridine linker (44BP). The 44BP linker was therefore rotated once around the axis defined by the two nitrogen atoms and the total energy of the system was recorded every 0.5° in order to compute the PES with respect to the dihedral angle φ which is measured between the symmetry plane in the middle of the pyridine rings of 44BP and one of the terephthalic acid linkers in MOF-508.

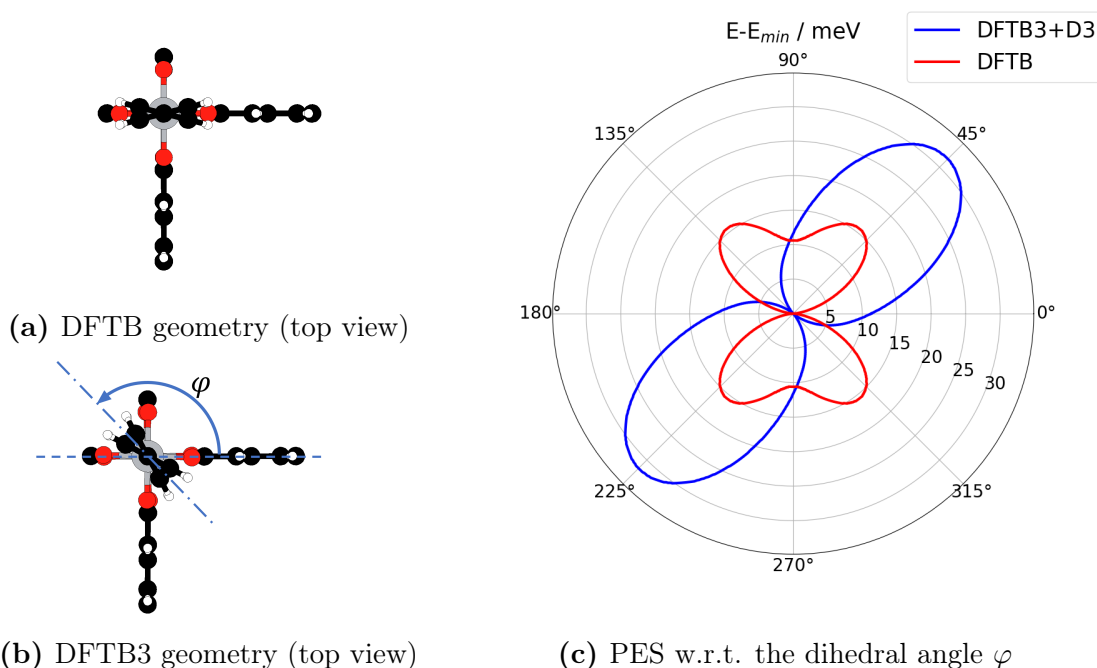


Fig. A.3: PES with respect to the dihedral angle φ measured between the symmetry plane between the pyridine rings of 44BP and one of the terephthalic acid linkers in MOF-508 obtained with DFTB and DFTB3. The tetragonal symmetry is kept by the better description of the hydrogen-hydrogen interaction of DFTB3.

From this plot it is obvious that without employing the DFTB3 with D3 vdW correction the 44BP is preferentially oriented along one of the axes of MOF-508. However, different situation would be the angle $\varphi = 135^\circ$. This can only be achieved by the aforementioned corrections and is also in agreement with the geometry obtained with VASP. It shall be stressed that it was only possible to obtain the described geometry (with $\varphi = 135^\circ$) by including both, the vdW correction and the DFTB3 functional.

A.3. First Brillouin zone and high symmetry point of a fcc Bravais lattice

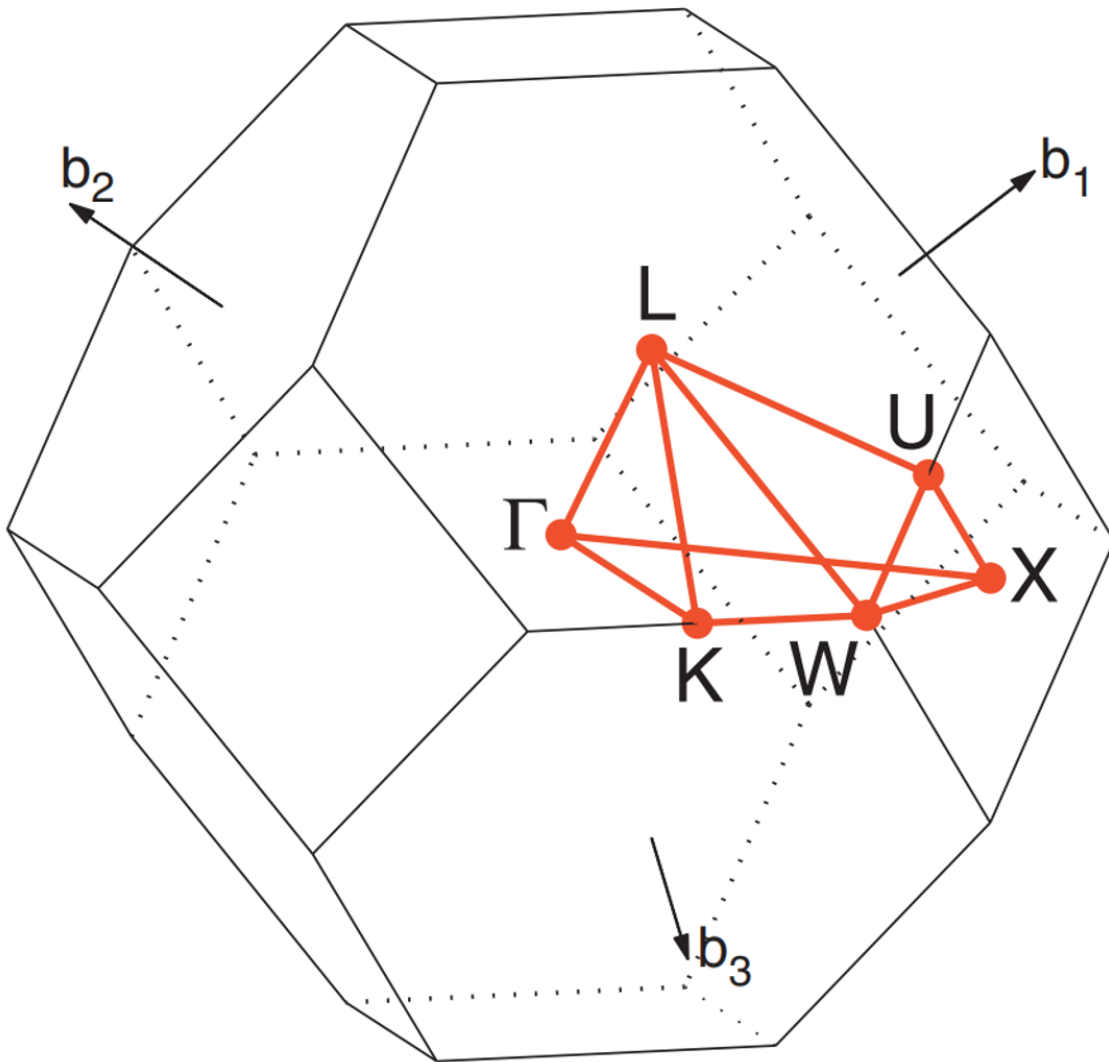


Fig. A.4: First Brillouin zone of an fcc Bravais lattice. By courtesy of Elsevier [62]

A.4. Linear linkers: IRMOF-130, IRMOF-131, and IRMOF-132

Contrary to increasing the linker length, one can also alternatively shorten it, resulting in a MOF that will be called IRMOF-130 (cf. fig. A.5(a)) in the following context. The general trends discussed in section 5 are validated by the following observations.

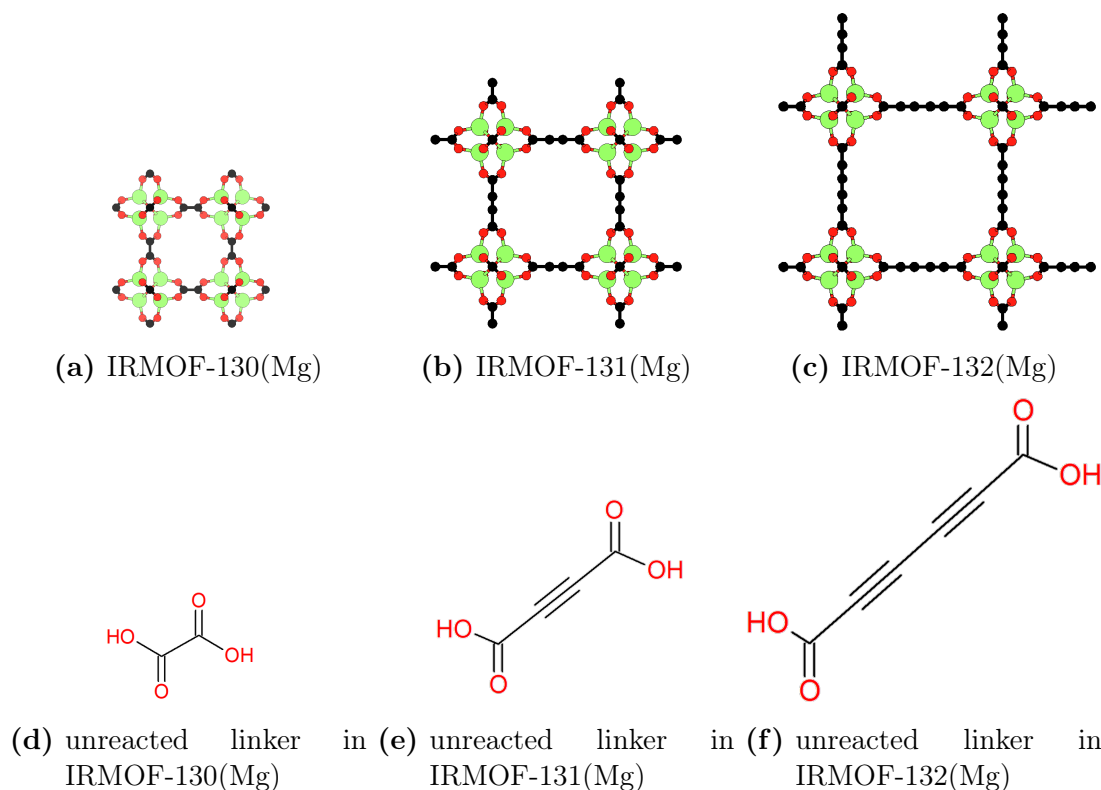


Fig. A.5: Two-dimensional views of IRMOFs which differ only in the length of the linear organic linkers, but not in the metallic nodes.

The linker used for IRMOF-130 is oxalic acid. The decreased length of this molecule compared to the alkynes of IRMOF-131 and IRMOF-132 results in an equilibrium lattice parameter $a = (8.84640 \pm 0.00001) \text{ \AA}$ (cf. eq. (5.4)) obtained with DFTB+ for the aforementioned settings. This lattice parameter results in a unit cell volume of about 1385 \AA^3 and an average mass for the primitive cell of $M = 16.40 \text{ u}$, considering the 46 atoms per unit cell. Further important parameters were the Debye frequency obtained from phonopy ($\nu_D = 1165 \text{ cm}^{-1}$) and the cutoff frequency ($\nu_{cut} = 98.3 \text{ cm}^{-1}$), with which the temperature scaling factor ($\Theta = 105.99 \text{ K}$) was calculated according to equation (3.30). A constant product of phonon lifetime and squared frequency (cf. eq. (3.25)) of 76.21 THz was obtained.

The temperature dependent thermal conductivity can be seen in figure A.11. The contribution per phonon frequency and \mathbf{q} point can be found in the band structure plot in figure A.7. The phonon DOS is shown in figure A.8.

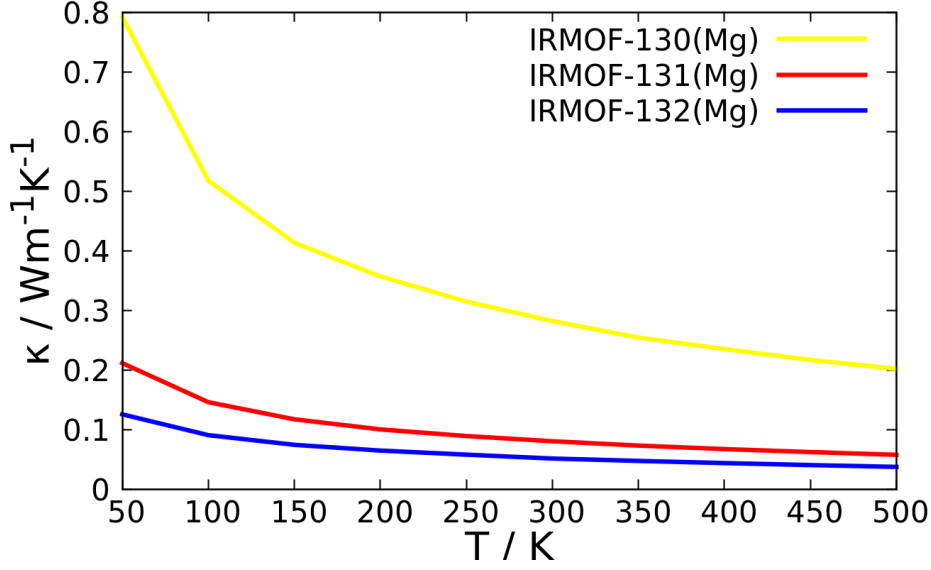


Fig. A.6: Calculated thermal conductivity (κ) as a function of temperature (T) of some IRMOFs with different linear organic linkers.

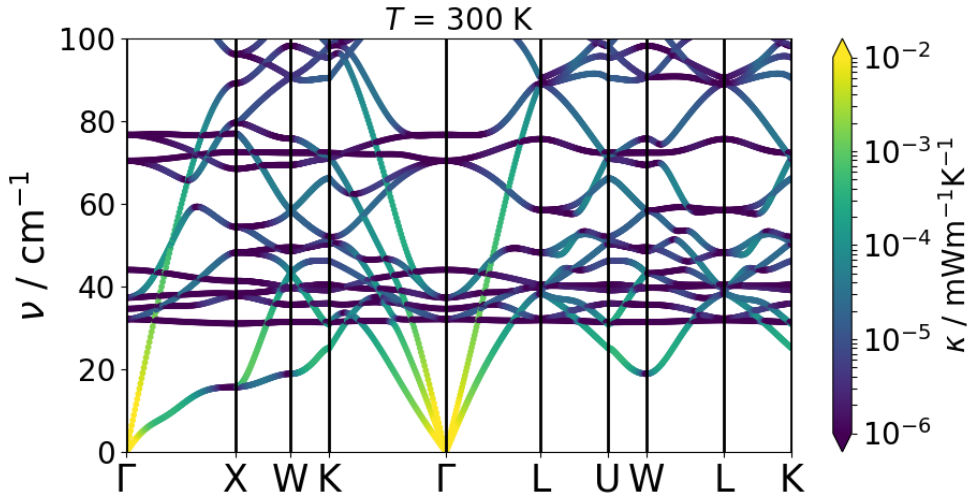
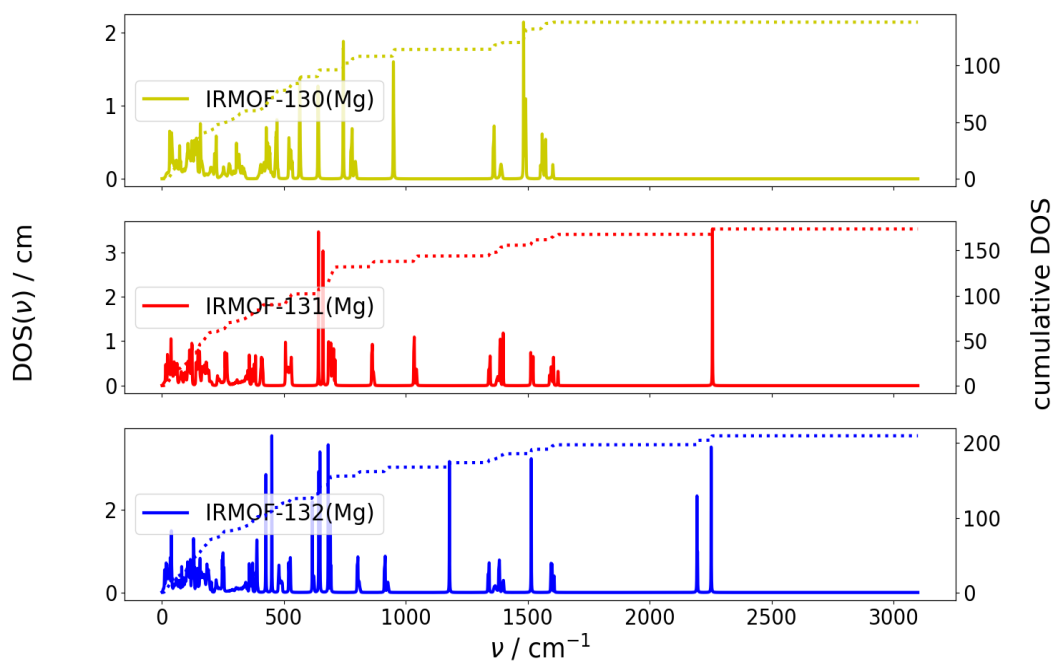
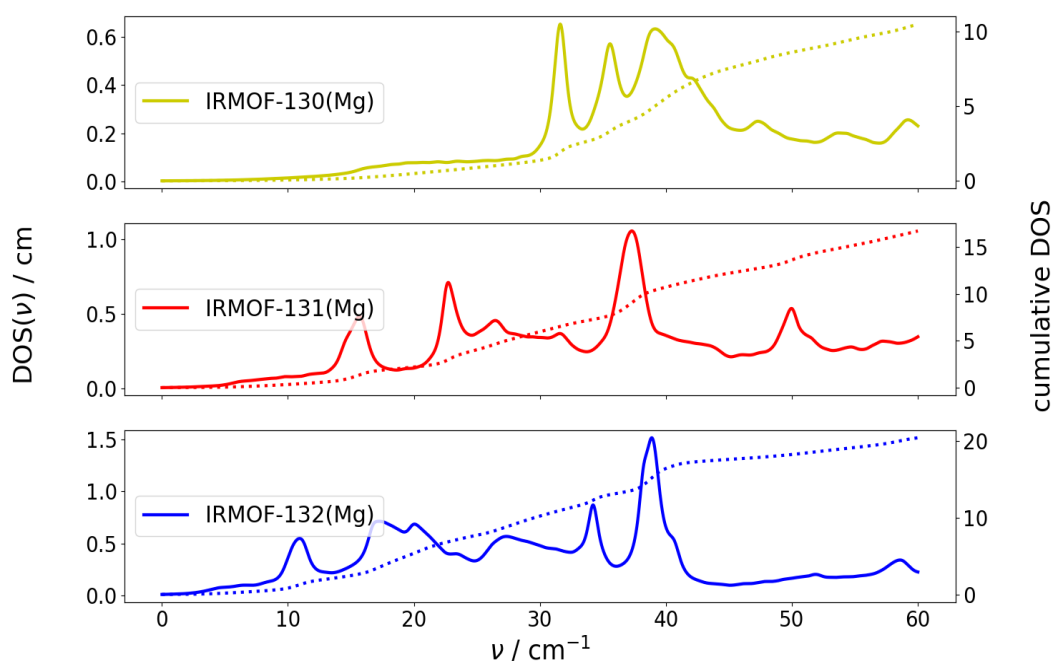


Fig. A.7: Phonon band structure of IRMOF-130(Mg) with a fcc Bravais lattice. The bands are coloured in a logarithmic scale showing the contribution to the thermal conductivity κ per \mathbf{q} point and mode.

The same trends, as discussed before, can be observed, including a reduced mean squared Grüneisen parameter (MSGP) for IRMOF-130 of approx. 38 (cf. fig. A.9), resulting in larger phonon lifetimes, as can be seen in figure A.14. Interestingly, the region of important contributions is extended to higher frequencies (approx. $\leq 60 \text{ cm}^{-1}$) as can be seen in figure A.6. The group velocities are somewhat reduced compared to IRMOF-131 and IRMOF-132 (cf. fig. A.13).



(a) Full range



(b) Zoomed in range

Fig. A.8: Density of states (DOS) of the IRMOFs with linear linkers in (a) full and (b) the low-frequency (ν) range. The cumulative DOS is plotted as dotted line on the secondary ordinates.

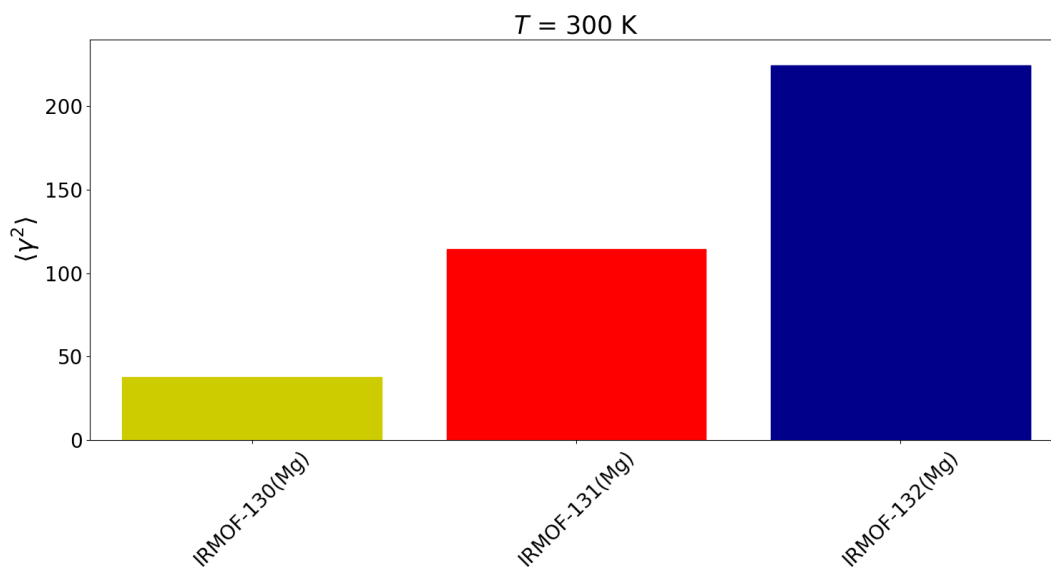


Fig. A.9: Mean squared Grüneisen parameters at a temperature of 300 K for the studied IRMOFs with linear linkers according to eq. (3.28).

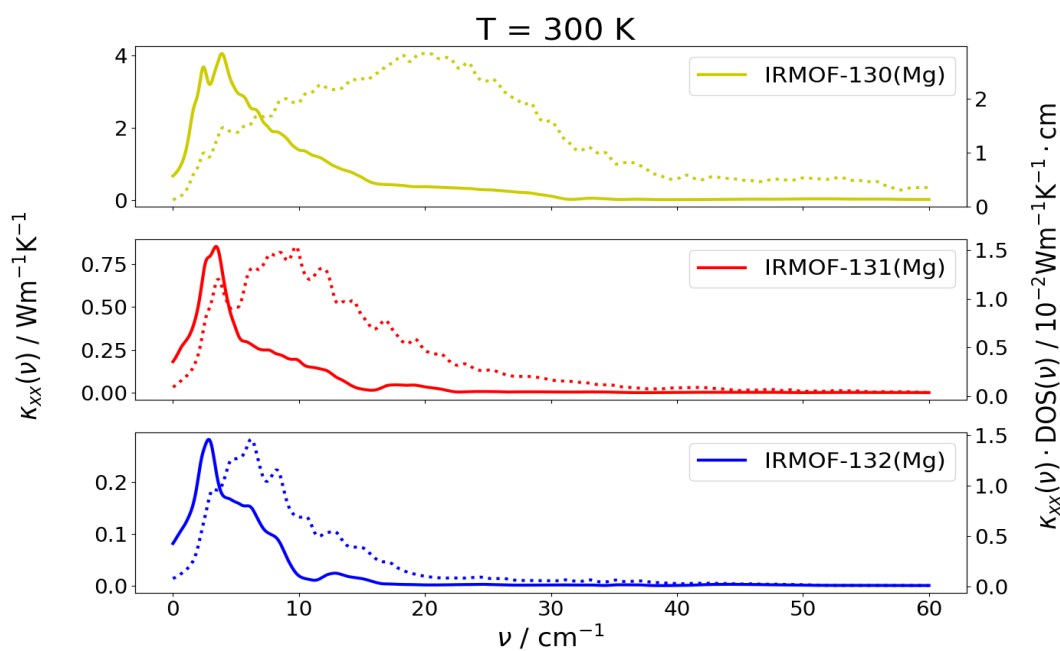
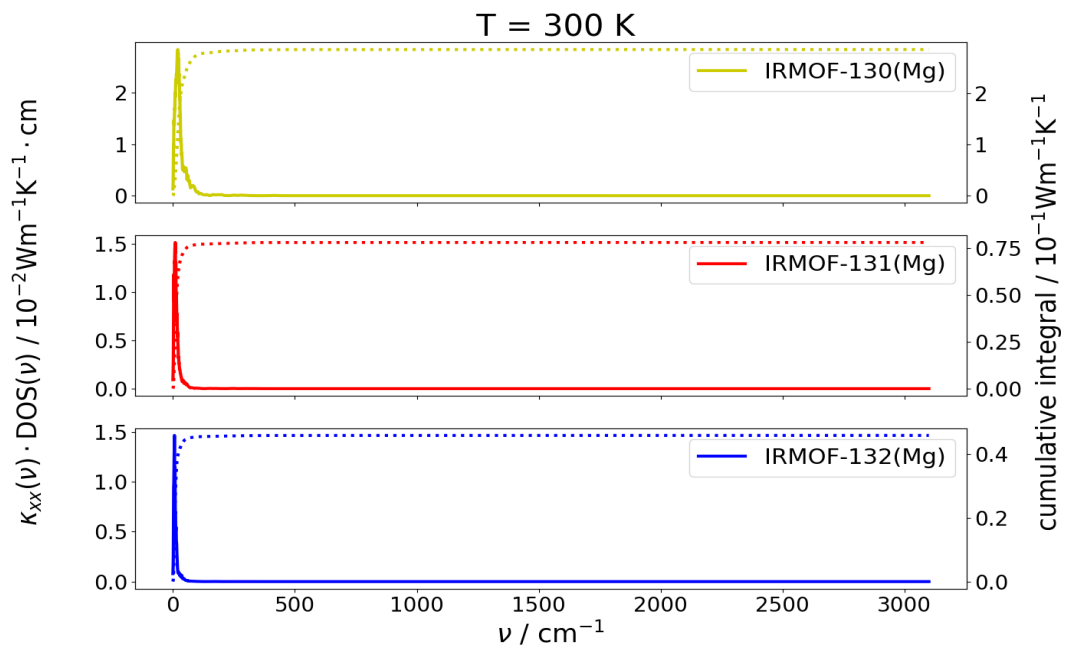
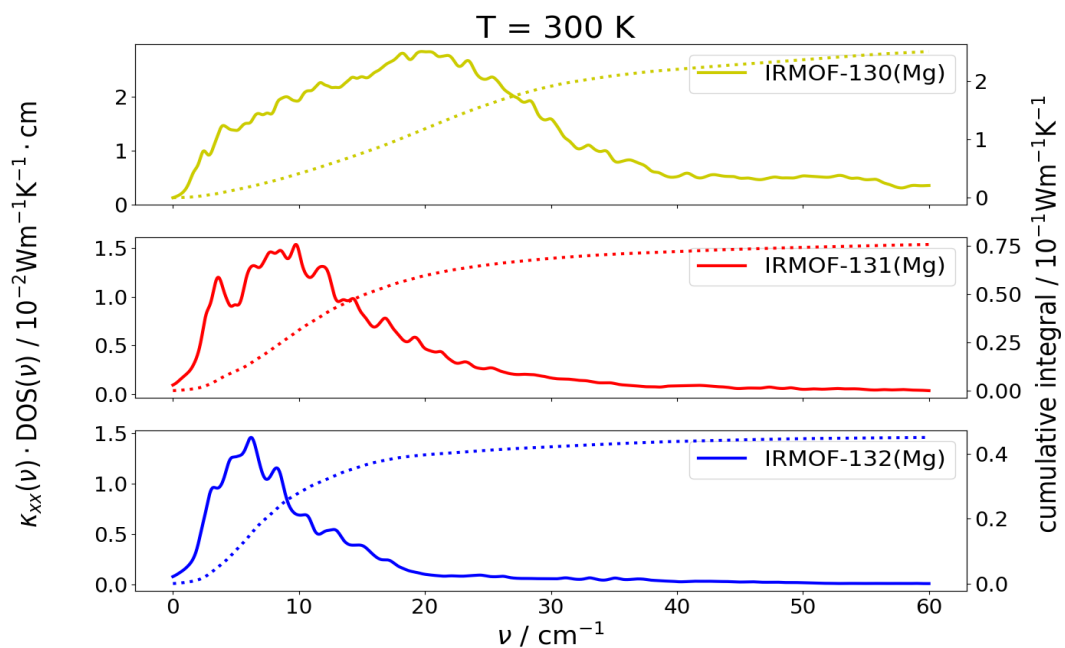


Fig. A.10: Mode contributions to the thermal conductivity (κ_{xx}) (solid lines, left ordinate) and their products with the density of states (DOS) (dotted lines, right ordinate) of the IRMOFs with linear linkers in low-frequency (ν) range at 300 K.



(a) Full range



(b) Detailed range

Fig. A.11: Mode contributions to the thermal conductivity (κ) multiplied with the density of states (DOS) of the IRMOFs with linear linkers in (a) full and (b) detailed frequency (ν) range at 300 K. The cumulative integrals are plotted as dotted lines on the secondary ordinates.

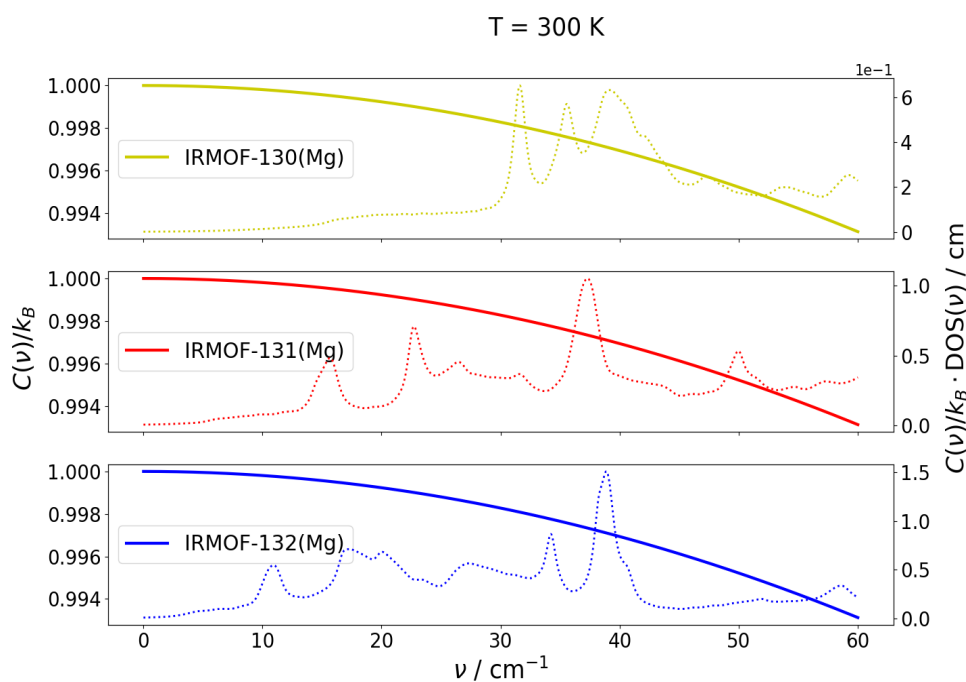
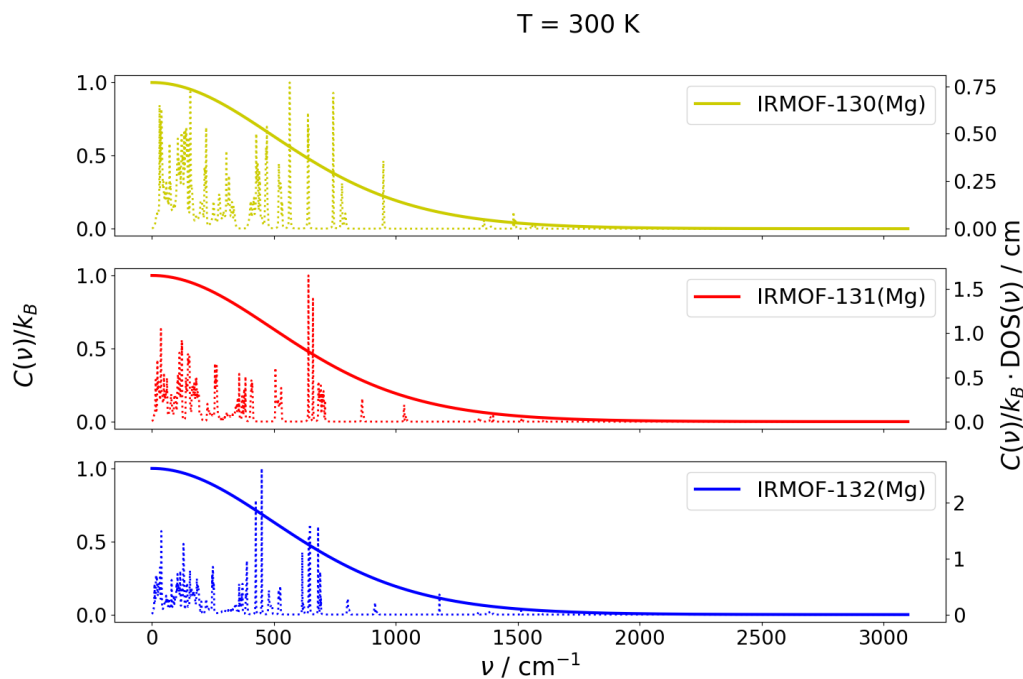


Fig. A.12: Mode heat capacities (C) (solid line, left ordinate) and their product with the the density of states (DOS) (dotted line, right ordinate) of the IRMOFs with linear linkers in (a) full and (b) detailed frequency (ν) range at 300 K.

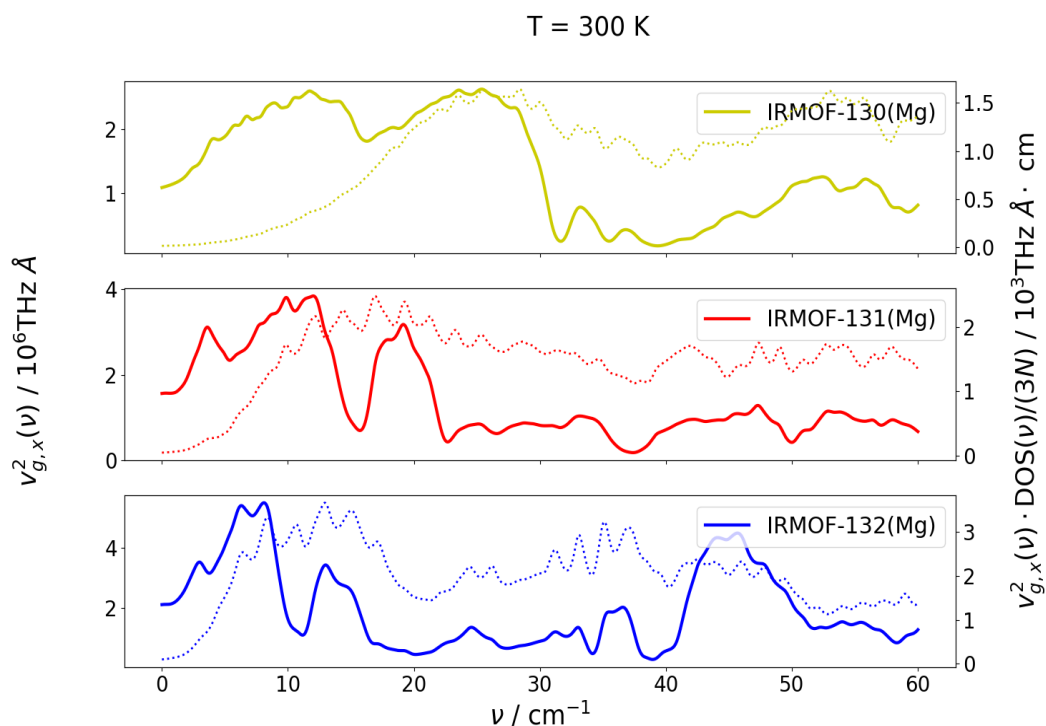
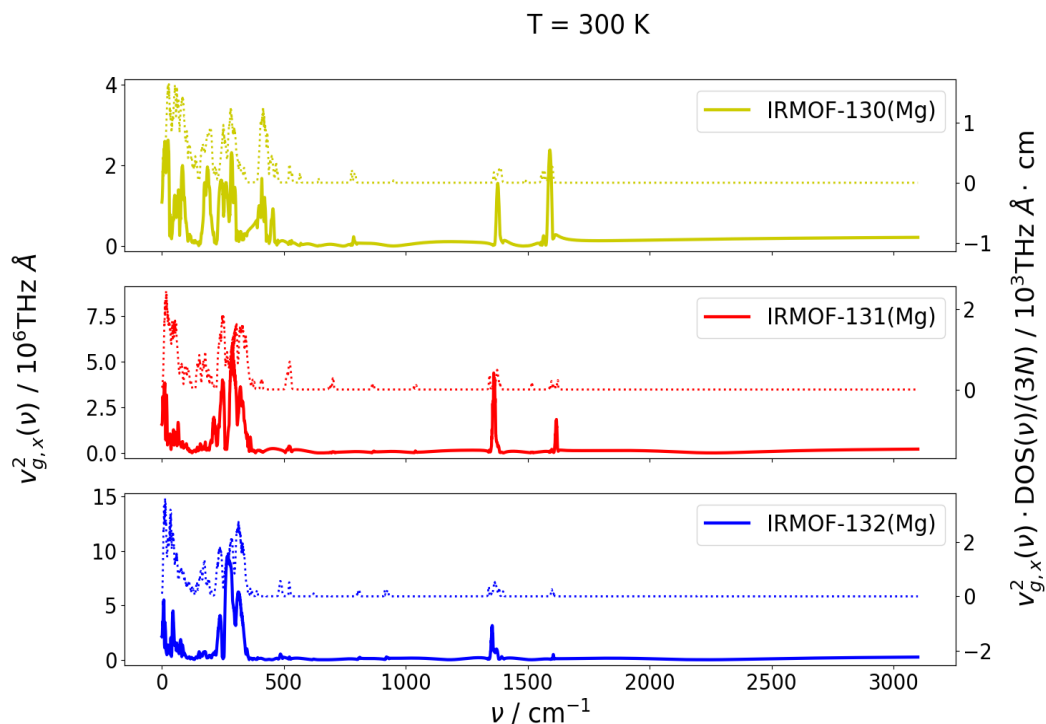


Fig. A.13: Mode contributions of the squared group velocities in x direction ($v_{g,x}$) (solid line, left ordinate) and their product with the the density of states (DOS) (dotted line, right ordinate) of the IRMOFs with linear linkers in (a) full and (b) the low-frequency (ν) range.

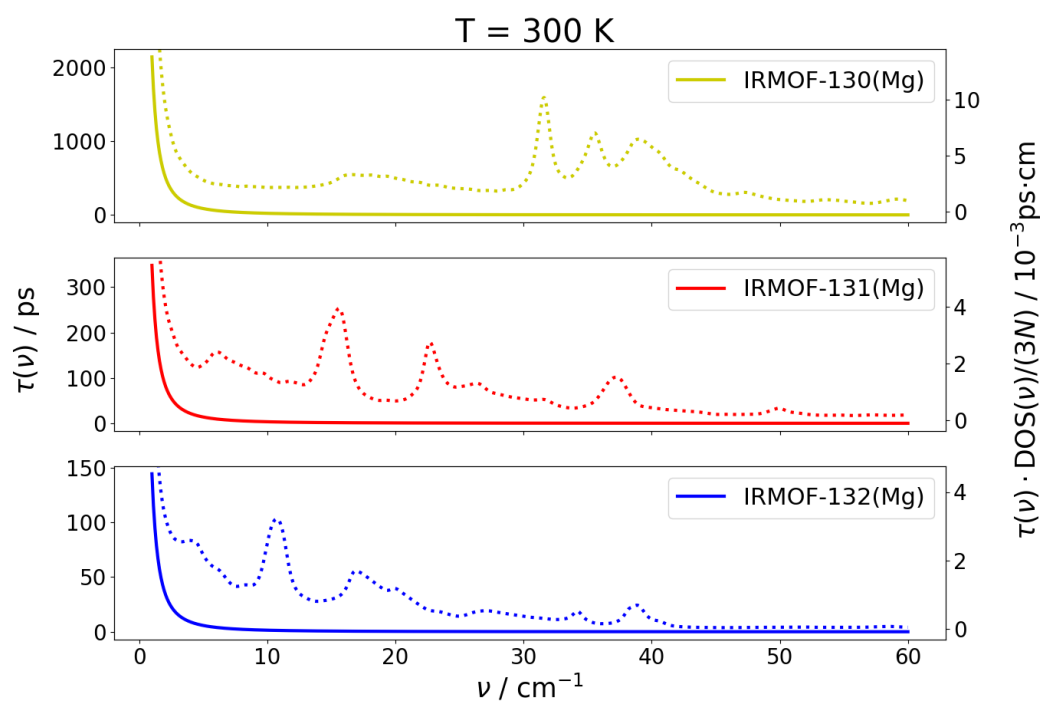
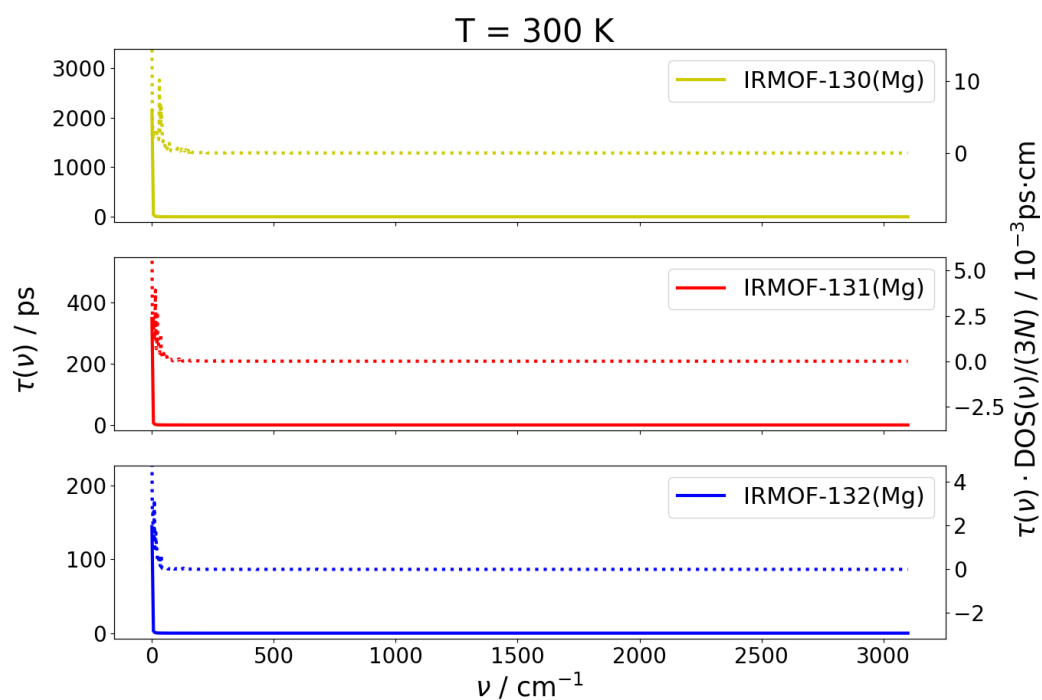


Fig. A.14: Mode dependent phonon lifetimes (τ) (solid line, left ordinate) and their product with the density of states (DOS) (dotted line, right ordinate) of the IRMOFs with linear linkers in (a) full and (b) the low-frequency (ν) range at 300 K.